Flagellated and Ciliated Microswimmers

Inaugural-Dissertation

zur
Erlangung des Doktorgrades
der Mathematisch-Naturwissenschaftlichen Fakultät
der Universität zu Köln
vorgelegt von

Sebastian Rode
aus Berlin

Jülich 2017

Berichterstatter:	Prof. Dr. Gerhard Gompper
(Gutachter)	Prof. Dr. U. Benjamin Kaupp

Tag der letzten mündlichen Prüfung: 15.12.2017

Abstract

The propulsion mechanism and the swimming dynamics of various ciliated microorganisms are investigated. Ciliated microswimmers, ranging from a single flagellated sperm cell to multiciliated microswimmers, propel themselves by cilia attached to their cell membrane. The underlying complex biomachinery of a cilium, the axoneme, employs an evolutionary developed mechanism, which is tailored to generate an optimal beating pattern to propel the swimmer through the environment it encounters. In this work mesoscale hydrodynamics simulations are used to simulate the whip-like motion of the cilium at low Reynolds numbers. The particle-based approach of multi-particle collision dynamics enables simulations of self-propelled microswimmers in complex confinements where steric and hydrodynamic interactions strongly influence the swimming dynamics. Details of cilia arrangement and beat shape are critical in understanding propulsion and surface attraction. The axonemal beating of cilia and flagella is modeled by a semi-flexible polymer with periodically changing intrinsic curvature. In the spirit of a minimalistic modeling approach, the axoneme is only bend along one degree of freedom, creating a defined beat plane.

The first part discusses surface attraction and guidance of sperm cells swimming in confinement. In particular, the motion of sperm in geometrically structured (zigzag) microchannels provides an interesting geometry for the manipulation and sorting of sperm cells. Sperm swim along the channel walls, but are deflected from the sidewall at sharp bends. The simulation results are in qualitative agreement with recent microfluidic experiments and provide a better insight into the mechanisms of sperm navigation under strong confinement. The effective adhesion of a sperm cell to a flat surface depends both on the envelope of its planar beat shape and on the orientation of its beat plane. A proposed self-propelled steric model explains the average deflection around corners. Further investigation of various beat patterns with increasing wavelength results in complex surface attraction dynamics of the sperm cell. The insight from the steric model helps to understand the surface attraction in terms of the beat-shape envelope. It is found that when the beat pattern exceeds a critical wavelength, the flagellum buckles and beats in a complex three-dimensional shape, which strongly increases surface attraction. Indeed, the analysis of three-dimensional experimental holographic data of freely swimming human sperm cells shows that on average the beat pattern is relatively planar but exhibits regular nonplanar components twice per beat. By comparing this high-resolution experimental data with simulation results, a possible explanation for the nonplanar beating is obtained. Simulated sperm with imposed planar bends and two orders of magnitude smaller twist than bending rigidity undergo a twist instability and exhibit a three-dimensional beat pattern.

Simulations allow to map the phase space of the twist instability, which shows no dependence on the bending rigidity, but a sharp transition from planar to three-dimensional beating below a critical twist rigidity. A localized twist wave goes through the cilium, which twists the cilium at a very narrow segment close to the point of minimal in-plane bending. This creates essentially two beat planes, separating the cilium in two segments of planar beating before and after the twisting region.

In the second part, propulsion and synchronization of multi-ciliated spherical swimmers with different cilia densities and arrangements are studied. Instead of pre-imposing the intrinsic curvature, a ratchet-like mechanism drives the ciliary beat pattern. Therefore, the beat period can be influenced by the flow generated from the motion of the other cilia. The propulsion velocity of ciliated spherical swimmers increases sub-linearly with increasing cilia density. Large differences in propulsion speed for equal numbers of cilia with different arrangements on the sphere are found. For symmetric ciliated swimmers, the emergence of a stable synchronization state is found to depend on the initial condition. In some symmetric 9-cilia swimmers, long stable phases of synchronization emerge. Swimmers whose phase difference increases due to phase slips have a slower propulsion velocity than swimmers which develop a constant phase-lag between cilia. Turning to an oscillator model for cilia synchronization, the emergence of metachronal coordination in different topologies above a surface is studied. The oscillators are modeled as hydrodynamically interacting spheres propelled along a circular trajectory. Non-dimensionalization of the model provides the radial confinement strength as the only control parameter. Boundary effects influence the synchronization as well as the confinement strength. In open chains of oscillators as well as in circular arrangements, stable large-scale patterns of synchronization emerge until a critical confinement strength. No long-term coordination emerges above a critical confinement strength in any of the studies topologies.

Finally, the cilium model is used to simulate a tuft of cilia, modeled to describe the placement of cilia in brain ventricles of mice. It is found that the particle flux towards the surface is located in hot-spots where the flux is significantly enhanced compared to purely diffusive transport. This shows the important role of ciliary beating in molecular transport towards primary cilia on the surface of the ventricles.

Contents

List of Figures **xi**

List of Tables **xv**

Nomenclature **xvii**

1 Introduction **1**

1.1 Evolution and Reproduction 1

1.2 Structure of the Thesis 2

1.3 Sperm 3

1.4 Ciliated Cells and Microswimmers 5

1.5 Propelling Cells by Ciliary Beating 7

1.6 Theoretical Approaches to Ciliary Beating 8

1.7 Microfluidics 9

1.8 Aim of the Thesis 12

2 Theory & Methods **13**

2.1 Hydrodynamics at Low Reynolds Numbers 13

2.1.1 Notation 13

2.1.2 Navier Stokes Equation 14

2.1.3 Stokes Equation and Green's Function 16
2.1.4 Mobility and Flow Field of a Sphere 19
2.1.5 Swimmer as Hydrodynamic Dipoles 20
2.2 Particle-based Simulation Methods 22
2.2.1 Introduction 22
2.2.2 Newtonian Dynamics 22
2.2.3 Langevin Dynamics 23
2.3 Mesoscale Hydrodynamic Approaches 24
2.3.1 Introduction 24
2.3.2 Tensor-based Hydrodynamic Simulations 26
2.3.3 Multiparticle Collision Dynamics (MPC) 28
2.4 Axoneme Model 33
2.4.1 Introduction 33
2.4.2 Sperm Model 34
2.4.3 Ciliary Beating 38
2.4.4 Kirchhoff Model of Semi-flexible Filaments 40
2.5 Mobility Coefficients of a Sphere, Rod and Beads 45

3 Sperm Cells **49**

3.1 Sperm in Microfluidic Channels 49
3.1.1 Introduction 49
3.1.2 Wavelength-dependent Surface Attraction 50
3.1.3 Rectangular Corner Deflection 56
3.1.4 Simple Steric Swimmer 60
3.1.5 Sperm Guidance and Selection in Narrow Channels . 64
3.1.6 Conclusions - Details Matter 73
3.2 3D-Beat Pattern of Sperm Cell 75

3.2.1 Introduction 75
3.2.2 Analysis of Experimental Data 75
3.2.3 Simulations 82
3.2.4 Conclusions 86

4 Cilia 89

4.1 Ciliated Microswimmers 90
4.1.1 Volvox & Chlamydomonas 90
4.1.2 Multi-ciliated Sphere Model 90
4.1.3 Effect of Cilia Arrangement on Propulsion Velocity . 92
4.1.4 Synchronization on Symmetrically Ciliated Swimmers 94
4.1.5 Conclusion 100
4.2 Synchronization Patterns in Cilium Oscillators 104
4.2.1 Motivation 104
4.2.2 Cilium Oscillator Model 104
4.2.3 Results 107
4.2.4 Conclusions 112
4.3 Particle Transport in Cilia Tufts 114
4.3.1 Ciliary Tufts in Brain Ventricles 114
4.3.2 Modeling and Data Extraction 116
4.3.3 Results 117

5 Summary & Conclusions 119

Appendix A 131

A.1 Gyration Tensor Decomposition 131
A.2 Phase Extraction from Limit Cycle 132
A.3 Adaptive Timestep 133

Appendix B 135

B.1 Simulation Parameters 135

B.2 Kurzzusammenfassung 139

List of Figures

1.1 Beat pattern of cilium and sperm 2
1.2 Human sperm cell schematic 4
1.3 Axoneme cross section 4
1.4 Electron microscopy image of Opalina 6
1.5 Motor control 9

2.1 Dipole flow field 21
2.2 MPC algorithm 30
2.3 Axoneme construction 36
2.4 Principle axes of the sperm cell 37
2.5 Space curve with material frame 41
2.6 Discrete flagella model 44
2.7 Mean-squared displacement 47
2.8 Dragged filament 48

3.1 Beat shape envelopes of sperm 52
3.2 Opening angles of the beat shape 53
3.3 Sperm trapping 54
3.4 Wavelength dependent surface attraction 55

3.5 Wavelength dependent sperm distribution in a planar channel 56

3.6 Zigzag channel 57

3.7 Sperm swimming in the corner 58

3.8 Deflection angle distribution 59

3.9 Beat-plane orientation 60

3.10 Sperm cell orientation and steric model 62

3.11 Varying corner angle γ 66

3.12 Detachment point distributions 67

3.13 Attachment time distributions 68

3.14 Detachment point distributions 69

3.15 2D vs. 3D beat plane orientation 70

3.16 Phase-space flow of the beat plane orientation 72

3.17 Beat pattern of a human sperm cell 76

3.18 Nonplanarity of the beat 77

3.19 Power spectrum of in-plane beat frequencies in dependence on the arc length 78

3.20 Flagellar beat shape in the local frame 79

3.21 Rolling speed and nonplanarity 80

3.22 Beat-plane nonplanarity in experimental data 81

3.23 Curvature and twist kymographs of the flagellum 82

3.24 Planar vs. nonplanar beat pattern 84

3.25 Twist/bending rigidity phase space 85

3.26 Simulation of nonplanar beating sperm 87

4.1 Multi-ciliated sphere model 91

4.2 Propulsion velocity 93

4.3 Fastest ciliated microswimmers per decade 94

4.4 Three 3-cilia swimmers 95
4.5 Phase differences of three 3-cilia swimmers 96
4.6 Propulsion velocity distribution 97
4.7 9-cilia swimmers 99
4.8 Phase difference of the 9-cilia swimmers 101
4.9 Propulsion velocity distributions of 9-cilia swimmers 102
4.10 Chain of oscillators 105
4.11 Circular arrangement of oscillators 107
4.12 Time relaxation of two oscillators 108
4.13 Stationary phase lag of two oscillators 109
4.14 Metachronal waves in chains 109
4.15 Chain vs. circle 110
4.16 Phase difference of oscillators 111
4.17 Confocal microscopy image of ependymal tissue 114
4.18 Distribution of tracked particles 115

List of Tables

1.1 Motor control mechanisms for axonemal beating 10

2.1 Mobility coefficients in MPC 46

4.1 Experimental scales of cilia tufts 116

B.1 Cilium simulation parameters 135

Nomenclature

Greek Symbols

α	deflection angle, page 58
α_t	oscillator trajectory orientation, page 106
α_{MPC}	MPC rotation angle, page 29
$\bar{\chi}$	phase difference between oscillator and the average phase, page 95
χ	phase difference between successive oscillators, page 107
$\delta_{\|\|}$	cone-like swimmer opening angle (parallel), page 63
$\delta_{\perp}$	cone-like swimmer opening angle (perpendicular), page 63
δ_b	in-plane opening angle of the beat-shape envelope, page 51
Δ_n	axoneme sliding displacement, page 9
δ_p	out-of-plane opening angle of the beat-shape envelope, page 51
η	dynamic viscosity, page 16
η’	first Lamé coefficient, page 16
Γ	Nonplanarity of the beat pattern, page 77
γ	corner angle, page 65
γ_c	harmonic potential strength, page 105
κ	curvature, page 9

λ	beat-shape wavelength, page 35
λ_b	principal moments of the gyration tensor along **b**, page 77
λ_c	oscillator trajectory confinement strength, page 104
λ_e	principal moments of the gyration tensor along **e**, page 77
λ_p	principal moments of the gyration tensor along **p**, page 77
μ_0	self mobility of a sphere, page 19
$\mu_{\|\|}$	mobility of a sphere moving parallel to a surface, page 20
$\mu_{\perp}$	mobility of a sphere moving perpendicular to a surface, page 20
$\mu_{R,\|\|}$	rod mobility coefficient parallel to the length axis, page 48
$\mu_{R,\perp}$	rod mobility coefficient perpendicular to the length axis, page 48
ω	angular frequency of the sperm beat (model), page 35
Φ	polar angle of sperm swimming along quarter-circles, page 67
ψ	latitude cilium position, page 92
ρ	density, page 16
τ	torsion, page 41
τ_b	beat period, page 108
τ_{MD}	Molecular dynamic integration time step, page 23
τ_{MPC}	streaming time step of fluid particles (MPC), page 29
θ	longitude cilium position, page 92
$\Theta_{\|\|}$	sperm cell inclination with parallel beat-plane orientation, page 63
$\Theta_{\perp}$	sperm cell inclination with perpendicular beat-plane orientation, page 63
φ	oscillator phase, page 106
ζ	intrinsic twist, page 41

Roman Symbols

A	amplitude of the imposed curvature of the beat, page 35
a	MPC box size, page 29
B_0	beat amplitude (equilibrium), page 35
D	diffusion constant (fluid), page 29
d	sidewall distance, page 57
f	frequency, page 78
f_0	beat frequency of a single cilium, page 91
f_n	normal force between axonemes, page 9
f_s	shear forces along the axoneme, page 9
h	height of the channel, page 57
i	discrete bond-length index, page 35
i_0	mid-point cilium, page 39
I_e	angular velocity of the rolling around the main axis, page 78
K_1	in-plane bending rigidity, page 42
K_2	out-of-plane bending rigidity, page 42
K_3	twist rigidity, page 42
k_b	Boltzmann constant, page 24
L	total flagellum length, page 35
L'	cone-like swimmer length, page 63
l_b	bond length filament, page 35
L_x	simulation box width (x), page 50
L_y	simulation box height (y), page 50

L_z	simulation box depth (z), page 50
m_{MD}	MD particle mass, page 23
m_{MPC}	fluid particles mass (MPC), page 29
n_0	index of the first active beat (cilium), page 39
N_{cilia}	number of cilia on the microswimmer, page 94
P	pressure, page 16
p	mean-value parameter for the inverse Gaussian distribution, page 68
q	shape-value parameter for the inverse Gaussian distribution, page 68
Q^P	power-stroke threshold, page 39
Q^R	recovery-stroke threshold, page 39
R	radius of curvature (circle), page 67
R_β	curvature response function, page 9
R_χ	displacement response function, page 9
R_γ	normal force response function, page 9
r_a	bead radius, page 19
R_c	radius of circular oscillator arrangement, page 107
r_h	head radius of the sperm cell, page 57
s	arc-length position, page 35
s_t	arc-length position of the twist point, page 81
s_{cm}	arc-length position in the middle of the sperm, page 51
T	temperature, page 24
t	time, page 16
T_0	thermostat desired temperature, page 32

$v_{recover}$	mid-point velocity, page 39
x	XYZ Cartesian coordinate system (global reference), page 20
y	XYZ Cartesian coordinate system (global reference), page 20
z	XYZ Cartesian coordinate system (global reference), page 20
px	pixel - point in a raster image, page 75

Vectors

$\bar{\mathbf{u}}$	center of mass velocity per box, page 29
$\mathbf{b}$	beat-plane axis, page 35
$\mathbf{e}$	sperm main-axis, page 35
$\mathbf{F}$	MD particle force, page 23
$\mathbf{f}$	force density, page 16
$\mathbf{F}_d$	Drag force of a sphere, page 19
$\mathbf{F}_{bi-normal}$	bi-normal restoring force, page 105
$\mathbf{F}_{normal}$	normal restoring force, page 105
$\mathbf{m}$	bi-normal vector, page 40
$\mathbf{n}$	normal vector, page 40
$\mathbf{p}$	beat-plane normal, page 35
$\mathbf{r}$	position vector, page 13
$\mathbf{t}$	tangent vector, page 40
$\mathbf{u}$	fluid velocity, page 16
$\mathbf{v}$	MD particle velocity, page 23

Matrices / Tensors

$\overleftrightarrow{\mu}$	mobility matrix (including hydrodynamic interactions), page 28
$\overleftrightarrow{G}$	Green's function of the stokes equation, page 18
$\overleftrightarrow{R}$	three-dimensional rotation matrix, page 29

Chapter 1

Introduction

1.1 Evolution and Reproduction

In the course of evolution, over millions of years, living matter developed from single cells into highly structured multi-cellular organisms. Individual organisms separated from each other and adapted their structure to their individual evolutionary niche. Evolution dictates that only the best adapted organism survives (Darwin, 1859).

The selection process tailored organisms where every detail is optimized towards evolutionary advantage. However, it is not easy to tell what needs to be optimized to achieve this advantage. From a physical/chemical point of view, the metabolism of cells is an out-of-equilibrium process which is tailored to extract the free enthalpy of their environment. One could argue that evolutionary optimization favors the most efficient method of extracting work from its surrounding. On the other hand, an extremely complex metabolism process increases the encoding complexity, making the occurrence of coding errors more likely and adaption to new environmental condition increasingly difficult. Thus, evolutionary optimized organisms expose an efficient, robust mechanism for metabolism, adaption and reproduction by developing evolutionary highly conserved structures, which fulfill roles within organisms but share a very similar structure. One example of such a structure is the cilium,

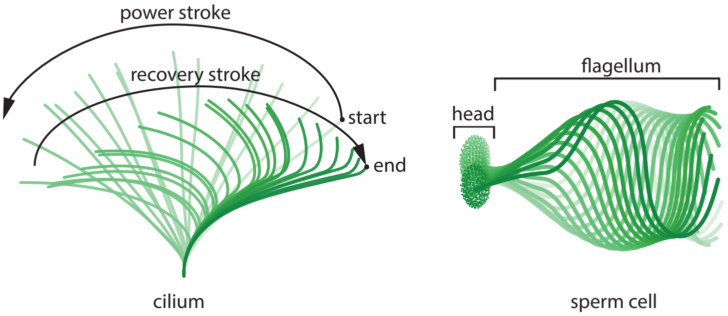

Figure 1.1 **Beat pattern of cilium and sperm** - Snapshots of simulations of the beat pattern of a motile cilium (left) and a sperm cell (right). The sperm consists of a spherical head and an actively beating flagellum. The time axis of the snapshots ranges from light-green to dark-green. With respect to the cilium the power stroke is more in light-green, whereas the recovery stroke is more in dark-green.

which functions as a force sensing and flow generating device on the surface of cells in almost all organisms. They have a critical role in embryogenesis where cilia propel sperm cells to transport DNA to the female egg cell and are essential in breaking left-right symmetry during development.

Substantially, hydrodynamic interactions provide a robust guiding principle in this fascinating process. In this work the consequences of cilia beat shape on propulsion and flow field generation are studied. The interplay of hydrodynamic and steric interaction under strong confinement is analyzed using fluid dynamic simulations.

1.2 Structure of the Thesis

The thesis is structured in five chapters. Chapter 1 introduces the topic of ciliated microswimmers and describes their internal structure. Chapter 2 recapitulates the fundamental theory describing hydrodynamics at low Reynolds numbers and Langevin dynamics, followed by the presentation of computational methods to solve hydrodynamic interactions and to simulate flagellar and ciliary beating. The results are presented in the following two main chapters:

Chapter 3 presents the results of flagellar beating of sperm. In particular, fluid dynamic simulations are used to explore the relationship between sperm cell beat patterns and swimming trajectories in highly structured environments, followed by the analysis of experimental three-dimensional human sperm cell data and its interpretation using hydrodynamic simulations.

Chapter 4 focuses on synchronization of multi-ciliated swimmers. First, the trajectories and states of synchronization on spherical ciliated swimmers are studied. Due to the high variety of different synchronization states found and the complexity of the underlying simulation, the multi-ciliated swimmer discussion is followed by the investigations of states of synchronization in a minimal oscillator model.

Finally, chapter 5 summarizes the results of both chapters and gives an outlook on interesting questions, which might be further investigated.

1.3 Sperm

Sperm cells are tiny one-way machines, built only to fertilize the egg cell. A human sperm cell, sketched in Fig. 1.2, consists of a disk-like head with ellipsoidal cross section to which a single cilium is attached, that propels the sperm. Due to its long length, it is often called flagellum (Gaffney et al., 2011). The first part of the flagellum, the mid-piece, is stiff. Only the following tail of the flagellum is bent by motor proteins.

The axoneme is a long and thin cylindrical structure (Howard, 2001; Lindemann and Lesich, 2010) with a length of $1 - 50\ \mu m$ and a radius of $250\ nm - 1\ \mu m$. A schematic representation of the axoneme is shown in Fig. 1.3. It consists of microtubules arranged in a 9+2 structure, where two inner-doublet microtubules, called central pair, are surrounded by a ring of nine outer-doublet microtubules. Nexin linkers strongly attach each of the outer doublets to its neighbors building a rigid structure. The axoneme is bend by dynein motors located along the entire axoneme which allows for a complex beat shape dynamic. Dynein molecular motors slide two neighboring microtubules along each other by hydrolysis of ATP (Gibbons and Rowe, 1965). Since sperm are single-purpose machines, they are optimized to

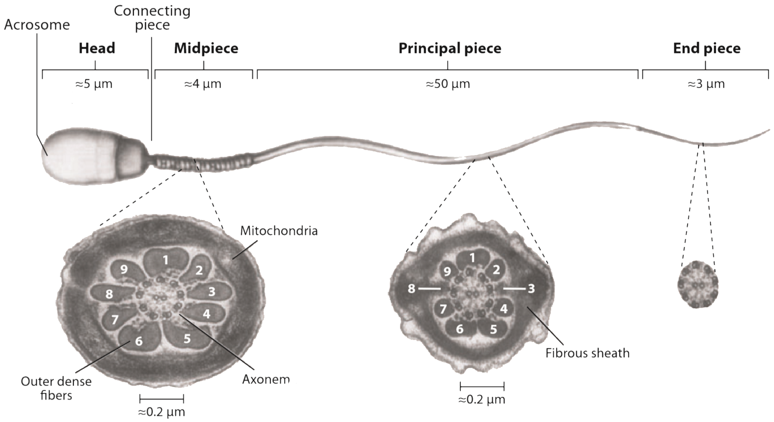

Figure 1.2 **Human sperm cell schematic** - The disk-like head with ellipsoidal cross section is attached to the flagellum. Besides the stiff midpiece the flagellum is beating in a whip-like pattern. Cross sections at different arc-length positions along the flagellum show the internal structure of the flagellum. The outer dense fibers in the mid-piece are a characteristic feature of internal fertilizers. (from: Gaffney et al. (2011)).

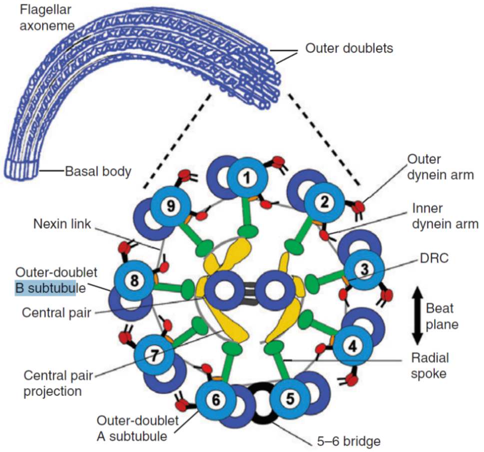

Figure 1.3 **Axoneme cross section** - Cross section of the axoneme of a cilium with the 9+2 arrangement of microtubules. Dynein motors move along the outer (microtubule) doublets to bend the axoneme. (from: Lindemann and Lesich (2010)).

transport the male DNA to the female egg. Their journey is an interactive process where the beat pattern of the sperm cell reacts to and interacts with the physical conditions it faces (Katz, Drobnis, and Overstreet, 1989). Active guidance of human sperm towards the egg cell is achieved by chemotaxis and thermotaxis (Eisenbach and Giojalas, 2006; Kaupp, Kashikar, and Weyand, 2008), as well as by rheotaxis (Bukatin et al., 2015; Kantsler, Dunkel, Blayney, et al., 2014; Miki and Clapham, 2013). A human sperm cell actively responses to progesterone-induced calcium influx (Strünker et al., 2011) by changing its beat pattern (Saggiorato et al., 2017). In addition to guidance by physical or chemical cues, sperm can be also guided passively along surfaces or walls. Sperm cells of humans (Winet, Bernstein, and Head, 1984), mice (Woolley, 2003) and bull (Rothschild, 1963) have a tendency to accumulate at surfaces. Simulation results confirmed a general tendency of alignment of sperm cells (Elgeti, Kaupp, and Gerhard Gompper, 2010; Fauci and McDonald, 1995) due to hydrodynamic and steric interactions. This has the consequence that sperm swim along surfaces purely based on physical interaction without actively altering their beating pattern.

Sperm move by the undulatory motion of the cilium. As head shape and length of sperm vary between species, so do the wavelengths and frequencies of the beat. This leads to different beat shapes of sperm. The majority of sea urchin sperm beat planar most of the time, but occasionally switch to a helical beat shape (Woolley and Vernon, 2001). Mammalian sperm cells undergo several structural changes during their lifetime which affects their beat shape (Mortimer, 1997). Free swimming human sperm cells rotate on their main axis and their flagellum forms a three-dimensional helical beat pattern (Katz, Drobnis, and Overstreet, 1989).

1.4 Ciliated Cells and Microswimmers

Cilia occur in two different variations and can fulfill two (mainly) distinct purposes. Motile cilia are actively beating either to propel a microswimmer or create a fluid flow close to cell surfaces, whereas immotile cilia do not beat but can act as a flow sensor for the cell on which surface they are exposed. In mammals motile cilia appear for example in the ventricles of the brain, in the

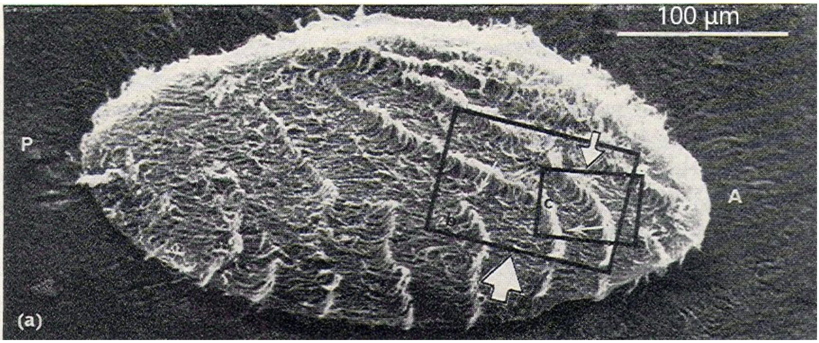

Figure 1.4 **Electron microscopy image of Opalina** - Cilia on the surface of *Opalina* show metachronal waves traveling from the anterior (A) to the posterior (P) end (from: Machemer (1974)).

Fallopian tube and in the trachea. On the surface of unicellular microswimmers like *Chlamydomonas*, *Paramecium* or *Opalina* they create propulsion.

The core structure of cilia, the axoneme, is very similar to that of sperm cells. Motile cilia have a 9+2 axoneme structure, whereas immotile/primary cilia have a 9+0 axoneme structure. Nodal cilia, which have a size of $2-3\ \mu m$, are significantly shorter than motile cilia found for example in the brain with a size of $12\ \mu m$. Instead of showing the almost planar beat pattern, they rotate consistently counterclockwise (viewed from base to tip) (Charles J. Brokaw, 2005). During mammalian embryogenesis the flow generated by nodal cilia provides essential information to determine the left-right asymmetry (Fliegauf, Benzing, and Omran, 2007; Nonaka et al., 1998). In particular primary cilia react to mechanical forces generated by flow with signaling responses such as calcium influx (Berbari et al., 2009; Davenport and Yoder, 2005; Eyckmans et al., 2011). Therefore, many genetic diseases are related to ciliary dysfunction (Valente et al., 2013).

Cilia are also present on smaller organisms, like algae, where they are attached to the membrane of a cell. The cilia density on such ciliated microswimmers varies from the single flagellum of a sperm cell, over a pair of two cilia on *Chlamydomonas* to hundreds of cilia that beat in a coordinated manner on the surface of *Paramecium* or *Opalina*. Here the ciliary beating creates a flow field around the swimmer that transports nutrition towards the cell membrane and propels the swimmer.

1.5 Propelling Cells by Ciliary Beating

Ciliated and flagellated microswimmers have to propel themselves on the micrometer scale, which implies that they have to swim faster than diffusion. As Lighthill (1989) points out, slenderness of the propulsion device mainly determines the swimming efficiency, which is in low for low Reynolds numbers. Prokaryotes and eukaryotes expose long and thin appendages on their surfaces. Even though the structure is often called flagellum for both cases, the way they create their beat pattern is completely different. Prokaryotes, like *Escherichia coli* bacteria, expose a flagellum which forms a passive helical structure and is rotated by a molecular motor sitting in the cell membrane (Berg, 2008; Darnton et al., 2007). They move in a run-and-tumble motion (Berg and Brown, 1972) by reversing the applied torques. Also, they use the flagella for mechanosensing where external forces trigger gene expression which eventually controls morphogenesis (Kawagishi et al., 1996; McCarter, Hilmen, and Silverman, 1988).

The beat-pattern generation of cilia is more complex than that of bacterial flagella. Torques are generated by dynein motors along the cilia which bend the filament locally, rendering it a self-contained biological machine (Charles J. Brokaw, 1961). They generate the traveling wave, which is going through the axoneme of sperm cells, and the beat pattern of cilia (Fig. 1.1). The beat pattern of a cilium on the surface of a cell divides into an elongated power and a recovery stroke close to the surface. The power stroke takes one third of the beating time, whereas the slower recovery stroke takes two thirds of the beating time.

Theoretical studies of densely ciliated microswimmers show that the emergence of metachronal waves increase propulsion velocity (Elgeti and Gerhard Gompper, 2013; Vilfan and Jülicher, 2006). An example of the ciliary metachronal wave on the surface of *Opalina* is shown in Fig. 1.4.

1.6 Theoretical Approaches to Ciliary Beating

The active beat pattern of the flagella of sperm cells and cilia is created by molecular motors which are distributed along the axoneme (Satir and Christensen, 2007). These dynein motors move along microtubules in finite steps where the energy for the motion is provided by ATP hydrolysis. The local displacement of the microtubules leads to a bending of the axoneme due to constraints caused by the basal body at the end of the axoneme and the nexin links between microtubules. Different mechanisms have been proposed (Bayly and Wilson, 2014; Hines and Blum, 1978; Howard, 2001; Satir, Pedersen, and Christensen, 2010) how motors self-organize into the wipe-like beating pattern observed in ciliary and sperm beating.

Table 1.1 summarizes three different proposed coupling methods between the axoneme structure and the internal motor activity. Motor activity is modeled as an explicit sliding force per motor (Lindemann, 2002), as a sliding force density $f(s,t)$ acting along the axoneme (Camalet and Jülicher, 2000) or as motors that switch between a constant and zero torque(Charles J. Brokaw, 1972). Modeling of structural details varies from assuming an elastic filament to resolving the full 9+2 microtubule-doublets arrangement. Since dynein motors only walk in one direction, periodic beating patterns need an oscillating motor activity between the left (2-5) and right (1-6) half of the microtubule-doublets. Experiments confirmed alternating motor activity between the two halves of the axoneme (Satir, 1985). Therefore, the underlying assumption and main difference of the motor control models is how the motor attachment and detachment rates depend on structural conformation of the axoneme and thereby creates an alternating sliding force density between the two halves. The three different motor control mechanisms of each model are visualized in Fig. 1.5. Motor activity is controlled by either the curvature $\kappa(s)$ of the axoneme, the perpendicular forces $f_{\perp,n}(s)$ separating neighboring microtubule doublets, or the sliding displacement Δ_n between microtubule doublets. The curvature-control mechanism regulates motor detachment based on a curvature threshold, e.g. a large curvature leads to reduced motor activity and less bending. The normal-force-control mechanism regulates the detachment of motor based on the normal force between neighboring, curved microtubule doublets. The sliding-control mechanism regulates detachment based on the

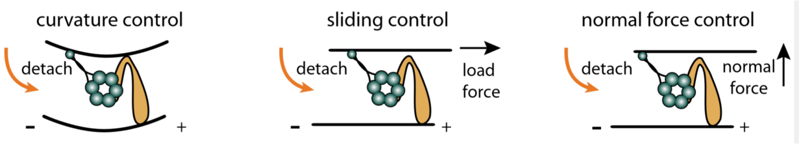

Figure 1.5 **Motor control** - Schematic representation of the three different Dynein (orange) control mechanisms. Signs indicate the polarity of the doublet. Motor detachment is controlled by either the curvature, sliding of doublets or the normal force between them (from: Sartori et al. (2016)).

tangential force along the axoneme, due to the competition between the motors on opposing sides, oscillations emerge (Jülicher and Prost, 1997).

Mathematically speaking the dynamics of shear forces $f_s(s,t)$ have to undergo a Hopf bifurcation leading to oscillations of the beating frequency ω. Using Fourier decomposition, a general response function (Sartori et al., 2016) summarizing all proposed regulation patterns can be written as:

$$f_s(\omega,s) = R_\chi(\omega)\Delta_n(s) + R_\beta(\omega)\kappa(s) + R_\gamma(\omega)f_n^\perp(s) \tag{1.1}$$

The complex valued response functions R_χ, R_β and R_γ give a relation between the sliding force and the corresponding quantity. The real part relates to the value itself, whereas the imaginary part relates to its rate of change. Due to the Fourier transform the imaginary part reflects the time derivative. By fitting all three response functions, Sartori et al. (2016) show that curvature control reproduces experimentally observed beating patterns most reliable. Interestingly, the important ingredient is the coupling to the change of curvature and not the absolute value of the curvature itself.

1.7 Microfluidics

Microfluidic devices allow to control experimental conditions on the scale of microswimmers, i.e. in the order of 100 μm. Microfluidic devices range from

Type	Type of motor	Feedback	structure	response function coefficients
Curvature (Brokaw)	positive constant or zero shear forces	Curvature and hysteresis for negative bending moments	Microtubules, nexin linkers (single filament)	β
Geometric Clutch (Lindemann)	continues sliding force density	normal force	4 dynein motors per microtubule doublet (very detailed)	γ
Sliding (Jülicher)	continues sliding force density	sliding	microtubules, nexin linkers (single filament)	χ

Table 1.1 **Motor control mechanisms for axonemal beating** - The table compares theoretical models which explain the self-organization principle leading to axonemal beating. The models implement the structure of the axoneme with different level of detail. Motor activity is implement in a similar way by either shear forces or bending, whereas the feedback of the structural change to the motor activity differs between models. The three different options are sketched in Fig. 1.5 and correspond to the three different coefficients, as explained in the main text.

chemical micro reactors over diffusive separation systems to micro-pumps (Tabeling, 2005). A combination of these subsystems enables the construction of lab-on-a chip systems, where entire bio-medical analysis can be performed on the scale of just a few organisms.

Passive surface guidance, where microswimmers align and swim along surfaces, are used to rectify microswimmers along a desired direction or spatially separated by swimming velocity. Microfluidic devices with cavities have been shown to sort bacteria by length (Elizabeth Hulme et al., 2008) and two slightly shifted U-shape barriers allow to direct motion of swimmers along one direction(Guidobaldi et al., 2014). In sperm research, especially for in-vitro fertilization, microfluidic devices are used to sort sperm according to their health or sex. A variety of channel designs to sort sperm cells are successfully applied in sperm research (Knowlton, Sadasivam, and Tasoglu, 2015). Relatively simple junction-designs allow the separation of motile from non-motile sperm. Flow cytometric sexing of mammalian sperm is increasingly applied in cattle-breeding where the differences of X and Y chromosome are used to optically identify sex and sort sperm cells by selective microfluidic flow patterns (Vazquez et al., 2009).

The critical components for determining sperm quality are concentration, motility, and morphology (Amann and Katz, 2004). Recent computer-aided analysis methods allow to self-diagnose semen quality (Kanakasabapathy et al., 2017), based on the correlation between DNA integrity and sperm motility (Robinson et al., 2012; Zini et al., 2008). Microfluidic experiments show a strong correlation between the ability of sperm cells to follow corners and their DNA integrity (Eamer et al., 2016). This does not only suggest, that the narrow channel of the Fallopian tube might have evolved in order to enhance the chance of the “best” sperm cell to reach the egg cell, but also opens the door for improved diagnostics and filtering devices. Experiments by Kantsler, Dunkel, Polin, et al. (2013) highlighted the importance of steric interactions in surface guidance and provide a starting point for the fluid dynamic simulation of this work (section 3.1). The combination of passive structural properties and an in-depth understanding of the swimmer mechanism provides a promising diagnostic tool and sorting device.

1.8 Aim of the Thesis

Flagella and cilia are ubiquitous structures throughout eukaryotic life forms. This thesis investigates their role in the propulsion of microswimmers using simulation of ciliated microswimmers with their complex beat shape and explores the physical mechanisms of boundary interactions. Mircoswimmers are living organisms that have complex signaling pathways. They are potentially able to influence the flagella/cilia beat shape in many ways.

However, the aim of this thesis is, to identify minimal models, based on fundamental physical laws, that explain experimentally observed patterns. If a physical, minimal model can explain the experimental observation, insight is gained, into what the underlying process and interactions of the observed phenomena are. In particular, these models demonstrate which patterns might emerge based on physical laws without the need for complex biochemical signaling.

The first part of the thesis looks at guidance of sperm cells by boundary interactions. It considers the following questions: How do steric and/or hydrodynamic interactions attract sperm cells towards surfaces? How do the beat shape and the pattern of the channel walls influence surface attraction? Can a change in beat-shape alter surface attraction?

The second part of the thesis draws the attention to hydrodynamic interactions between multiple cilia. How does the arrangement of cilia on a spherical swimmer change the emergence of states of synchronization? Under which conditions do metachronal waves (a constant, non-zero phase difference between neighboring cilia) emerges? How do boundaries and topological differences influence the emerging patterns?

The common subject is found in the emergence of complex swimming behavior based on the combination of the active flagellar beat, boundaries in hydrodynamic simulations, followed by the development of a simple model which captures the essential dynamics.

Chapter 2

Theory & Methods

2.1 Hydrodynamics at Low Reynolds Numbers

2.1.1 Notation

Notation of vectors and matrices is handled by the following convention. Lower indices represent the particle number, whereas upper indices represent the coordinate in index notation. The position of particle is a $\mathbb{R}^3$ vector with components:

$$\mathbf{r}_i = \begin{pmatrix} r_i^x \\ r_i^y \\ r_i^z \end{pmatrix} . \tag{2.1}$$

Bold quantities are vectors $\mathbf{v}$. Matrices $\overleftrightarrow{m}$ are marked by a double arrow. By default, vectors are three-dimensional $\mathbf{v} \in \mathbb{R}^3$ quantities and matrices have a corresponding square shape $\overleftrightarrow{m} \in \mathbb{R}^{3\times3}$. If their shape differs, dimensionalities are stated explicitly. In index notation Einstein summation is used to simplify sums.

2.1.2 Navier Stokes Equation

Hydrodynamics describe the flow of matter in liquid or gas state. This applies to single component Newtonian gases and fluids, but it is not limited to them. It is a generalization of Newtonian motion to the movement of many (similar) interacting particles under external forces. The velocity field $\mathbf{u}(\mathbf{r},t)$ and the particle density $\rho(\mathbf{r},t)$ describe the flow direction and density of particles in space and time.

The governing equation for these fields is the Navier-Stokes equation which can be derived using conserved quantities of the system like mass and momentum. The production terms and fluxes in a volume equal the local change of the corresponding quantity. Most familiar is the continuity equation for mass conversation under the assumption of a single component and conserved total mass:

$$\int_V \frac{\partial \rho(\mathbf{r},t)}{\partial t}\, dV = -\oint_{S(V)} \rho(\mathbf{r},t)\mathbf{u}\, dS \tag{2.2}$$

The change of particle density in a volume V equals the flow of particles through the surface of this volume $S(V)$. Using Gauss theorem, the differential form of the mass balance can be easily derived:

$$\frac{\partial \rho}{\partial t} = -\nabla^j(\rho u^j) \tag{2.3}$$

This states that density change in a volume has to equal the flow of mass in or out of it. The momentum balance follows in a similar form from a generalization of Newtonian dynamics:

$$\int_V \rho \frac{d\mathbf{u}}{dt}\, dV = \int_V \mathbf{f}\, dV + \oint_{S(V)} \tilde{\mathbf{P}}\, dS, \tag{2.4}$$

where $\mathbf{f}$ is the force density acting on the fluid and $\tilde{\mathbf{P}}$ the tension on the surface of the volume element. The stress tensor can be expressed as $\tilde{P}^i = \sigma^{ij} n^j$, with $\mathbf{n}$ being the surface normal. Using Gauss theorem, the differential of momentum balance explicitly yields:

$$\rho\frac{du^i}{dt} = \rho\left(\frac{\partial u^i}{\partial t} + u^j\nabla^j u^i\right) = \nabla^j\sigma^{ij}n^j + f^i$$
$$\rho\frac{\partial u^i}{\partial t} = \nabla^j\left(\sigma^{ij} - u^j\rho u^i\right) + f^i, \tag{2.5}$$

where in the second line the total derivative is expanded by the chain role into the advective contribution and intrinsic variation of the velocity with time. By applying the chain rule again and using Eq. (2.3) the equation takes the form of a continuity equation. The momentum flux consists of two terms: the momentum flux that is transported by the flow field and the momentum exerted by the stress normal to the boundaries of a volume element.

For a homogenous, isotropic medium the stress tensor can only depend on a hydrostatic pressure P and the derivatives of the strain rate. Additional symmetry consideration leads to the Cauchy-Euler stress tensor:

$$\sigma^{ij} = \left(-p(\rho,T) + \eta'(\rho,T)D^{kk}\right)\delta^{ij} + 2\eta(\rho,T)D^{ij} \tag{2.6}$$

$$D^{ij} = \frac{1}{2}\left(\frac{\partial u^i}{\partial r^j} + \frac{\partial u^j}{\partial r^l}\right) \qquad \textbf{linear strain rate tensor} \tag{2.7}$$

The dynamic viscosity $\eta(\rho,T)$ and the first Lamé coefficient $\eta'(\rho,T)$ are transport properties of the medium. Under isothermal conditions, pressure and viscosity of the medium are independent of temperature which decouples the internal state equations for the energy and entropy from the force and momentum balance. Finally, the Navier-Stokes equation follows by inserting the stress tensor into the local formulation of the momentum balance:

$$\rho\left(\frac{\partial\mathbf{u}}{\partial t} + \mathbf{u}\cdot\nabla\mathbf{u}\right) = -\nabla P + \eta\,\triangle\mathbf{u} + (\eta' + \eta)\nabla\,(\nabla\cdot\mathbf{u}) + \mathbf{f} \tag{2.8}$$

The left-hand side is the advective derivative of the velocity, i.e. it describes fluid inertia. The velocity field either changes explicitly with time (partial time derivative) or the gradient of the flow field transports matter along its flow lines (gradient term). Forces acting on the fluid and internal stress are on the right-hand side: the pressure gradient ∇P, a viscous friction term, a term related to the compressibility and finally applied external body force densities $\mathbf{f}$.

Similar local formulation, using conserved quantities, can be derived for the angular-momentum, energy and entropy in the system, leading to corresponding balance equations. In general, pressure and viscosity couples the internal energy change to the momentum balance.

Assuming additionally, an incompressible medium, the compressible part in the stress tensor vanishes $D^{kk} = 0$. In the incompressible Navier-Stokes equation the transport properties only depend on the constant viscosity of the medium:

$$\rho \left(\frac{\partial \mathbf{u}}{\partial t} + \mathbf{u} \cdot \nabla \mathbf{u} \right) = -\nabla P + \eta \triangle \mathbf{u} + \mathbf{f}. \tag{2.9}$$

Finding exact solutions for this non-linear partial differential equation is difficult and only possible for simple geometries.

2.1.3 Stokes Equation and Green's Function

The length scales of many biophysical problems are in the range of micrometers. Thusm especially microswimmers have a small mass compared to the surface area. Therefore, inertia effects are small compared to friction. The Reynolds number $Re = \frac{\rho u L}{\eta}$ quantifies this difference. It emerges from rewriting the incompressible Navier-Stokes equation in nondimensional units in terms of a typical mean velocity amplitude u, a length scale L. Rescaling all units accordingly and plugging these in Eq. (2.9), yields:

$$\mathrm{Re} \left(\frac{\partial \mathbf{u}}{\partial t} + \mathbf{u} \cdot \nabla \mathbf{u} \right) = -\nabla P + \triangle \mathbf{u} + f. \tag{2.10}$$

If the Reynolds number is small, $\mathrm{Re} \ll 1$, inertia terms are negligible compared to friction.

In the low-Reynolds number regime the Navier Stokes equation simplifies to the linear Stokes equations:

$$\begin{aligned} 0 &= -\nabla P + \eta \triangle \mathbf{u} + \mathbf{f} \\ 0 &= \nabla \cdot \mathbf{u} \end{aligned} \tag{2.11}$$

Note that the flow field has no explicit time dependency in the low Reynolds number limit, which has important consequences for hydrodynamic interactions on the cell-scale.

In order to create a net propulsion the beat pattern of the propulsion device has to break time-reversal symmetry (Purcell, 1977). Using the length and time scales of typical microswimmers beating, the Reynolds number calculation is straightforward. The fastest time scale in the motion of the flagellated swimmers is the beating of the flagellum. Assuming oscillatory motion the Reynolds number is $\mathrm{Re} = \frac{fL^2}{\nu_{water}}$. Given a typical length scale of a flagellum is $L = 50\mu m - 100\mu m$, the beat frequency is $50 - 100Hz$ and the kinematic viscosity of water $\nu = 10^{-6}Pas$, a low Reynolds number $Re \approx 0.02$ follows. The squared dependency on the length makes the Reynolds number sensitive on the chosen length scale of the problem. Therefore, the largest length scale, the length of the flagellum, and the fastest time-scale are chosen, leading to an upper bound, which shows that all motion is clearly in the low Reynolds number regime.

Using the linearity of the Stokes equation a Green's function approach is an elegant way to solve these equations. The Green's function $\overleftrightarrow{G}$ is the particular solution of Eq. (2.11) for a delta force distribution. Though it needs to be derived for the given boundary conditions. It allows for a straight-forward calculation of the flow field created by arbitrary force densities $\mathbf{f}(\mathbf{r})$:

$$\mathbf{u}(\mathbf{r}) = \int\limits_{\mathbf{r} \neq \mathbf{r}'} d\mathbf{r}' \, \overleftrightarrow{G}(\mathbf{r}, \mathbf{r}') \, \mathbf{f}(\mathbf{r}') \tag{2.12}$$

Thus, given an appropriate Greens function, the knowledge of the forces applied upon the medium allows straight-forward determination of the flow field. However, it still remains difficult to obtain the Green's function G in complex geometries. Therefore, the relatively simple Green's function for an infinite volume and an infinite boundary are discussed here. The Oseen tensor gives the solution of the Stokes equations (Eq. 2.18) with open boundaries $\mathbf{u}(\mathbf{r} \to \infty) = 0$ for a delta force at position $\mathbf{r}$, a so called Stokeslet:

$$\overleftrightarrow{G}^{Oseen}(\mathbf{r}_i, \mathbf{r}_j) = \overleftrightarrow{G}^{Oseen}(\mathbf{r}_i - \mathbf{r}_j) = \overleftrightarrow{G}^{Oseen}(\mathbf{r}_{ij}), \tag{2.13}$$

where the indices of the matrix are:

$$\left(\overleftrightarrow{G}^{Oseen}(\mathbf{r}_{ij})\right)^{\alpha\beta} = \frac{1}{8\pi\eta\, r}(\mathbf{1} + \frac{r_{ij}^{\alpha} r_{ij}^{\beta}}{r^2}) \quad \text{for i} \neq \text{j}, \tag{2.14}$$

with $r = |r_{ij}|$. Similar to the electrodynamic deviation of the electric field above a planar infinite surface with the help of image charges, the flow field above an infinite half plane at $z = 0$ has been derived by Blake (1971). Starting from a Stokeslet in the positive half space $z > 0$, imaginary ‘charges‘, can be placed in the negative half space $z < 0$ in such a way that they fulfill the no-slip boundary condition. Additionally, to a mirror Stokeslet with inverted z-coordinate, a stokes-doublet and a source-doublet are needed:

$$\overleftrightarrow{G}^{\text{Blake}}(\mathbf{r}, \mathbf{r}') = \overleftrightarrow{G}^{Oseen}(\mathbf{r}, \mathbf{r}') - \overleftrightarrow{G}^{Oseen}(\mathbf{r}, \bar{\mathbf{r}}') + \overleftrightarrow{G}^{D}(\mathbf{r}, \bar{\mathbf{r}}') - \overleftrightarrow{G}^{SD}(\mathbf{r}, \bar{\mathbf{r}}'), \tag{2.15}$$

$$\text{where } \bar{\mathbf{r}} = (r^x, r^y, -r^z)^T$$

The individual contributions are:

$$\left(\overleftrightarrow{G}^{D}(\mathbf{r}_i, \mathbf{r}_j)\right)^{\alpha\beta} = \frac{2\,(r_j^z)^2(1 - 2\delta^{\beta z})}{8\pi\eta} \left(\frac{\delta^{\alpha\beta}}{r^3} - \frac{3 r_{ij}^{\alpha} r_{ij}^{\beta}}{r^5}\right) \tag{2.16}$$

$$\left(\overleftrightarrow{G}^{SD}(\mathbf{r}_i, \mathbf{r}_j)\right)^{\alpha\beta} = \frac{2\,(r_j^z)^2(1 - 2\delta^{\beta z})}{8\pi\eta} \left(\frac{\delta^{\alpha\beta} r_{ij}^z}{r^3} - \frac{\delta^{\alpha z} r_{ij}^{\beta}}{r^3} + \frac{\delta^{\beta z} r_{ij}^{\alpha}}{r^3} - \frac{3 r_{ij}^{\alpha} r_{ij}^{\beta} r_{ij}^{z}}{r^5}\right), \tag{2.17}$$

where $r = |\mathbf{r}_{ij}| = |\mathbf{r}_i - \mathbf{r}_j|$.

2.1.4 Mobility and Flow Field of a Sphere

The drag force needed to move a solid sphere of radius r_a with a velocity $\mathbf{u}$ through a resting fluid is given by the famous Stokes law. It follows from integrating the stress tensor of the fluid over the surface of the sphere:

$$\mathbf{F}^d(\mathbf{r}) = 6\pi\eta r_a \, \mathbf{u}(\mathbf{r}) = (\mu_0)^{-1} \, \mathbf{u}(\mathbf{r}). \tag{2.18}$$

Here, the self-mobility of a sphere $\mu_0 = 1.0/(6\pi\eta r_a)$ is introduced. It captures the stickiness of the medium, i.e. how easily the sphere can be moved through the medium. The inverse of the self-mobility is called the friction coefficient, which is the proportionality factor between the spheres velocity and the drag force. The drag force, exerted by the sphere on the fluid, sets the fluid in motion and creates a flow field.

In first order the far-field of the flow $\mathbf{u}(\mathbf{r}_i)$ created by the sphere is described by the drag force exerted into the fluid at the spheres center of mass position $\mathbf{r}_j$.

$$\mathbf{u}(\mathbf{r}_i) = \int \overleftrightarrow{G}(\mathbf{r}_i, \mathbf{r}_j) \, \mathbf{F}^d(\mathbf{r}_j) \tag{2.19}$$

The presence of a surface, with normal orientation $\mathbf{n}$, reduces the self-mobility of the sphere and renders it direction dependent:

$$\overleftrightarrow{\mu_0}(\mathbf{r}) = \mu_\perp \mathbf{n} \otimes \mathbf{n} + \mu_{||} \left(\mathbf{1} - \mathbf{n} \otimes \mathbf{n}\right), \tag{2.20}$$

with the reduced mobility coefficients for movement parallel to the surface $\mu_{||}$ and perpendicular to the surface $\mu_\perp$:

$$\begin{aligned} \frac{\mu_{||}}{\mu^0} &= 1 - \frac{9r_a}{16z} + o\left(\frac{r_a}{z}\right)^3 \\ \frac{\mu_\perp}{\mu^0} &= 1 - \frac{9r_a}{8z} + o\left(\frac{r_a}{z}\right)^3 . \end{aligned} \tag{2.21}$$

Note the divergences for $z \to 0$, where the far field approximation breaks down and the full hydrodynamic solution yields a logarithmic dependency.

2.1.5 Swimmer as Hydrodynamic Dipoles

A macroscopic object that is moving through a resting fluid creates a flow field, which can be constructed from the stress on its surface:

$$\mathbf{u}(\mathbf{r}_i) = -\oint_{S(V)} \overleftrightarrow{\sigma}(\mathbf{r}_j)\mathbf{n}_j \overleftrightarrow{G}(\mathbf{r}_i, \mathbf{r}_j) dS \tag{2.22}$$

The flow field created by a rigid particle can be described by a multi-pole expansion, analogous to electrodynamics, which is limited here to the first terms of the expansion, neglecting the effect of the size of the swimmer and rotation:

$$\mathbf{u}(\mathbf{r}_i) = f_0 \overleftrightarrow{G}^{Oseen}(\mathbf{r}, \mathbf{r}') + f_1 \overleftrightarrow{G}^{Dipole}(\mathbf{r}, \mathbf{r}', \mathbf{e}), \tag{2.23}$$

where $\mathbf{e}$ is the orientation of the dipole. A dipole built from two forces of equal strength, but opposing directions, separated by distances d, is shown in Fig. 2.1.

A microswimmer is force and torque free (Kim and Karrila, 2013; Lauga, 2014; ten Hagen et al., 2015). It propels by drag-induced thrust, generated by the anisotropy of its mobility and periodic shape which are not time-reversible. Therefore, no force monopoles can exist, $f_0 = 0$ and the leading order contribution to the flow field becomes a dipole. The dipole has a force density $\pm f_1$. These coarse-grained far-field interactions distinguish swimmers between pushers,$f_1 > 0$, and pullers, $f_1 < 0$. A pusher propels by pushing the cell body through the fluid, e.g. a sperm cell, whereas a puller pulls the cell body, like Chlamydomonas. The difference in propulsion mechanism creates substantially different flow fields, that result in different alignments of swimmers. The far-field of a puller type swimmer aligns pullers perpendicular to surfaces, whereas pushers are aligned parallel. More details can be found in the paper of Spagnolie and Lauga (2012).

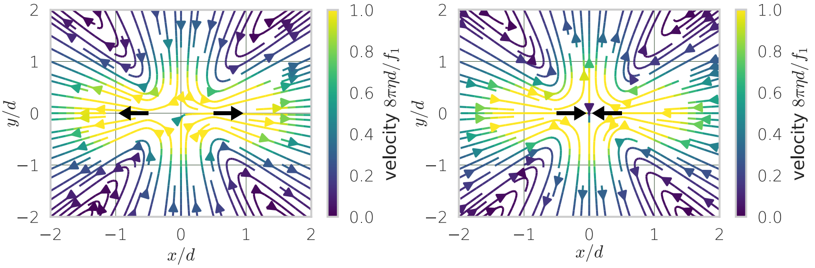

Figure 2.1 **Dipole flow field** - Streamlines of the flow field created by two monopoles, separated at a distance d, describing the far field of a pusher $f_1 > 0$ (left) and puller $f_1 < 0$ (right) type swimmer. The color indicates the absolute value of the velocity.

2.2 Particle-based Simulation Methods

2.2.1 Introduction

In order to go beyond the dipole-swimmer approximation the motion of the swimmer is modeled explicitly. In case of the beating flagellum, these are bending and twist motion along the flagellum. These internal degrees of freedom have to be modeled and coupled via hydrodynamic interactions. Active swimmers exert forces onto the fluid and at the same time they move within the flow these forces are creating. Since the swimmer has internal degrees of freedom the forces it exerts on the fluid have to be resolved on a smaller scale. Numerically, this is done by discretizing the shape of the swimmer by beads (Ainley et al., 2008; Bailey et al., 2009; Lowe, 2001) and calculate the force acting on them, due to the internal degrees of motion in the swimmer. The motion of these beads is obtained by integrated plain Newtonians equations of motion (section 2.2.2) with the additional adjustment of the velocity due to the flow in the system. Different ways to obtain the flow field in mesoscale systems from the forces exerted in the fluid are discussed in section 2.3.

2.2.2 Newtonian Dynamics

The dynamics of the microswimmer are described by Newton's equations of motion. Since hydrodynamic interactions have to be incorporated, the velocity needs to be available during integration. Eventually, this constrain leads to the velocity-Verlet method to integrate Newton's equations of motion.

The conservative force acting on each bead, follows from the internal energy of the system, described by the Hamiltonian $\mathscr{H}$:

$$\mathbf{F}_i^c = -\frac{d\mathscr{H}}{d\mathbf{r}_i}. \tag{2.24}$$

The displacement of each particle follows Newtonian dynamics:

$$m_{MD}\frac{d^2\mathbf{x}_i}{dt^2} = \mathbf{F}_i(\mathbf{x}_i, t), \tag{2.25}$$

which is a second order ordinary differential equation, where the force acting on a bead depends only on its position and time.

Using the central difference method to derive the position twice gives:

$$\mathbf{x}_i(t+\tau_{MD}) = 2\mathbf{x}_i(t) - \mathbf{x}_i(t-\tau_{MD}) + \frac{\mathbf{F}_i(t)}{m}\tau_{MD}^2 + o(\tau_{MD}^4), \tag{2.26}$$

where the integration time step τ_{MD} is introduced. However, in order to couple hydrodynamics the velocity component has to be calculated separately, rendering the method computationally complex. Instead the velocity can be integrated explicitly and used to correct position, providing the same integration error bound (Allen and Tildesley, 1989):

$$\begin{aligned}\mathbf{x}_i(t+\tau_{MD}) &= \mathbf{x}_i(t) + \mathbf{v}_i(t)\tau_{MD} + \frac{\mathbf{F}_i(t)}{2m_{MD}}\tau_{MD}^2 \\ \mathbf{v}_i(t+\tau_{MD}) &= \mathbf{v}_i(t) + \frac{\mathbf{F}_i(t) + \mathbf{F}(t+\tau_{MD})}{2m_{MD}},\end{aligned} \tag{2.27}$$

which is used to integrate Newtonians dynamics, when explicit velocities are necessary, e.g. for coupling to MPC-based hydrodynamic simulations.

2.2.3 Langevin Dynamics

Instead of modeling the molecular interactions between water molecules explicitly, their effect is included by integrating over the fast time scale. Using the result of the continues hydrodynamic theory for the mobility of a spherical particle (Eq. 2.18), the equation of motion is extended to include the interactions with the fluid:

$$m_{MD}\frac{d^2\mathbf{x_i}}{dt^2} = \mathbf{F}_i^c + \mathbf{F}_i^d + \delta\mathbf{F}_i, \tag{2.28}$$

where $\mathbf{F}^c$ is the conservative force, $\mathbf{F}^d$ the dissipative force and $\delta\mathbf{F}$ the random force acting on the bead. In the friction dominated regime, where the friction force is much larger than the inertia, i.e. $\mu_0 m_{MD} \to 0$, inertia can be neglected, leading to the equations for over-damped Brownian motion:

$$\frac{d\mathbf{r}_i}{dt} = \mathbf{v}(t) = \mu_0 \mathbf{F}_i(t) + \delta\mathbf{F}(t), \tag{2.29}$$

where the interactions of the beads with the fluid are included in the self mobility μ_0. In a pure dissipative system, no hydrodynamic interactions are included. The flow that the movement of the particles creates is neglected so far.

The noise has a mean value of zero, since it should not introduce average momentum. The correlation fulfills the fluctuation-dissipation theorem (Ermak and McCammon, 1978):

$$\langle \delta\mathbf{F_i(t)} \rangle = 0 \tag{2.30}$$

$$\langle \delta\mathbf{F}_i(t)\delta\mathbf{F}_j(t') \rangle = 2k_BT\ \mu_0\ \delta(t-t')\delta_{ij}, \tag{2.31}$$

where k_B is the Boltzmann constant and T the temperature of the medium.

2.3 Mesoscale Hydrodynamic Approaches

2.3.1 Introduction

The scale on which hydrodynamics are modeled depends on the system at hand. Large systems in the range of meters and time scales of seconds are often modeled in the continuum limit, described by the Navier-Stokes equation. When solved numerically, this partial differential equation has to be discretized, leading to usually quite large volumes of discretization, that allow to describe the medium solely by transport properties such as the viscosity. By fully neglecting the underlying molecular nature, very efficient simulations in the macroscopic regime are achieved. On the other end of the length and time scale, on the nanometer and nanosecond scale, molecular dynamics simulations simulate the motion of every water particle, including interactions on the atomic scales.

A mesoscale object, such as a suspended polymer with a length of several micrometers, is between these two limits. It is too small to neglect the influence of noise, due to the single particle nature of the medium, whereas the simulation of each water molecule would need around 10^{19} particles, which is computationally infeasible. Therefore, several mesoscale methods have been developed to perform efficient simulations in this regime. The momentum exchange between the object and the fluid is coarse-grained by replacing individual water molecules with effective interactions, that maintain the influence of the medium on the embedded object on a time scale, which is relevant for its motion. In Brownian-dynamics simulations the different time scales of the molecular and colloidal motion are exploited to omit the explicit simulation of molecular motion. Only the average effect of the collisions between fluid molecules and the colloid are considered by integrating over the fast, molecular time-scale and determine the flow field from the continuum solution, as described in detail in section 2.3.2.

Alternatively, the momentum exchange of water molecules can be coarse-grained by introducing fluid particles, which transport the momentum of several water molecules. In lattice Boltzmann simulation the fluid is described by particle distributions that move on a fixed lattice. Particle distributions move with a probability according to their current state from lattice site to lattice site. Particle distributions occupying the same lattice side, exchange momentum and mass, mimicking a collision of particles according to a Boltzmann transport equation. The method does conserve energy and momentum. However, no noise is introduced and the construction of the lattice can be complex especially for complex geometries.

In dissipative particle dynamics, the fluid is described by a Boltzmann gas model: Additional interactions give raise to hydrodynamic interactions. They are modeled as soft and finite interactions between fluid particles. For each pair of particles within a cut-off range a friction, a conservative and a random force are applied. The particles can be considered as the center of mass motion of a small volume of fluid. By conserving momentum and number of particles the particle distribution field couples to a continuity equation and therefore can be tuned to simulate hydrodynamic transport.

In multi-particle collision dynamics, presented in section 2.3.3 in detail, the fluid is again described as gas with modified collision rules. Particles move freely in the streaming step. Space is divided in boxes of equal size on which scale particles interact by exchange momentum. The momentum exchange is defined by a collision rule from which the transport properties of the fluid can be derived.

2.3.2 Tensor-based Hydrodynamic Simulations

In the tensor-based modeling approaches, hydrodynamic interactions between the water molecules and the beads are incorporated via a modified mobility matrix and a noise term, that includes the integrated momentum exchange between the thermal fluctuating water molecules and the bead. The flow field $\mathbf{u}(\mathbf{r},t)$ is composed of the forces the beads exert on the fluid, because the average velocity of the thermal fluctuations is zero. The linear nature of the Stokes equation allows to calculate the flow field from a superposition of the forces of the beads, according to Eq. (2.19). The particles, described by Eq. (2.29), now move relatively to the fluid, yielding:

$$\begin{aligned} \frac{d\mathbf{r}_i}{dt} &= \overleftrightarrow{\mu_0}\mathbf{F}_i + \mathbf{u}(\mathbf{r},t) + \delta\mathbf{F}(t) \\ &= \sum_j \overleftrightarrow{\mu}(\mathbf{r}_i,\mathbf{r}_j)\,\mathbf{F}_j + \delta\mathbf{F}_i(t), \end{aligned} \tag{2.32}$$

where the hydrodynamic interactions between particles are incorporated by extending the mobility matrix:

$$\overleftrightarrow{\mu}(\mathbf{r}_i,\mathbf{r}_j) = \delta_{i,j}\overleftrightarrow{\mu_0}(\mathbf{r}_i) + (1-\delta_{i,j})\overleftrightarrow{G}(\mathbf{r}_i,\mathbf{r}_j). \tag{2.33}$$

The hydrodynamic interactions introduce correlations in the mobility matrix between beads. These correlations have to be reflected in the correlations of the noise, according to the fluctuation dissipation theorem. The noise is not Gaussian anymore, but is “colored” by the mobility matrix, rendering the generation of the noise significantly more complex:

$$\langle \delta \mathbf{F_i}(\mathbf{t}) \rangle = 0 \tag{2.34}$$

$$\langle \delta \mathbf{F}_i(t) \delta \mathbf{F}_j(t') \rangle = 2k_B T \overleftrightarrow{\mu}(\mathbf{r}_i, \mathbf{r}_j)\ \delta(t-t')\delta_{ij}, \tag{2.35}$$

The integration is performed in four steps to exploit symmetries of the hydrodynamic interactions:

1. Calculating the conservative forces according to the current position and time of each bead.
2. Determine the only position-dependent mobility tensor for the entire system $\overleftrightarrow{\mu}$
3. Cholesky decomposition of the mobility matrix to “color” the noise
4. Move the particles according to brownian dynamics (Eq. 2.32)

The first two steps depend on the position of each bead, whereas the last step boils down to a multiplication of the mobility matrix $\overleftrightarrow{\mu} \in \mathbb{R}^{3N \times 3N}$ with the combined force vector $\mathbf{F}_g \in \mathbb{R}^{3N}$.

The combined force vector simply concatenates the forces acting on all particles. The mobility matrix $\overleftrightarrow{\mu}$ describes the hydrodynamic interactions between all particles. Since these interactions are symmetric, the mobility matrix is symmetric as well $\mu_{ij} = \mu_{ji}$. An additional symmetry for open systems is $\mu_{ij}^{\alpha\beta} = \mu_{ij}^{\beta\alpha}$. These symmetries allow to simplify the construction of the mobility matrix and the time-consuming matrix multiplication, which is needed to move the particles. The interaction tensor $\overleftrightarrow{G}(\mathbf{r}_i, \mathbf{r}_j)$ depends on the boundary conditions. The tensor, used in this work, describes open boundaries (Eq. 2.14) or motion closed to a surface (Eq. 2.15). Since the generation of the correlated noise is computationally expensive, the simulation performed in this work is done at the zero temperature, i.e. without noise. For simulations where noise has to be considered multi particle collision dynamics (MPC) simulates hydrodynamic with noise in a computational affordable manner, as explained in section 2.3.3 in detail.

For simulations it is useful to introduce the following nondimensionalized units: $r \to r/r_a$ and $F \to F/F_0$, where F_0 is a typical force scale of the system and r_a the radius of the beads used to model the microswimmer. The self-mobility of the beads given by (Eq. 2.18) sets the time scale of the simulation $t \rightarrow t\mu_0 F_0/r_a$.

2.3.3 Multiparticle Collision Dynamics (MPC)

Multi particle collision dynamics (MPC) is a meso-scale, particle based simulation method allowing for highly parallelized, efficient simulations (G. Gompper et al., 2009; Malevanets and Kapral, 1999; Ripoll, Mussawisade, et al., 2004). The fluid consists of an ensemble of point particles of mass m_{MPC}. Successively, in each time step, a collision and streaming step is performed. In the streaming step, each particle moves freely with its current velocity. Instead of calculating the collisions of each particle, particle interactions are coarse-grained by introducing a box grid, that splits the simulation box into equal boxes of edge length a. Particles in one box collide collectively, hence the name “multi particle collision dynamics”.

Particles interact in the collision step, shown in Fig 2.2 . Particles in a given box exchange momentum by applying a unitary transformation R to their relative velocities:

$$\mathbf{v'}_i = \bar{\mathbf{u}}(t) + \overset{\leftrightarrow}{R} \left(\mathbf{v}_i(t) - \bar{\mathbf{u}}(t)\right), \tag{2.36}$$

where $\mathbf{u}(t)$ is the center of mass velocity of all particles in the box. The unitary transformation ensures that momentum per box is conserved. There are several choices for $\overset{\leftrightarrow}{R}$ leading to different transport coefficients. Here, SRD is used, where a collision rotates the relative velocities in each box around a randomly chosen axis. A point on the unit sphere defines the random axis in three dimension. Two random numbers, $\phi \in [0, 2\pi]$ and $u \in [-1, 1]$, describe an equal distribution of random points on the unit sphere. In each simulation step a rotation axis per box has to be chosen randomly. $\overset{\leftrightarrow}{R}$ is the rotation matrix around this axis with a fixed angle $\alpha_{MPC} = 130^\circ$.

In the following streaming step fluid particles move freely with the new velocity $\mathbf{v}'$. No interactions between fluid particles happen during the streaming time step time τ_{MPC}:

$$\mathbf{r}_i(t+\tau_{MPC}) = \mathbf{v}'_i(t)\tau_{MPC}. \tag{2.37}$$

Due to the small mean free path length $\tau_{MPC}\sqrt{k_bT/m_{MPC}}$ a particle interacts several times with the same surrounding particles, which introduces correlations due to the boxing. A shift of the boxing grid at each time step restores Galilean invariance (Ihle and Kroll, 2003). The boxing grid is shifted by a value between 0 and a in each dimension.

The collision step introduces noise and long-range hydrodynamic correlations between particles. The viscosity of the fluid due to the kinematic and collision contributions $\eta = \eta_{kin} + \eta_{col}$ and the diffusion constant D depend on the collision step, the mpc time step and the particle density ρ of the fluid and are given by:

$$\begin{aligned}
\frac{\eta_{\text{kin}}}{\rho k_b T\tau_{MPC}/2m_{MPC}} &= \frac{5\rho}{\left(\rho-1+e^{-\rho}\right)\left(2-\cos(\alpha_{MPC})-\cos(2\alpha_{MPC})\right)} - 1 \\
\frac{\eta_{\text{col}}}{\rho a^2/\tau_{MPC}} &= \frac{\rho-1+e^{-\rho}}{18\rho}\left(1-\cos\alpha_{MPC}\right), && (2.38) \\
\frac{D}{k_bTh/2m_{MPC}} &= \frac{3\rho}{\left(1-\cos(\alpha_{MPC})\right)\left(\rho-1+e^{-\rho}\right)} - 1. && (2.39)
\end{aligned}$$

In this work all simulations use a particle density of $\rho = 10a^{-3}$ particles per box, a streaming time step $\tau_{MPC} = 0.05\sqrt{k_bT/(ma^2)}$ and a MPC box size of $a = 1$. Since particles move much less than a box size per streaming step transport is dominated by the collision step which ensures fluid like behavior. Assuming thermal equilibrium with a mean velocity scale of $v^2 \approx k_bT/m_{MPC}$, the mean free path length follows as $0.05\sqrt{k_bT/m_{MPC}}$.

The momentum transfer between beads of the microswimmer and the fluid particles is done by including them in the collision step. The mean velocity of each box is calculated by adding the momentum of fluid particles and beads of the swimmer in the box and dividing it by the total mass in the box. Beads have a mass of five times the mass of the fluid particles: $m_{MD} = 5m_{MPC}$. Integration of swimmer dynamics continues to follow Newtonian dynamics, integrated via

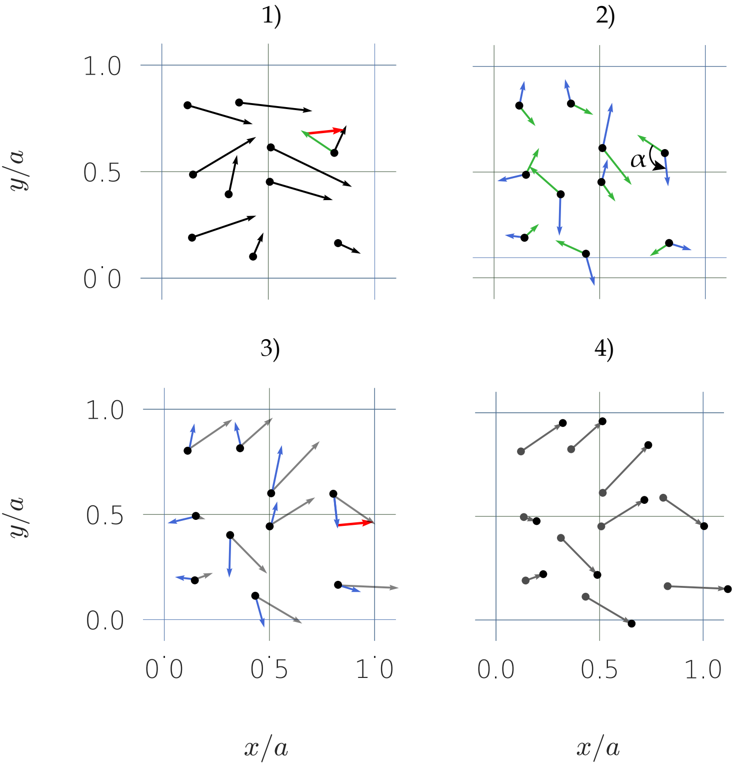

Figure 2.2 **MPC algorithm** - Sketches of the MPC steps in a box: **1)** Subtract center of mass velocity (red arrow) from all particle velocities in the box (black arrow). **2)** Rotate relative velocities (green arrow) by collision angle α_{MPC}. **3)** Adding the center of mass velocity to the rotated relative velocities (blue arrow) leads to the final velocities (gray arrow). **4)** Particles are translated along the new velocity direction in the streaming step.

Eq. (2.27) with the modification of using the bead velocity $\mathbf{v}_i$ with the updated velocity after the collision step $\mathbf{v}'$ every τ_{MPC} in the position integration step.

For the simulation of sperm swimming under confinement (section 3.1) a slightly different approach to determine the random axis of rotation is used. Here the rotations axis is chosen only from the six coordinate axes $(\pm x, \pm y, \pm z)$, which reduces the determination of random numbers to only one per box and time step.

Thermostats

The periodic motion of the microswimmer transfer energy into the fluid, which increases the fluid temperature over time. Therefore, a thermostat is needed to keep the fluid at a constant temperature T_0 by taking heat out of the system. Several different thermostats for MPC have been proposed (Huang, Varghese, et al., 2015).

The **global thermostat** re-scales the velocities of all fluid particles according to the desired temperature T_0:

$$\begin{aligned} k_b T &= \frac{1}{3N} \sum_i^N m_i \mathbf{v}_i^2 \\ \mathbf{v}_i &\rightarrow \sqrt{\frac{T_0}{T}} \mathbf{v}_i \end{aligned} \tag{2.40}$$

The global scaling introduces a difference in the density, distribution of fluid particle velocities and energies along the profile of a Poiseuille flow (Huang, Chatterji, et al., 2010). A box based rescaling of velocities overcomes this problem. The approach of a **kinetic thermostat** is to re-scale the relative kinetic energies per box according to their equilibrium distribution. Since the relative velocities in each box follow the Maxwell-Boltzmann distribution, the distribution of their kinetic energies $P(\delta E)$ can be derived as being gamma distributed, which depends on the (desired) temperature and the degrees of freedom in the system.

$$\delta E = \frac{1}{2}\sum_i m_i (v_i(t) - u(t))^2 \tag{2.41}$$

After drawing a desired energy value $\delta E'$ from the gamma distribution, the velocities in each box are re-scaled by the square root of the difference of the measured and desired energy:

$$\mathbf{v}_i \rightarrow \sqrt{\frac{\delta E'(f,T)}{\delta E}}\mathbf{v}_i. \tag{2.42}$$

In each time step the desired kinetic energy E' is drawn from $P(E';T,f)$ for each box, where T is the desired temperature and $f = 3\ (n-1)$ is the number of degrees of freedom for the relative motion of n particles in the box.

The single sperm cell simulation (chapter 3) uses the global thermostat. For the multi-ciliated sphere simulation (chapter 4), which induces a greater amount of energy and local momentum into the fluid than the single sperm cell, the kinetic thermostat is used to regulate the temperature more strictly.

Slip and No-Slip Boundaries

Boundary conditions impose conditions on the flow field. The velocity component normal to the surface vanishes, since no flow through the surface is possible. Slip is the flow tangential to the surface. A no-slip condition allows no relative motion between the surface and the fluid whereas a perfect slip boundary condition does not restrict the tangential velocity of the fluid along the surface. In the co-moving reference frame of the surface, the Dirchlet boundaries can be stated in the following from:

$$\mathbf{n}(\mathbf{r}) \cdot \mathbf{v}(\mathbf{r})|_{\mathbf{r}=\text{surface}} = 0 \qquad \text{(slip)}, \tag{2.43}$$

$$\mathbf{v}(\mathbf{r})|_{\mathbf{r}=\text{surface}} = 0 \qquad \text{(no-slip)}, \tag{2.44}$$

where **n** is the normal vector of the surface.

In MPC a no-slip boundary is implemented by a bounce back of the particle that is hitting the surface. If a particle crosses the boundary in the streaming step, its velocity is inverted exactly at the impact point, bouncing it back to the correct side of the boundary. Additionally, ghost particles of zero average velocity are filled into each MPC box that contains parts of the boundary until the particle density ρ is reached. This suppresses density fluctuation and improves the zero velocity constrain in the box describing the no-slip surface. Since hydrodynamic is resolved on the box level, it has been shown that these added ghost particles provide the main contribution of the enforced zero velocity constrain of the no-slip boundary condition. A slip boundary is implemented by simply reversing the velocity component normal to the surface.

No-Slip Boundary Conditions for Sperm Cells in Micro Channels

For complex boundaries the bounce-back of the no-slip boundary is simplified. Instead of calculating the exact intersection between the trajectory of the fluid particle and the wall, the velocity of the particle hitting the wall is inverted at the position before it crosses the wall, i.e. the bounce back is done in a layer of thickness $\mathbf{v} \cdot \mathbf{n}\ \tau_{MPC}$, where $\mathbf{v} \cdot \mathbf{n}$ is the particle velocity normal to the surface. The error introduced here is small, since the fluid velocities are of the order of one and therefore the thickness of the layer is $\ll 1$.

2.4 Axoneme Model

2.4.1 Introduction

In spirit of minimalistic modeling, the focus here lies on these essential features of the beat pattern of sperm cell flagella and the cilium. In the coarse-grained approach the beat shape is described by a semi-flexible filament. Here, two models are presented to discretize the three-dimensional filament structure and couple its internal dynamics to hydrodynamics.

2.4.2 Sperm Model

Although the specific structure of sperm cells differs a lot across species they follow a common shape. The genetic material is located in a relatively big head, which is pushed through the fluid by the much smaller flagellum. The pusher-type swimmer with a spherical head and beating flagellum is described by a sperm model based on Elgeti, Kaupp, and Gerhard Gompper (2010), which demonstrated realistic trajectories in bulk and close to planar walls. The head of the sperm cell is approximated by a sphere of radius $r_h = 2\ a$ that is modelled by $N_b = 163$ beads with one bead in the center and 162 beads uniformly covering the surface of the sphere. All surface beads are connected to their next neighbors forming a triangulated dense mesh. They are as well connected to the center bead. The flagellum is constructed out of four semi-flexible filaments and is connected by stiff springs to the spherical head so that it can still rotate around its central axis $\mathbf{e}$. The first bead of each filament is connected to the center bead, while the fourth bead of each filament is in connection to the closest bead on the surface of the sphere.

The four filaments (0,1,2,3) mimic the flagellum structure (Fig. 2.3). They are arranged in a rhombic cross section with a side length equal to the bond length $l_b = 0.5\ a$. Each filament consists of $N_f = 100$ beads which are connected by stiff springs. This results in a total flagellum length $L = 25\ r_h$ composed of 49 segments. The beat pattern is imposed along the flagellum by changing the bond lengths of the two active filaments 0 and 2 $l_i^{0,2}$, whereas the bond lengths of filament 1 and 3 are kept constant at the bond-length value l_b. The passive filaments stabilize the structure. Two passive and two active filaments oppose each other rendering the structure symmetric with respect to the center of the cross section. To stabilize the structure the beads are connected by additional springs: five springs within the cross section and two springs for four of the face-diagonals between successive cross sections. Four cross-section springs connect the four beads within a cross section with their two closest neighbors. Additionally, they connect the two beads belonging to the passive filaments (1-3). Finally, two cross-segment springs along the diagonals between successive cross sections stabilize the three-dimensional structure. Eight additional cross springs are added for the four outer faces 0-1, 1-2, 2-3 and 3-0. The face 1-3 between the two passive filaments is as well connected by two cross springs to stabilize the structure.

The beat shape is imposed along the filament by changing the bond length of the active filaments $l_i^{0,2} = l_b \pm \delta l_i$, where the arc length parametrization along the filament s is discretized per segment, i.e. $s = l_b i$. A sinusoidal beat shape is imposed along the flagellum by $\delta l(s,t) = A \sin(2\pi/\lambda\ s - \omega t)$, where s is the arc-length position along the filament, A the amplitude, λ the wavelength and $\omega = 2\pi/\tau_b$ the frequency (period) of the beating activity. In order to include the stiff-neck part of the flagellum, the bond length for beads below $i < 10$ is not changed. Diagonal springs connection active (0-2) and passive filaments (1-3) are adapted as well.

The bond-length difference between the two active filaments, which are separated with a normal distance of $l_b \sin(\pi/3)$, creates an equilibrium in-plane curvature of the filament $\kappa(s,t) = (l_b^2 \sin(\pi/3)^{-1}\delta l_{1,2}(s,t)$. The local tangent angles Ψ describes the orientation of the filament in the beat plane. In the limit of zero beat frequency $\omega = 0$, the angle of the local tangent relates to the curvature by $\Psi(s) = \int_{s0}^{s} \kappa(s')ds'$, where s0 is the end of the stiff neck part. Evaluating the integral leads to

$$\Psi(s,t) = -\frac{A\lambda}{2\pi l_b^2 \sin(\pi/3)} \cos(s\ 2\pi/\lambda - \omega t). \tag{2.45}$$

Assuming a straight orientation along the x-axis and small Ψ, the maximal beat shape amplitude above the x-axis is:

$$y(s,t) = \int_{s0}^{s} \Psi(s')ds' = -B_0 \sin(s\ 2\pi/\lambda - \omega t) \tag{2.46}$$

The beat shape amplitude scales proportional to the squared wavelength λ (Charles J Brokaw, 1971): $B_0 = -A(\frac{\lambda}{2\pi l_b})^2 \frac{1}{\sin(\pi/3)}$.

For $\omega > 0$ the difference in imposed equilibrium curvature and actual curvature of the flagellum leads to effective torques which bend the flagellum. Since the bending takes place along the filaments 0 and 2, the torques define the beat plane (Fig. 2.4). The current configuration of the sperm cell is characterized by the center of mass of the head and the three principle axes of the gyration

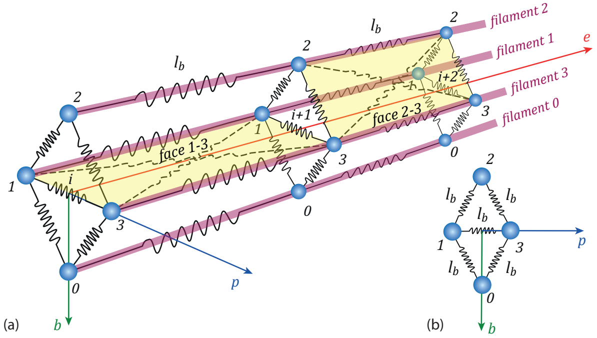

Figure 2.3 **Axoneme construction** - **(a)** Three successional segments along the axoneme are shown in the local coordinate system, described by the principle axes of the gyration tensor **e**, **b** and **p**. **(b)** Each cross section consists of four beads, labeled 0, 1, 2 and 3 (blue spheres) that are arranged in the same rhomb-shaped cross section with equal side length l_b. Springs connecting these beads are shown as thin lines with a zigzag pattern. The filaments (red) 1 and 3 are passive and provide stability, whereas the filaments 0 and 2 are actively shortened/stretched. They define the beat plane of the sperm cell. Additional springs provide stability for the rhomb-shaped structure: five springs within the cross section, four diagonal springs on each of the outer faces and four diagonal springs stabilizing the passive filaments of successive cross sections. Note that for clarity only the four diagonal springs (red) on the outer face 2-3 (yellow) between segment $i+1$ and $i+2$ and the inner face 1-3 between segment i and $i+1$ are shown. Springs connecting the faces 0-1, 1-2, 2-3, 3-0 and 1-3 between all successional segments are not shown.

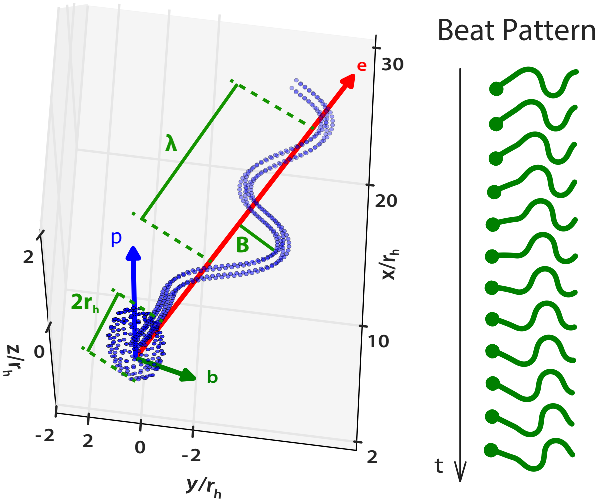

Figure 2.4 **Principle axes of the sperm cell** - The left side shows a snapshot of the beating sperm cell with beat shape parameters $\lambda = 0.63\ L$ and $A = 0.05\ r_h$ along with the orientation of the principle axes of the gyration tensor **e**, **b** and **p** in the 3D lab system. r_h is the radius of the spherical head. The series of snapshots on the right shows the time development of the beat pattern in the **eb**-plane. $B(s,t) \leq B_0 = 5.8\ r_h$ measures the beat amplitude along **b** (in-plane).

tensor of the flagellum: **e** the main axis of the flagellum, **b** the beating direction and **p** the beat-plane normal (details in A.1).

Following the theoretical calculation from Lighthill (1989) for a sinusoidal beating axoneme the average swimming velocity scales like $v \propto B_0^2\ \omega/\lambda \propto A^2\ \omega\lambda^3$.

2.4.3 Ciliary Beating

The cilium model used in this work is based on the model by Elgeti and Gerhard Gompper (2013), which shows metachronal coordination mediated by the hydrodynamic interactions between cilia. Technically the cilium model is based upon the flagellum model of the sperm cell described in section 2.4.2. But now it consists of only three rods that form a triangular cross section, i.e. rod 3 from the sperm-flagellum model is removed. The cilium is bent by only changing the bond length of filament 0. Instead of pre-imposing the beat pattern, as in the sperm model, the bond-length change along the active filament δl_i^0 depends on the mean curvature of the cilium and the local tension. The length of the diagonal springs connecting the active (0) and the passive filaments (1-3) are adapted as well, which provides structural stability for a wide range of cilia lengths and simulation parameters. Each filament of the cilium of length L is described by $N_F = L/l_b$ beads. The first part of the cilium, $i < n_0$, is passive and stays at the bond-length value $\delta l_{i<n_0} = l_b$.

The beat pattern is controlled by a heuristic model that can be controlled by a few key parameters and allows feedback to external flow. It is regulated by making the equilibrium curvature along the cilium depended on the mid-point. Thus, the bond length along the active filament is defined by:

$$\begin{aligned}
\delta l_i(t) &= A\left(1-\frac{i-n_0-1}{N_F-n_0-1}\right)^{2.5}\cdot\left(1-\frac{1}{i_0-i-1}\right) && \text{for } i < i_0-2 \\
\delta l_i(t) &= -\frac{2A}{(i-i_0)^2+1} && \text{for } i \geq i_0-2 \qquad (2.47)
\end{aligned}$$

The start and the end of the active beat pattern is defined by the arc-length indices $n_0 \leftarrow s_0/l_b$ and $n_0 \leftarrow L/l_b$. The difference between power and recovery stroke depends on the mid-point position i_0. During the power stroke, the mid-point is set to the first point of active beating n_0. It stays at this value, until the mean curvature of the flagellum reaches the negative power-stroke threshold Q^P. Then, during the recovery stroke, the mid-point i_0 moves along the cilium with a constant velocity $v_{recover}$ until the mean curvature reaches the positive recovery-stroke threshold Q^R.

The mean curvature of the cilium is given by:

$$Q = n_L l_b^2 C = \sum_{i}^{n_L} 2\, r_2^i - r_1^i - r_0^i, \tag{2.48}$$

with $r_i^j = |\mathbf{r}_{i+1}^j - \mathbf{r}_i^j|$ is the length of the tangent vector at position i along filament j.

The point of highest curvature is close to the mid-point i_0. The beat frequency emerges from the movement of the mid-point in the recovery stroke and the limiting motion due to the maximum allowed force that can be applied due to the stall force of the motors.

A mechanism simulating the stall force of dynein motors according to Elgeti and Gerhard Gompper (2013) is implemented. This implements a Brownian ratchet like potential for the motors. If the local tension along the filament is above the stall threshold the bond length is not changed. However, it always inhibits reverse motion, i.e. a change of the bond length that would lead to a change of mean curvature away from the mean curvature threshold. Note, that this prohibition of backwards motion and the high noise of MPC simulation provides the main driving mechanism of the cilia beat. During the power stroke the system acts like a Brownian ratchet that moves towards the equilibrium curvature, whereas the recovery-stroke is mainly dominated by the speed of the mid-point movement $v_{recovery}$.

Control parameters of the cilia beating are the length L of the cilium, the beat amplitude A, the maximal Q^P and the minimal mean curvature Q^R, the speed of the mid-point $v_{recover}$ and the maximal force a motor can exert before stalling. The parameters used in the simulations are summarized in Table B.1.

2.4.4 Kirchhoff Model of Semi-flexible Filaments

The flagellum is described as an elastic filament of constant length with three independent deformation modes. The filament can be bend along two perpendicular directions $\mathbf{e}^1$ and $\mathbf{e}^2$ and twisted along the tangent axis $\mathbf{e}^3$ (Fig. 2.5). A mathematical description of this filament is given by the space-curve $\mathbf{r}(s,t)$ along the center-line and its intrinsic twist, i.e. the change of the material-frame orientation along the space curve.

However, the normal (and bi-normal) orientation of the flagellum is difficult to measure experimentally. Without a normal orientation, the Frenet frame mathematically defines a normal orientation consistently along the space-curve. In general, both frames describe a rotation along the space curve. This allows to introduce internal twist along the filament to discuss the relation between the Frenet frame orientation and the material frame orientation. In the second part of this section the Hamiltonian for the elastic filament is presented which is used to simulate sperm like beat patterns.

The Frenet frame of the curve $\mathbf{r}(s,t)$ is defined by choosing the frame so that $\mathbf{n}$ and $\mathbf{m}$ are oriented in such a way that the out-of-plane curvature is zero. The normal orientation follows from the derivative of the tangent vector $\mathbf{t}$ and the bi-normal $\mathbf{m} = \mathbf{t} \times \mathbf{n}$ follows by enforcing a right handed orthogonal coordinate system. The change of the Frenet frame along the space curve is given by the Frenet equations:

$$\begin{aligned}\frac{d\mathbf{t}}{ds} &= \kappa\mathbf{n}\\ \frac{d\mathbf{n}}{ds} &= \tau\mathbf{m} - \kappa\mathbf{t}\\ \frac{d\mathbf{m}}{ds} &= -\tau\mathbf{n}.\end{aligned} \tag{2.49}$$

They define the curvature κ and the torsion τ of the space curve. An inversion of these relations leads to a definition of the curvature and the twist:

$$\begin{aligned}\kappa &= \left|\frac{d\mathbf{t}(s)}{ds}\right|\\ \tau &= \frac{1}{\kappa}\frac{d\mathbf{t}}{ds}\frac{d\mathbf{m}}{ds}\end{aligned} \tag{2.50}$$

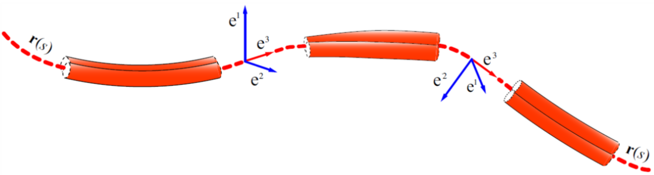

Figure 2.5 **Space curve with material frame** - Coarse-grained flagellum model with space curve $\mathbf{r}(s)$ and local reference frame $\mathbf{e}^1(s), \mathbf{e}^2(s), \mathbf{e}^3(s)$ (from: Hilfinger (2006)).

The right-handed local coordinate system $\mathbf{e}^1(s,t), \mathbf{e}^2(s,t), \mathbf{e}^3(s,t)$ describes the orientation material frame along the curve $\mathbf{r}(s,t)$(Fig. 2.5). It relates to the Frenet frame by pointing $\mathbf{e}_3(s,t)$ along the tangent vector. The perpendicular vectors $\mathbf{e}^1(s,t), \mathbf{e}^2(s,t)$ define the local cross section through the material.

The register ζ defines the intrinsic twist, i.e. how much the local material frame is twisted with respect to the Frenet frame:

$$\begin{aligned} \mathbf{n}(s) &= \cos\zeta\mathbf{e}^1 - \sin\zeta\mathbf{e}^2 \\ \mathbf{m}(s) &= \sin\zeta\mathbf{e}^1 + \cos\zeta\mathbf{e}^2 \\ \mathbf{t}(s) &= \mathbf{e}^3(s) \end{aligned} \tag{2.51}$$

For $\zeta = 0$, the normal vector $\mathbf{n}$ is parallel to $\mathbf{e}^1$ and the bi-normal vector is parallel to $\mathbf{e}^2$. Therefore, the local material frame follows the Frenet curve.

Locally, the change of orientation or angular velocity of the material can be decomposed as a rotation around each of the three local coordinate axes $\mathbf{e}_i$. The two local curvatures Ω^1 and Ω^2 and the twist Ω^3 are given by the change of the coordinate axis with respect to the arc-length. The Darboux vector $\Omega = \sum_i \Omega^i \mathbf{e}^i$ defines a pseudo vector for the angular velocity of the material frame. Infinitesimally small changes of the orientation relate to rotations around the material frame axis by $\Omega \times \mathbf{e}^i = \sum_j \partial\Omega^j R(\Omega^j|e_j)\ \mathbf{e}^i = \partial\mathbf{e}^i/\partial s$:

$$\partial_s \begin{pmatrix} \mathbf{e}^1(s) \\ \mathbf{e}^2(s) \\ \mathbf{e}^3(s) \end{pmatrix} = \begin{pmatrix} 0 & \Omega^3(s) & -\Omega^2(s) \\ -\Omega^3(s) & 0 & \Omega^1(s) \\ \Omega^2(s) & -\Omega^1(s) & 0 \end{pmatrix} \begin{pmatrix} \mathbf{e}^1(s) \\ \mathbf{e}^2(s) \\ \mathbf{e}^3(s) \end{pmatrix}. \tag{2.52}$$

The curvature $\kappa(s,t)$ and the torsion $\tau(s,t)$ of the space curve in the Frenet frame following Eq. (2.50) are given by:

$$\kappa = |\frac{d\mathbf{t}(s)}{ds}| = \sqrt{(\Omega^1)^2 + (\Omega^2)^2}, \tag{2.53}$$

$$\tau = \frac{1}{\kappa}\frac{d\mathbf{t}}{ds}\frac{d\mathbf{m}}{ds} = \Omega^3 - \zeta. \tag{2.54}$$

The infinitesimal rotation of the material frame around its three main axes relates to the Frenet frame by inverting Eq. (2.54) for the torsion and using the intrinsic twist ζ to project the curvature onto the axis of the material frame.

$$\begin{aligned} \Omega^1(s,t) &= \kappa(s,t)\sin\zeta(s,t) \\ \Omega^2(s,t) &= \kappa(s,t)\cos\zeta(s,t) \\ \Omega^3(s,t) &= \tau(s,t) + \frac{d\zeta}{ds}(s,t) \end{aligned} \tag{2.55}$$

The elastic energy integrated along the elastic flagellum is given by:

$$\begin{aligned} \mathscr{H} = \frac{1}{2}\int_0^L & K_1\ (\Omega^1(s,t) - \Omega_0^1(s,t))^2 \\ & + K_2\ (\Omega^2(s,t) - \Omega_0^2(s,t))^2 + K_3\ (\Omega^3(s,t) - \Omega_0^3(s,t))^2 ds, \end{aligned} \tag{2.56}$$

with two bending rigidities K_1, K_2 and twisting rigidity K_3. The rod can be bent along the two perpendicular axes and twist along its center-line. Ω_0^i define the equilibrium configuration of minimal energy, and determine the equilibrium shape of the filament.

Considering a Frenet curve whose torsion and curvature is known, the material frame has an additional degree of freedom: the intrinsic twist proportional to $\frac{d\zeta}{ds}$. Considering a desired space curve, several realizations are made possible by rephrasing the Hamiltonian in terms of curvature, torsion and intrinsic twist:

$$\begin{aligned} \mathscr{H} = \frac{1}{2}\int_0^L & K_1\left(\kappa\sin\zeta - \kappa_0\sin\zeta_0\right)^2 \\ & + K_2\left(\kappa\cos\zeta - \kappa_0\cos_0\zeta\right)^2 \\ & + K_3\left(\tau + \frac{d\zeta}{ds} - \tau_0 + \frac{d\zeta_0}{ds}\right)^2 ds \end{aligned} \tag{2.57}$$

Assuming a straight equilibrium shape of the filament ($\Omega_0^i = 0$) this simplifies to:

$$\begin{aligned} \mathscr{H} = \frac{1}{2}\int_0^s & K_1\left(\kappa\sin\zeta\right)^2 \\ & + K_2\left(\kappa\cos\zeta\right)^2 \\ & + K_3\left(\tau + \frac{d\zeta}{ds}\right)^2 ds \end{aligned} \tag{2.58}$$

Several models in the literature implement this Hamiltonian in a numerically stable way (Hilfinger, 2006; Vogel and Stark, 2012). For the approach used here the coupling to hydrodynamics is important. Therefore, the model is based on the work of Hu et al. (2015). The flagellum model implements this Hamiltonian using a discretized and numerically stable approach (Fig. 2.6). By explicitly modeling the local coordinate system along the filament by beads, the bending and twist deformation for all configurations are well defined and can be easily coupled to MPC simulations. Beads are placed along the center-line separated by a bond-length distance l_b. Eventually, the arc-length is discretized by the transition $\Omega^q(s,t) \rightarrow \Omega_i^q(t)$ for $q \in (1,2,3)$. Four additional beads standing normal on the bond vector between two beads on the center-line form an octahedron-shaped segment that allows to define the local orientation $\mathbf{e}^q$ along the entire filament. The five beads forming each segment are kept in the octahedron shape by strong springs. Using Eq. (2.52) the infinitesimal rotations Ω_i^q can be obtained from the current configuration of the filament in the local coordinate system. Then, the force acting on each bead of the segment can directly be obtained from the discretized version of Eq. (2.56).

The torques applied by molecular motors along the axoneme are included in the model by changing the equilibrium curvatures Ω_0^q accordingly. Throughout

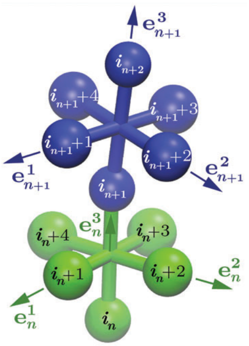

Figure 2.6 **Discrete flagella model** - Two segments of the discrete flagella modeled are shown. The orientation of each segment is described by the material frame $\mathbf{e}_n^1(s), \mathbf{e}_n^2(s), \mathbf{e}_n^3(s)$ which is modeled by the four beads i_n+1, i_n+2, i_n+3, i_n+4. Curvature and twist along the center-line can be derived from the orientation of the explicitly modeled material frames. The 12 springs ensuring the perpendicular orientation of the material frame with respect to the center-line are not shown. (from: Hu et al. (2015)).

this work motor activity is assumed to generate torques in only one bending mode, leading to the following equilibrium configuration of

$$\begin{aligned} \Omega_0^1(s,t) &= T_{active}(s,t)/K_1 \\ \Omega_0^2(s,t) &= \Omega_0^3(s,t) = 0. \end{aligned} \tag{2.59}$$

2.5 Mobility Coefficients of a Sphere, Rod and Beads

The mobility of fluid and MD particles in MPC simulations is calculated and compared to theoretical predictions, followed by the measurement of the mobility of a sphere, in order to determine its hydrodynamic radius. Since the diffusion constant is related to the mobility μ_0 by the fluctuation dissipation theorem, the mobility of a particle in a heat bath of temperature T can be easily obtained from the diffusion of a particle:

$$D = k_b T \mu_0. \tag{2.60}$$

Therefore, a straightforward way to measure the diffusion constant D, used here, is to calculate the mean-squared-displacement of a diffusing particle:

$$\langle (\mathbf{r}(t+\tau) - \mathbf{r}(t))^2 \rangle_t = 2fD\tau = 2fk_b T \mu_0, \tag{2.61}$$

where f is the number of degrees of freedom the diffusive particle can move along. In MD simulations the mobility is explicitly set, whereas in MPC simulations the mobility coefficient results from the collision step and therefore depends on a complex combination of simulation parameters. An analytic expression for the Brownian contribution can be derived (Ripoll, K. Mussawisade, et al., 2005):

$$\mu_{0,BD} = \frac{\tau_{MPC}}{m_{MD}} \left(\frac{1}{\gamma_D} - \frac{1}{2} \right), \tag{2.62}$$

where γ_D is the decorrelation factor:

$$\gamma_D = \frac{2}{3}(1 - \cos\alpha) \frac{m_{MPC}\rho}{m_{MPC}\rho + m_{MD}} \tag{2.63}$$

However, the diffusion is significantly enhanced due to hydrodynamic interactions, which are missing in this approximation. Therefore, the mobility of an embedded colloids is determined by measuring their mean-squared displacement and by using Eq. (2.61). Mobility values are summarized in Table 2.1 and agree well with the theoretical mobility of a fluid particle, given

Table 2.1 **Mobility coefficients in MPC** for different shapes and particles masses.

Shape	r_s/a	mass / m_{MPC}	δ_c	Mobility $\mu_0/\mu_{0,th}^{fl}$	$r_{hd}[a]$
particle (fluid)	-	1	–	1.185 ± 0.0002	0.12
particle (MD)	-	5		0.552 ± 0.003	0.23
sphere	2	815	0.54	0.0609 ± 0.0002	2.1
sphere	4	815	0.13	0.0465 ± 0.0002	2.7
sphere	4	3215	0.53	0.0328 ± 0.0008	3.8

by Eq. (2.39) as $\mu_{0,th}^{fl} = 0.0257\ \sqrt{a^2/(k_bTm)}$. The mobility for the MPC-simulation parameters used in this work (section 2.3.3) deviates from the Brownian approximation by $(\mu_0 - \mu_{0,BD})/\mu_{0,BD} = 0.63$.

In MPC, a single particle has no inherit size. However its hydrodynamic radius can be defined from Stokes law (Eq. 2.18) by measuring its self mobility $r_a = (6\pi\eta\mu_0)^{-1}$. MD particles have a corresponding hydrodynamic radius $r_a = 0.23\ a$, justifying the chosen bond-length of $l_b = 0.5\ a$ to model the flagellar structure (section 2.4).

The mean-squared displacement of an embedded MD particle and spheres of radius $r_s = 2\ a$ and $r_s = 4\ a$ (Fig. 2.7) allows to define the hydrodynamic radius r_{HD} of the spheres via Eq. 2.18 . The radius of the sphere should roughly match the measured hydrodynamic radius if the density of MD-particles describing its surface is high enough. The coverage of the spherical particles via beads is calculated by:

$$\delta_c = \frac{N_b \pi r_a^2}{4\pi r_s^2}, \tag{2.64}$$

where r_s is the sphere radius, r_a the hydrodynamic radius of an MD bead and N_b the number of beads covering its surface. As seen in table 2.1, a good approximation of the theoretical Stokes friction is achieved for $\delta_c > 1$. Detailed studies show that for too large bead coverage additional inertial effects occur (Poblete et al., 2014) which might explain the slightly larger hydrodynamic radius obtained for the densely covered small sphere.

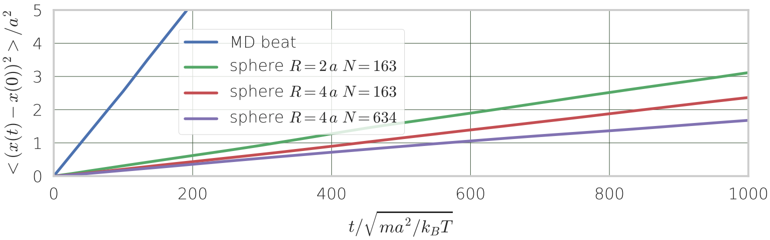

Figure 2.7 **Mean-squared displacement** - Mobility coefficients for a MD-bead and spheres of different radii, modeled by triangulated particle meshes, are obtained from a linear fit to the mean-squared displacement of the fluctuating motion, due to the thermal noise in the MPC fluid.

Long, thin and stiff filaments, called rods, provide a simple test for the accuracy of the simulation methods, since the drag resistance can be compared to theoretical results. Here, the filament is simulated using tensor-based hydrodynamic simulations (section 2.3.2). In a similar setup the match to theoretical anisotropy values of the filament model for MPC simulations has been shown by Elgeti and Gerhard Gompper (2008). The computational model for the filaments is described in section 2.4.4. The filament has a size of $L = 80\ r_a$ and a height of $d = 4\ l_b$ which results in a very small aspect ratio of $d/L = 0.05$. In the very stiff regime ($K_1 = K_2 = K_3 = 100000\ /(F_0 r_a^2)$) with a straight equilibrium configuration ($\Omega_i^0 = 0$) internal modes of the filament are suppressed. The filament is aligned along the x-direction. It gets dragged by total force $F = 0.1\ F_0$ either in x or y direction. The mobility coefficients of the rod depend on the dragging direction. By measuring the corresponding velocities, the mobility coefficient for a movement parallel $\mu_{R,\|}$ and perpendicular $\mu_{R,\perp}$ to the length axis can be obtained:

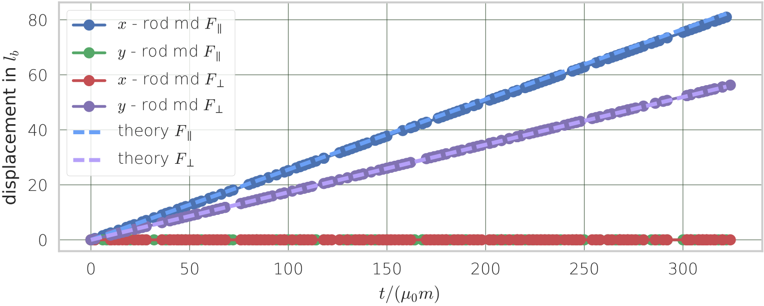

Figure 2.8 **Dragged filament** - Tensor-based hydrodynamic simulations of a filament which is dragged parallel and perpendicular to its main axis. Drag coefficient agree very well with theoretical predictions (dashed lines).

$$\frac{dx}{dt} = \mu_{R,\parallel} F_\parallel \tag{2.65}$$

$$\frac{dy}{dt} = \mu_{R,\perp} F_\perp \tag{2.66}$$

$$\tag{2.67}$$

Figure 2.8 shows the center-of-mass displacement. The mobility $\mu_{R,\parallel}$ of the filament is about 1.45 times larger when the filament is dragged along the parallel direction (x-axis) than the mobility $\mu_\perp$ in perpendicular direction (y-axis). Theoretical predictions (Löwen, 1999):

$$\begin{aligned} \mu_r\, R, \| &= \log(L/d) + 0.839 + 0.185\ d/L + 0.233\ (d/L)^2 \\ 2\ \mu_r\ \mu_{R,\perp} &= \log(L/d) - 0.207 + 0.980\ d/L - 0.133\ (d/L)^2, \\ \text{with } \mu_r &= 2\pi\eta L, \end{aligned} \tag{2.68}$$

agree very well with the simulation results. Note the strong effect of finite sized rods, due to the *log* scaling. In the limit of infinite small rods $d/L \to 0$ parallel mobility is twice the perpendicular mobility $\mu_{R,\parallel} = 2\mu_{R,\perp}$.

Chapter 3

Sperm Cells

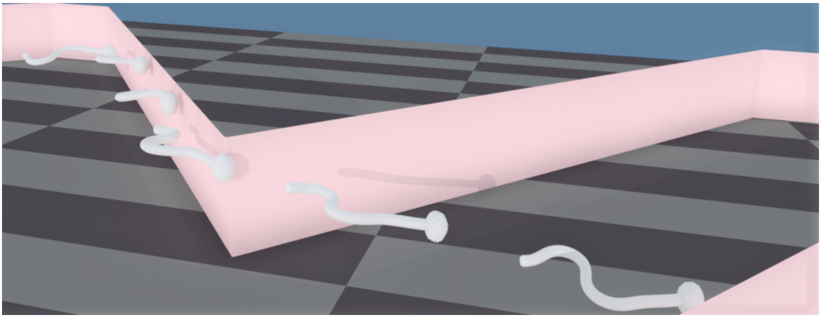

3.1 Sperm in Microfluidic Channels

3.1.1 Introduction

For fertilization mammalian sperm cells pass through the narrow windings of the Fallopian tube. Microfluidic devices that recapitulate these confined environments allow in-vitro experiments and provide an insight in surface attraction mechanisms of sperm. The simulation approach presented here shows a way to interpret these experiments and eventually understand the mechanisms of sperm guidance along surfaces.

Here I start with a studying how the beat pattern influences surface attraction in planar narrow channels. This is followed by simulation of sperm trajectories in channels with periodically modeled side walls, that closely resemble the pattern of channels used in recent micro-fluidic experiments on sperm (Denissenko et al., 2012). A visualization of such a zigzag channel is shown in an artful fashion at the beginning of the chapter. These simulations reproduce experimental results, which allow to develop a minimal, steric model that captures the average deflection of sperm around rectangular corners. Finally, attraction towards curved surfaces for planar and nonplanar beating flagella are studied.

Sperm simulated in this chapter use an imposed curvature amplitude $A = 0.05\ r_h$ (section 2.4.2), whereas beat frequencies ω and imposed wavelength λ are varied. The fluid is simulated using MPC hydrodynamic simulations (section 2.3.3).

3.1.2 Wavelength-dependent Surface Attraction

The surface attraction of sperm depends on the flagellar beat shape and the shape of the head. Here, the relation between flagellar beat shape and surface attraction for a rectangular channel is studied. It is shown, that the beat shape-envelope depends on the wavelength λ, which directly affects the surface attraction of sperm.

The beat pattern of freely swimming sperm is simulated using the sperm model presented in section 2.4.2. Hydrodynamic interactions are included using MPC in a simulation box of size $L_x = 70\ a$, $L_y = 70\ a$ and $L_z = 70\ a$ with periodic boundaries in x, y and z-direction. Sperm with two different beat frequencies $\omega = 0.05\ \sqrt{k_BT/(am^2)}$ and $\omega = 0.1\ \sqrt{k_BT/(am^2)}$ are simulated. Figure 3.1 shows the projection of the beat pattern for different wavelengths λ and $\omega = 0.1\ \sqrt{k_BT/(am^2)}$ onto the principle axis of the gyration tensor (appendix A.1).The beat-shape envelope is quantified by two opening angles: the in-plane opening angle $\delta_b(t)$ and the out-of-plane opening angle $\delta_p(t)$. They are defined by the opening angles of the triangle in the corresponding projection, which covers the beat pattern. The triangles are constructed by finding the maximal elongation along the b- and p-direction on both sides of

s_{cm}, which defines the arc-length position that splits the sperm in two parts of equal mass:

$$\tan\delta_b(t) = \frac{\max_{s''} B(s'' > s_{cm}, t) - \max_{s'} B(s' < s_{cm}, t)}{E(s'', t) - E(s', t)}, \tag{3.1}$$

where s', s'' are the arc-length positions where $B(s)$ is maximal. Doing the same for the minimum results in the upper and lower bounds of the opening angle δ_b. Because both bounds have the same value with opposing sign, due to the axis symmetry of the beating pattern, the opening angle can be defined by taking the mean of their absolute values. Finally, the time dependence is omitted by averaging over several flagellar beats.

Figure 3.2 quantifies the increase of δ_b with an increase of wavelength λ for both beat frequencies. When the wavelength increases above a threshold of $\lambda = 0.79\ L$, the flagellum buckles under the load of the viscous forces and exhibits an out-of-plane component, leading to a complex three-dimensional beating pattern (which will be considered in more detail for human sperm cells in section 3.2). The torque generated by the in-plane beat along the flagellum is counter-balanced by the head (Friedrich et al., 2010), leading also to an oscillation of the head orientation relative to the flagellum. In the planar beating regime ($\delta_p < 0$), the in-plane opening angle δ_b increases linearly with the wavelength. For slow beating sperm ($\omega = 0.05\ \sqrt{k_BT/(am^2)}$) it increases with $\delta_b(\lambda) = 30°\ \lambda/L - 6°$, whereas it increases slightly slower for fast beating sperm ($\omega = 0.1\ \sqrt{k_BT/(am^2)}$) with $\delta_b(\lambda) = 27°\ \lambda/L - 6°$. The out-of-plane opening angle δ_p behavior depends on the beat frequency. For the slow beating sperm the out-of-plane opening angle increases, while the in-plane opening angle stays constant, whereas for the faster beating sperm cell the out-of-plane opening angle increases non-linearly, almost like a short ramp. In the intermediate regime between $\lambda = 0.7$ and $\lambda = 0.79$ both the in-plane and the out-of-plane opening angle increase. Although this needs further investigation, in this section, I will focus on the effect of the beat-shape envelope on the surface attraction in close confinements.

Surface attraction is studied in an infinite planar channel by enforcing two no-slip boundaries in z-direction at $z = 0$ and $z = 24.5\ r_h$ and therefore reducing the simulation box dimension in z to $L_z = 24.5\ r_h$. Trajectories of a sperm, beating with different wavelengths and beat frequency $\omega = 0.1\ \sqrt{k_BT/(am^2)}$,

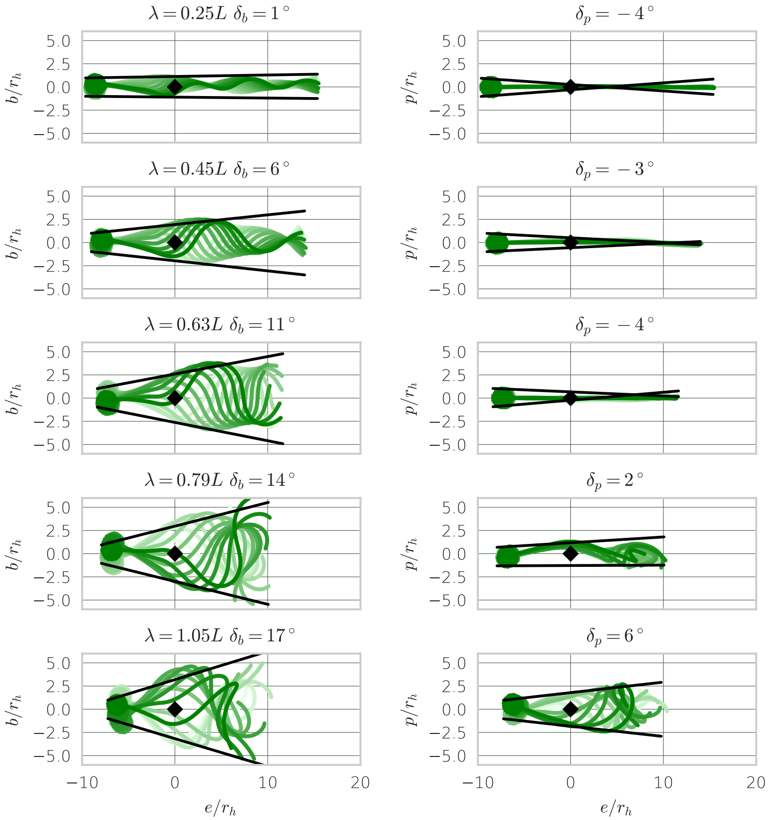

Figure 3.1 **Beat shape envelopes of sperm** - Snapshots of the beating pattern ($\omega = 0.1\ \sqrt{k_BT/(am^2)}$) are projected on the three principle axis of the gyration tensor **e**(main elongation), **b** (in-plane beating) and **p** (out-of-plane beating) colored from dark to light green with increasing time. Each row shows the beat-pattern for an imposed wavelength λ and the resulting opening angles δ_b (in-plane), δ_p (out-of-plane). Black lines indicate the corresponding beat-shape envelope. Note the increasing in-plane shape asymmetry with increasing wavelength λ, that leads to a buckling of the filament, which results in an out-of-plane beating component along the **p**-axis.

(a) $\omega = 0.05\ \sqrt{k_BT/(am^2)}$

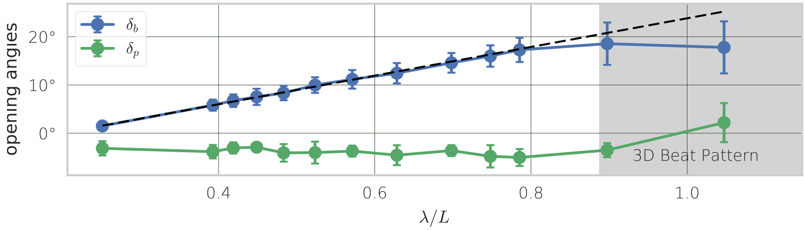

(b) $\omega = 0.1\ \sqrt{k_BT/(am^2)}$

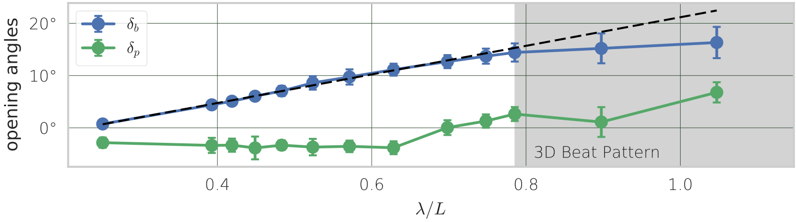

Figure 3.2 **Opening angles of the beat shape** - The in-plane opening angle δ_b of the beat-shape envelope increases linearly with wavelength λ until the out-of-plane opening angle δ_p starts to increase ($\lambda \geq 0.79\ L$). Error bars indicate the standard deviation when averages over several beats. The increase of the in-plane opening angle for the slower beating sperm **(a)** is $\delta_b/\lambda = 30°/L$, whereas the increase of the faster beating sperm **(b)** is slightly less steep with $\delta_b/\lambda = 27°/L$. Note, that only the faster beating sperm shows an intermediate regime with linear increasing out-of-plane component δ_p between $\lambda = 0.7$ and $\lambda = 0.79$.

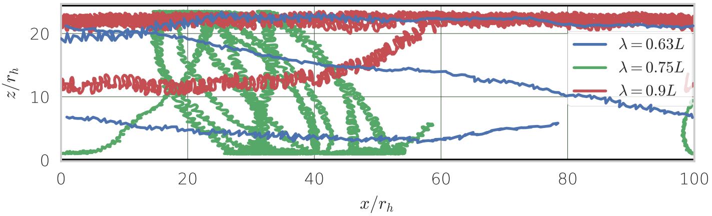

Figure 3.3 **Sperm trapping** - The trace of trajectories of the head of the sperm cell, swimming in a narrow channel of height $h = 24.5\ r_h$, is projected into the xz-plane with periodic boundaries along the x-direction. At the transition from planar to three-dimensional beating the buckling ($\lambda = 0.75\ L$) of the flagellum leads to curved trajectory, which traps the sperm cell. Sperm with larger out-of-plane beating ($\lambda = 0.9\ L$) as well as planer beating sperm cells ($\lambda = 0.63\ L$) attach to the channel boundaries and swim along them.

are shown in Fig. 3.3. Sperm tend to attach and swim along surfaces for $\lambda < 0.57\ L$. Only sperm at the transition between planar and three-dimensional beating at wavelengths between $\lambda = 0.7\ L$ and $\lambda = 0.79\ L$, detach regularly and commute between both sides of the channel. Because sperm swim on circular trajectories, they are trapped in a small segment of the channel.

The surface attraction of sperm swimming with a particular wavelength is quantified in Fig. 3.4. When sperm move more than 4 r_h away from the surface, this is called a detachment event. If sperm reach the opposite plane this is counted as a crossing event. Since crossing and detachment events are rare, they can be modeled as a Poisson process. This allows to calculate the 95%-confidence interval of both rates from the total number of events that occurred within the simulation time.

In the planar regime, the detachment rate is not affected by the change in wavelength. The rate fluctuates around a constant of 0.025 detachments per beat period, which corresponds to a detachment event for every 400 beats. None of the detachments lead to a crossing of the channel. In all cases, sperm quickly reattach to the same surface. The out-of-plane component increases detachment and crossing rates significantly up to a value of 40 beats per channel crossing for $\lambda = 0.79\ L$. A further increase of the wavelength

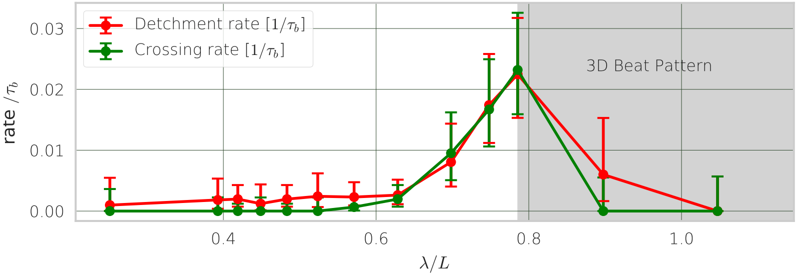

Figure 3.4 **Wavelength dependent surface attraction** - The surface attraction of sperm cells is quantified by the number of detachment events, the head of the sperm cell surpasses a distance from the channel wall $d > 4\ r_h$ (red) and the number of successful crossings of the channel (green). Error bars mark the 95% confidence-interval assuming an underlying Poisson process.

$\lambda \geq 0.90\ L$ decreases the crossing rate to zero crossing within the simulation time.

The detachment rate affects on the overall probability distribution of the center-of-mass of the sperm head at a certain distance from the surface (Fig. 3.5). In the range of no channel crossings, the sperm cell swims along the sidewall at a distance between 2 and 4 r_h. For very high wavelength, $\lambda \geq 0.90\ L$, the three-dimensional beat pattern pushes the head even more closely towards the wall, resulting in an even stronger attraction by the surface. Between $\lambda \geq 0.57\ L$ and $\lambda \leq 0.79\ L$, the probability distribution widens. Surprisingly, the average distance is largest for $\lambda = 0.63\ L$, where detachment events are rarely observed. Due to the very small out-of-plane component at this wavelength, the inclination angle at which the sperm cell detaches from the surface is smaller than the cases with larger wavelength and out-of-plane component. In the oscillating cases, the sperm cell is almost reflected at the surface, escaping the surface almost perpendicular.

The out-of-plane component directly influences the rate of detachment of sperm from the surface. In the regime of almost constant out-of-plane component $\lambda \geq 0.57\ L$, the detachment rate is constant as well. If sperm manage to detach, the flagellum is oriented away from the surface, thereby leaving the stable orientation of the planar beat parallel to the surface. However, sperm

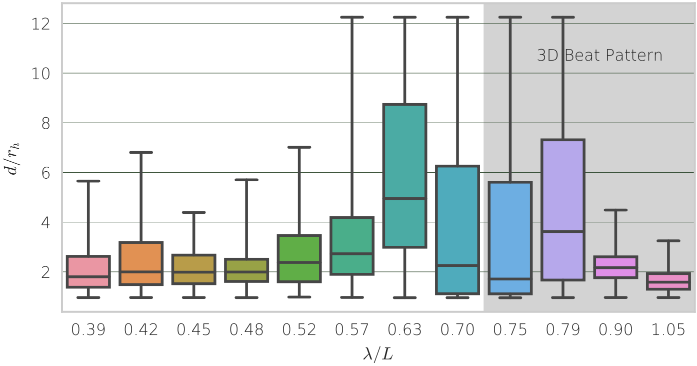

Figure 3.5 **Wavelength dependent sperm distribution in a planar channel** - The wavelength of the beat pattern highly influences the probability to find sperm at a certain distance d from one of the two surfaces of a channel with height $h = 24.5\ r_h$. The box plot indicates the probability distribution of d by the 25% and 75% percentile, the mean and the minimum/maximum value (whiskers).

need to propel fast enough to escape the hydrodynamic attraction of the surface. Although the origin of the parallel orientation of the beat plane with the surface is not completely understood, the computer simulation shows that sperm, when approaching surfaces, align their beat plane with the surface. It is thus plausible, that the presence of an out-of-plane beating component heavily influences surface attraction.

3.1.3 Rectangular Corner Deflection

The deflection of sperm swimming along the side-wall of a zigzag channel with a $\gamma = 90°$ corner is investigated. The zigzag channel is reconstructed with the same aspect ratio as used in the experiments performed by Kantsler, Dunkel, Polin, et al. (2013). The cubic simulation box has the dimensions $L_x = 400\ a$, $L_y = 400\ a$ and $L_z = 25\ a$ with periodic boundaries along the x-direction. The specific channel pattern is embedded in the simulation box and limits the motion in y-direction by two sidewalls, which are separated by a normal distance of $35.4\ r_h$. The channel is closed in z-direction at a height

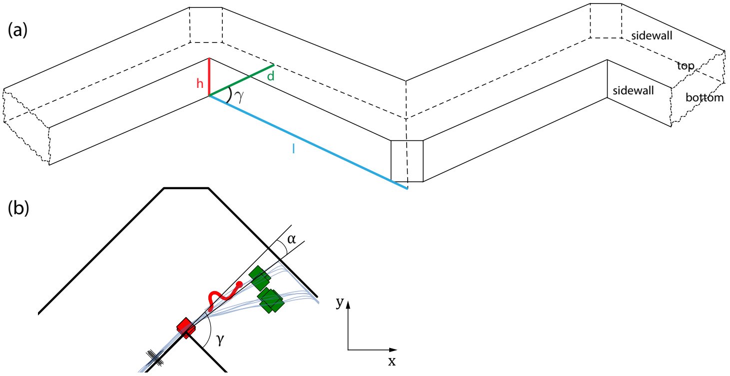

Figure 3.6 **Zigzag channel** - **(a)** The draft shows the dimensions of the zigzag channel: $d = 75\ r_h$, $h = 12.5\ r_h$ and a sidewall length $l = 100\ r_h$. The channel has $2l$-periodic boundaries in x-direction. No-slip boundaries conditions are enforced on all four faces of the channel. **(b)** Top view of the $\gamma = 90°$ corner showing trajectories of sperm cells swimming around it (blue lines). The deflection angle α is defined by the total deflection of the sperm cell orientation, starting from the red rhombus above the corner until the green rhombus when it is completely detached from the sidewall.

$h = 12.5 r_h$, leading to a narrow tunnel with a cross section of aspect ratio 2.8:1. All surfaces are no-slip boundaries. The study begins with the analysis of sperm with planar beat pattern with an imposed wavelength $\lambda = 0.63\ L$ and a beat frequency $\omega = 0.05\ \sqrt{k_B T/(am^2)}$. The channel geometry and typical trajectories of sperm deflecting around the corner are shown in Fig. 3.6. Sperm follow the sidewall – until they detach at the edge of the corner, cross the channel and reorient along the opposing sidewall.

The fan of sperm cell trajectories scattering off the edge of the channel look very similar to the experimental observations (Denissenko et al., 2012).

For a more quantitative comparison, the deflection angle α is defined the same way as in Kantsler, Dunkel, Polin, et al. (2013). The deflection α measures the turning of the sperm cell between the position when the center of the head is at the edge of the corner and its position 60 beats afterwards, when the entire sperm cell is detached from the sidewall. A change of orientation towards the

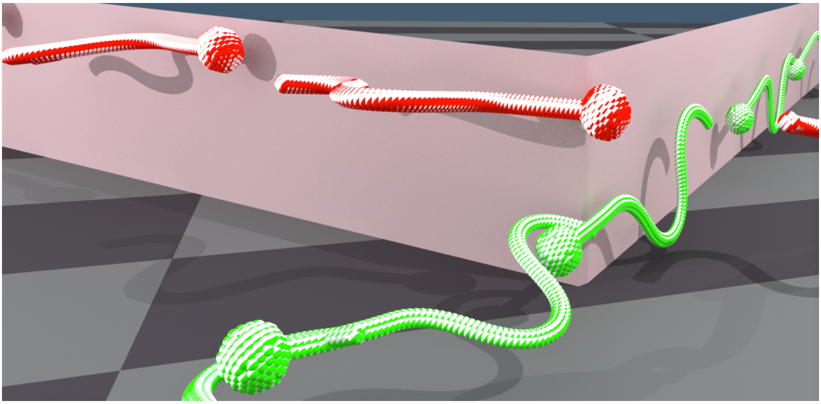

Figure 3.7 **Sperm swimming in the corner** - Overlay of a sperm cell swimming along the zigzag channel with parallel (green), $|\langle p_z \rangle| < 0.7$, and perpendicular (red), $|\langle p_z \rangle| \geq 0.7$ beat-plane orientation to the sidewall.

originating sidewall is defined as a positive α, whereas a turn away from the sidewall is defined as a negative α.

The distribution of deflection angles α (Fig. 3.8) matches surprisingly well with the experimental data (Kantsler, Dunkel, Polin, et al., 2013). The mean deflection angle is positive, $\langle \alpha \rangle \approx 15°$, with a very broad distribution from slightly negative α up to $\alpha = 45°$. Nevertheless, even for the high deflections, the sperm cell always crosses the channel and reaches the opposing sidewall, i.e. it never follows around the corner.

In contrast to experiments, simulations allow the observation of the beat-plane orientation with the sidewall. As shown in earlier works (Elgeti, Kaupp, and Gerhard Gompper, 2010), sperm orient their beat plane parallel to a nearby no-slip wall. Therefore, sperm can either align parallel to the sidewalls or to the top/bottom walls of the channel. The orientation of the beat plane is described by the beat-plane normal $\mathbf{p}$. Intermediate orientations of the sperm are rarely observed. Usually it beats either parallel to the sidewall of the channel or parallel to the top/bottom wall. Hence it is quantified as parallel $|\langle p_z \rangle| < 0.7$ or perpendicular $|\langle p_z \rangle| \geq 0.7$.

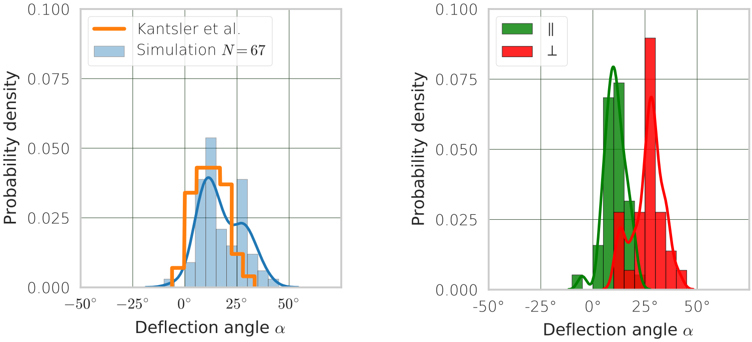

Figure 3.8 **Deflection angle distribution** - The deflection angles obtained in the simulations (blue) agree well with the ones obtained experimentally by Kantsler et al. (Kantsler, Dunkel, Blayney, et al., 2014) (orange). The solid lines show the Gaussian kernel density estimate of the underlying histogram. The distribution of deflection angles α (right plot) separates in two distinct distributions with respect to the beat plane orientation of the sperm cell towards the sidewall. The average beat plane orientation parallel (perpendicular) to the sidewall is indicated by the green (red) coloring. Note the higher deflection of the sperm cell for the perpendicular orientation. Here, the cone-like beat-shape envelope of the flagellum is pushing the cell further around the corner.

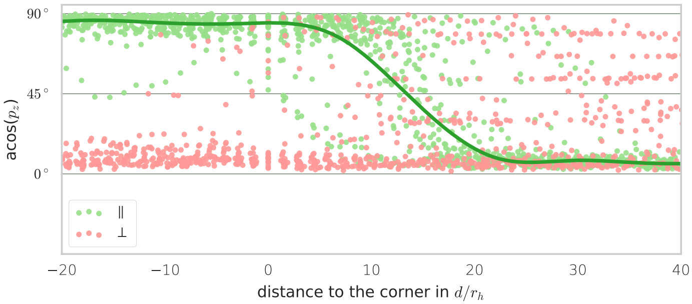

Figure 3.9 **Beat-plane orientation** - Each dot shows the tilting angle of the beat plane relative to the top wall, acos(p_z), at a distance d to the edge of the corner. Negative (positive) distances are before (after) the head of the sperm cell passes the corner. The green line is a weighted spline fit of the beat-plane orientation, given that it started with parallel orientation to the sidewall. Note the rapid loss of stability when the sperm pass the corner and lose the coordination with the sidewall.

The distribution of deflection angles α strongly depends on the beat-plane orientation of the sperm cell before it has reached the corner (Fig. 3.8). The distribution separates in two almost normal-like distributions. The parallel beat-plane orientation results in small deflections $\langle\alpha_{\|}\rangle \approx 10 \pm 5°$, whereas the perpendicular beat-plane orientation results in large deflections $\langle\alpha_{\perp}\rangle \approx 26 \pm 7°$. Furthermore, when the sperm cell detaches from the sidewall with a previously parallel orientation of its beat plane to the sidewall, it immediately reorients its beat plane parallel to the top (or bottom) walls(Fig. 3.9). This remarkable stability of the beat-plane orientation justifies the classification of the beat-orientation by its orientation with respect to either the sidewall (parallel) or the top/bottom wall (perpendicular).

3.1.4 Simple Steric Swimmer

The close proximity of the sperm cell with the sidewall suggests an important role of steric interactions. Thus, the contribution of steric interaction to the deflection of sperm around rectangular corners is investigated. This leads to the development of the cone-like swimmer model, which allows to interpret the relationship between the deflection angle of sperm, its inclination with respect to the sidewall and the beat-shape opening angles.

The orientation of the main elongation axis **e** of sperm is inclined towards the sidewall of the channel (Fig. 3.10 **a, b**). This inclination of the propulsion vector of the sperm cell provides an explanation of the steric interaction of the sperm cell with the wall and the resulting deflection angle: An inclined propulsion force leads to a velocity component that pushes the sperm cell towards the sidewall of the channel. Once the sperm cell passes the edge of the corner, it is free to move in this direction and therefore turns its swimming direction around the corner.

A minimal model allows to capture these steric interactions with the sidewall without the need of hydrodynamic interactions. Asymmetric swimmers composed of two beads with different radii are attracted to surfaces by pure steric interactions and self propulsion along their central axis (Wysocki, Elgeti, and Gerhard Gompper, 2015). This model is extended to a cone-like swimmer which is propelled with a constant force along its central axis. The minimal model follows over-damped dynamics. It includes only steric interactions and no hydrodynamics. The cone-like swimmer is described by two parameters: the opening angle of the cone δ and the length of the cone L'. Cone-like swimmers that follow the average deflection dynamics of sperm are shown in black in Fig. 3.10 **a, b**.

The turning behavior of the sperm is surprisingly well captured by this simple model when the parameters of the simple model are optimized accordingly. Figure 3.10 **(c)** compares the deflection simulated by the steric model to the full hydrodynamic sperm simulations. The average deflection dynamics of sperm are well captured by the simple model. The cone-like swimmer describes the average deflection for both orientations well. When the beat plane is perpendicular oriented, an effective opening angle $\delta_{\perp} = 15°$ and a length of $L' = 14\ r_h$ result in a deflection that matches the deflection of the full hydrodynamic model. For a sperm with parallel orientation between the beat plane and the sidewall the beat-shape envelope does not interact sterically. Nevertheless, a cone-like swimmer with length $L^{'} = 16\ r_h$ and an opening angle $\delta_{||} = 7°$ captures the average deflection quite well. As already suggested

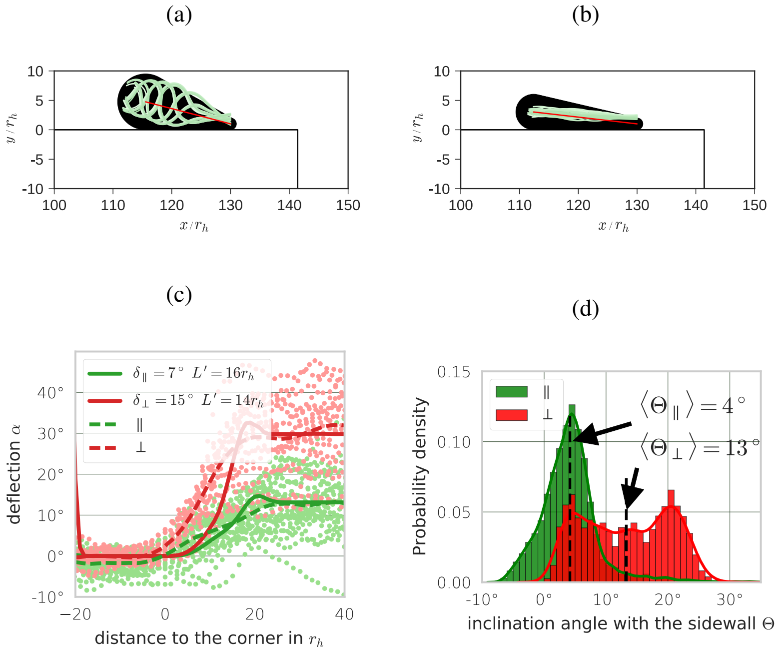

Figure 3.10 **Sperm cell orientation and steric model** - The beat pattern of the sperm cell swimming along the sidewall of the channel in **(a)** perpendicular and **(b)** parallel orientation (green) is overlaid by the corresponding cone-like swimmer (black) with its center line marked in red. **(c)** The deflection angle of a sperm cell simulated with full hydrodynamics and beat-shape dynamics is compared to the minimal self-propelled cone-like swimmer model. The color indicates the beat shape orientation during the time the sperm cell swims along the sidewall: parallel (green) and perpendicular (red). The dashed lines are the weighted spline fit to the ensemble with respect to the beat plane orientation. The solid lines show the deflection of the simple steric model. The distance to the corner is negative when the sperm cell approaches the corner and positive after the center of mass of its head has passed the edge of the corner. **(d)** Histogram of the inclination angle Θ between sperm symmetry axis $\mathbf{e}$ and the sidewall. For the perpendicular oriented swimmer, the cone-like swimmer opening angle of $\delta_{\perp} = 15^\circ$ agrees with the measured average inclination of the sperm orientation $\langle\Theta_{\perp}\rangle = 13^\circ$ (red). The inclination angle in the case of parallel orientation $\langle\Theta_{\parallel}\rangle = 4 \pm 5^\circ$ (green) differs from the cone-like swimmer opening angle $\delta_{\parallel} = 7^\circ$ due to additional hydrodynamic interactions.

by Elgeti, Kaupp, and Gerhard Gompper (2010), the effective opening angle can be interpreted as a result of hydrodynamic repulsion of the tail of the sperm cell.

Starting with the head passing the edge of the corner, the deflection angle increases approximately linear for one sperm length, sub-sequentially it plateaus in the total deflection angle (justifying the choice for alpha in the previous section and in the work of Kantsler, Dunkel, Polin, et al. (2013).) The sperm with perpendicular beat-plane orientation turns faster over a short length scale. In contrast the sperm with parallel beat-plane orientation turns slower over a longer length scale. Hence, the average deflection of sperm with perpendicular beat-plane orientation is 2.3 times larger than for sperm with parallel beat-plane orientation.

If the picture of dominant steric interaction holds true, this should be reflected in the distribution of the main elongation axis $\mathbf{e}$ of the sperm-cell inclination with respect to the sidewall in the hydrodynamic simulation. Indeed, sperm with parallel and perpendicular beat-plane orientation have a large difference in inclination (Fig. 3.10 d). For perpendicular beat-plane orientation, the inclination angle is almost equally distributed between $\Theta_\perp = 4^\circ$ to 24°, which can be understood by the beating of the sperm that constantly changes the orientation of the main axis and thereby interacts sterically with the sidewall. The regular beating of the flagellum creates a broad, almost uniform distribution. In contrast, the inclination of sperm with parallel beat-plane orientation is almost normal distributed around an average inclination of $\langle \Theta_{\|} \rangle = 4 \pm 5^\circ$. The inclination seems to be mainly affected by hydrodynamic interactions and the thermal noise. Both inclinations are in good agreement with the opening angle of the cone-like swimmer, as visualized in 3.10 (a, b). In case of perpendicular orientation the opening angle of the beat-shape envelope $\delta_b = 13^\circ \pm 2^\circ$ for an imposed wavelength of $\lambda = 0.63\,L$ (section 3.1.2) agrees with the average inclination measured here $\langle \Theta_\perp \rangle = 13^\circ$. Whether the origin of the slight inclination in the case of parallel beat plane orientation is due to hydrodynamic interactions or a result of a slightly nonplanar beat is unclear at the moment and needs further investigation.

The comparison of the minimal, steric simulations of a cone-like swimmer and the hydrodynamic sperm simulations proves that for a given inclination of the sperm cell propulsion axis **e**, the deflection of the sperm cell around a sharp corner is dominated by steric interactions. Even, for the parallel orientation where only a small inclination is observed an effective steric model captures the average deflection dynamics well. The larger deflection in the perpendicular orientation is therefore explained by the larger inclination, due to the larger in-plane opening angle of the beat-shape envelope.

3.1.5 Sperm Guidance and Selection in Narrow Channels

The dominant role of steric interactions and the wavelength dependence of the beat shape opening angles (section 3.1.2), suggests to extend the microchannel designs to more complex sidewall patterns. Here, two channels with different sidewall patterns are investigated.

The first channel consists of a zigzag channel with sharp corners of different angels γ. Dependent on the inclination angle Θ of the sperm cell, due to its beat plane orientation and opening angle, a critical corner angle $\gamma = \Theta$ exists, below which the sperm cells stay attached to the originating sidewall. The second channel has sidewalls with regions of alternating constant curvature. An increasing radius of curvature will increase surface attraction. This might allow to map differences in the beat-shape opening angles to changes in deflection angles. The modulation of the sidewall of a channel allows to guide and select sperm cells based on the shape of their beat pattern. Finally, the beat-plane orientation, when swimming in the proximity of a surface, provides an explanation for the altered surface attraction of curved surfaces compared to flat ones.

Variations of the corner angle γ provide a good test, whether steric interactions indeed dominate the deflection of sperm at corners. Since the beat-plane orientation still dominates the deflection-angle probability distributions (Fig. 3.11**a**), hydrodynamic interactions seem to play only a minor role here. Consistently, similar deflection angle distributions are observed for different corner angels γ; except for the geometric limitation $\alpha \leq \gamma$. For $\alpha = \gamma$ the sperm cell turns entirely around the corner and stays at the same sidewall. However, α can be slightly larger than γ, due to the finite distance between the sperm cell and the wall.

Using the result of the cone-like swimmer model (section 3.1.4), the average deflection angle of sperm can be estimated from the parallel $\Theta_{||}$ and perpendicular $\Theta_{\perp}$ inclination of the sperm cell. If the average deflection of the sperm cell is larger than the corner angle γ, the sperm cell stays at the same sidewall. For a sperm cell with parallel beat-plane the corner angle has to be below $\gamma = \delta_{||} = 7°$, whereas for perpendicular beat-plane orientation the corner angle has to be smaller than $\gamma = \delta_{\perp} = 15°$. Perpendicular oriented sperm cells can reach maximal deflection values of $\alpha = 20°$ and therefore swim around corners up to $\gamma = 20°$, whereas parallel oriented sperm cells always detach from corners with $\gamma \geq 20°$. Indeed, the crossing probability of sperm from one sidewall to the other (Fig. 3.11**b**) decreases from almost complete detachment for $\gamma \geq 60°$ to more than 80% attachment for $\gamma \leq 20°$, which agrees to deflection in the extreme cases $\gamma = 10°$ (attachment) and $\gamma = 60°$ (crossing), where the steric interactions dominate and either turn sperm completely around the corner or force them to swim straight until the originating sidewall is out of range. For $\gamma = 20°$ only perpendicular oriented sperm cells stay attached. For $\gamma = 10°$ both parallel and perpendicular oriented sperm cells manage to stay at the originating sidewall, as reflected in the very low crossing probability.

Even though the deflection angle distribution for $\gamma = 30°$ is almost identical to the distributions for larger corner angles, the crossing probability is at approximately 50 percent. In this intermediate regime around $\gamma = 30°$ a combination of hydrodynamics and steric interactions determines the crossing rate of sperm. The average deflection of perpendicular beating sperm of $\langle \alpha \rangle = 15°$ is just enough, so that they turn half around the corner and swim parallel to the main axis of the channel, whereas in the parallel case sperm are only slightly tilted away from the main axis towards the opposing sidewall. Therefore, sperm in both orientations detach from the originating sidewall and swim almost parallel along the main axis of the channel, giving them an equal chance of arriving at one of the two surfaces. In principle, a correctly tuned corner angle would allow to filter of sperm cells corresponding to their beat-plane orientation. However, the random nature of the two orientations as well as the overlap of the two distribution renders this approach difficult to realize.

The broad deflection angle distribution and the strong dependence on beat-plane orientation suggest to explore a novel channel design, where sperm

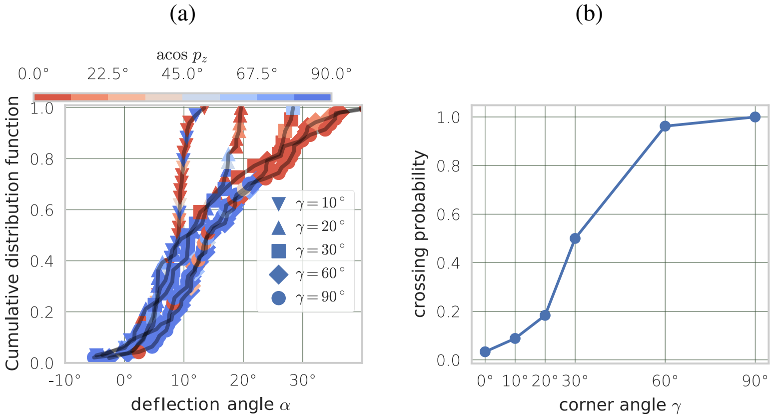

Figure 3.11 **Varying corner angle γ - (a)** The cumulative probability function of the deflection angle α does not change significantly with increasing corner angle γ - except for the cut-off at maximal deflection angles $\alpha = \gamma$. The average angle between the beat plane and the sidewall **acos**p_z is indicated by the blue ($\|$) to red ($\perp$) coloring. Note the perpendicular orientation to the sidewalls of the sperm cell for higher values of α. **(b)** The crossing probability to the opposing sidewall increases with increasing corner angle γ.

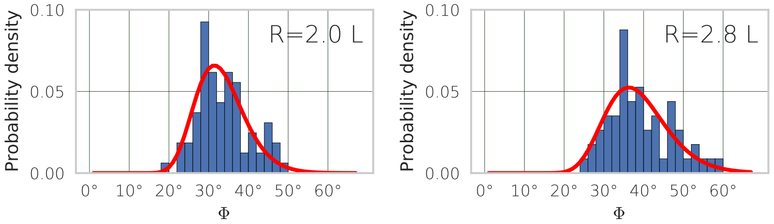

Figure 3.12 **Detachment point distributions** - Normalized probability distribution of the detachment point of the sperm cell in a channel with constant radius of curvature R. The distribution is well described by an inverse Gaussian fit (red) which is the solution of the first passage time distributions of a Wiener process with mean value p, shape parameter q and number of sperm passing N for $R = 2.0\ L$ $(p = 32.9,\ q = 2.5,\ N = 81)$ and for $R = 2.8\ L$ $(p = 36.7\ ,q = 2.8,\ N = 57)$.

swim along sidewalls with regions of alternating, constant curvature. The edge of the zigzag channel with 90° titled segments is smoothed by replacing it with quarter-circles of constant curvature. The probability of a sperm cell to stay attached to the sidewall can be controlled by changing the radius of curvature R. For a curved channel the critical radius of curvature is expected to be $R^c_{\|} = L'_{\|}/\delta_{\|} = 5.28\ L$ for the parallel orientation and a radius of curvature above $R^c_{\perp} = L'/\delta_{\perp} = 2.14\ L$ for the perpendicular orientation.

Because the deflection now happens along the entire surface until the sperm cell detaches, no unique deflection point can be defined anymore. Instead, the attachment strength is quantified by measuring the length of the path along the quarter-circle before detachment. The position of the sperm cell is described by the polar angle $\Phi(t)$. The region of constant curvature starts at $\Phi = 0°$. After the sperm cell swims into the region of constant curvature, it continues to swim along the curved sidewall until it orients away from the surface and eventually detaches. Since the reorientation happens in the vicinity of the surface, the detachment point Φ, where the center of mass of the head of the sperm cell is more than $8\ r_h$ away from the curved surface, is employed to measure the attraction of the sperm cell towards the surface.

Figure 3.12 shows the probability distributions of these detachment angles for a radius of curvature of $R = 2\ L$ and $R = 2.8\ L$. The mean detachment

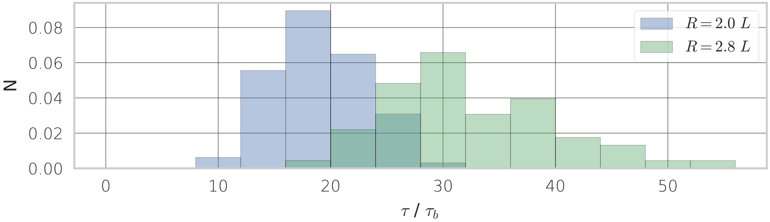

Figure 3.13 **Attachment time distributions** - The attachment time τ, measured in beat periods, gives the time sperm stay attached to the sidewall of the curved channel with radius R. The mean of the distribution is shifted from $\langle\tau\rangle = 20\ \tau_b$ for $R = 2.0\ L$ ($N = 81$) to $\langle\tau\rangle = 33\ \tau_b$ for $R = 2.8\ L$ ($N = 57$), which is almost proportional to the difference in radii.

angle $\langle\Phi\rangle$ increases slightly from about $\langle\Phi\rangle = 33^\circ$ to $\langle\Phi\rangle = 38^\circ$. However, no sperm cell swims around the curved region entirely, even though the steric argument predicts possible attachment for $R = 2.8\ L$ The reason for this is the destabilization of the perpendicular beat-plane orientation by the curvature of the sidewall, which will be discussed at the end of this section. Even constant deflection angles correspond to longer attachment times, during which the sperm cell stays attached to the sidewall. This is because the length of the swimming path which is needed to reach a certain polar angle increases with the radius of curvature R, whereas the propulsion velocity remains unchanged. Indeed, the mean attachment time τ increases by a factor of 1.67 (Fig. 3.13).

Spagnolie, Moreno-Flores, et al. (2015) suggested to model the very similar problem of a hydrodynamic dipole swimmer trapped by a cylinder as a Wiener process with drift. Indeed, the detachment angle distribution is well described by an inverse Gaussian, $f(\Phi) = q/(2\pi\Phi^3)\exp\{-q(\Phi-n)^2/(2p^2\Phi)\}$, which is the solution of the first passage time of a Wiener process with drift. It describes the distribution to a reasonable agreement for both radii of curvature.

If surface attraction is sterically dominated, it should increase with wavelength, due to the increasing beat-plane opening angle. However, sperm swimming in the curved channel with $R = 2.8\ L$ do not exhibit major changes in surface attraction. Only a small influence on the detachment point distribution is

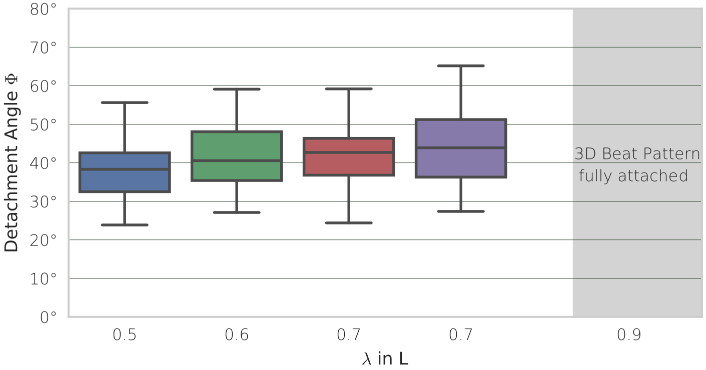

Figure 3.14 **Detachment point distributions** - Bar plot of the detachment polar angle Φ at which the sperm cell detaches from the curved surface for beat patterns with different wavelength λ. The mean of the distributions slightly increases with increasing wavelength. ($N = 26 - 100$). For $\lambda = 0.9\ L$ the beat shows a 3D-component which leads to perfect attachment.

observed for $\lambda \leq 0.7\ L$ (Fig. 3.14). Surprisingly, the behavior changes abruptly to a perfect attachment at a critical wavelength of $\lambda = 0.9\ L$. The explanation for this sudden transition lies within the three-dimensional beat pattern of the sperm cell (section 3.1.2).

In order to complete the argument of steric interaction leading to the large surface attraction for 3D beating sperm cells, the stability of the beat-plane orientation while swimming in the corner between sidewall and top/bottom wall of the channel is analyzed for the curved ($R = 2.8\ L$) channel. The phase-space flow (Fig. 3.16) compares the beat-plane orientations of the 2D and 3D cases while swimming along the quarter-circle. A consistent picture of attachment and detachment dynamics emerges. For planar beating, the sperm cells remain at the surface while perpendicular oriented, and detach while rotating to parallel orientation. Instead of a bi-modal distribution at parallel and perpendicular orientation as for the planer beating pattern (2D), the orientation of the 3D beat pattern is almost uniformly distributed (Fig. 3.15).

The distance to the sidewall of the channel and the polar Φ describe the passage of the sperm cell along the curved region. The quarter-circle ranges

(a) (b)

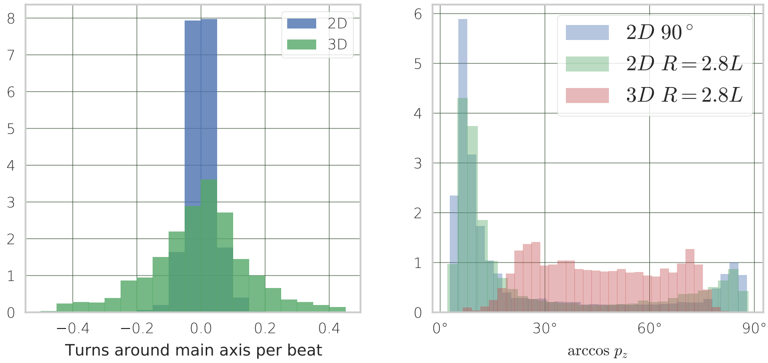

Figure 3.15 **2D vs 3D beat plane orientation** - **(a)** The three-dimensional beat pattern (3D) turns the sperm cell half way around its main axis **e**, whereas the planer beat pattern (2D) does almost not turn (Eq. 3.2). The 3D beat plane wobbles maximal half a turn, and thereby is switching between parallel and perpendicular orientation to the sidewall. **(b)** A histogram of the beat-plane orientation with respect to the sidewall arccos p_z for the planar beating sperm cell swimming along the $\gamma = 90°$ ($2D$ $90°$) and the curved channel ($2D$ $R = 2.8$ L) are compared to a sperm cell with out-of-plane beating along a curved channel ($3D$ $R = 2.8$ L). The 2D beat pattern shows a bi-modal distribution for parallel and perpendicular orientation, whereas the wobbling motion of the 3D beat pattern leads to an almost uniform distribution.

from $\Phi = 0^\circ$ to $\Phi = 90^\circ$ with the zenith of the corner at $\Phi = 45^\circ$. Sperm attach to the sidewall at $\Phi \approx -22^\circ$. For the zigzag channel with a corner of $\gamma = 90^\circ$, the beat plane attains a stable orientation when the sperm cell aligns along one of the walls. During $0^\circ < \Phi < 45^\circ$ the beat plane is either parallel or perpendicularly aligned. No transitions between the two states happen until the sperm cell approaches the sharp edge of the corner at $\Phi = 45^\circ$. Once the head passes the corner, the sperm cell departs from the sidewall, which renders the parallel orientation unstable and the sperm cell reorients towards the top/bottom wall of the channel.

The planar beating pattern in a curved channel starts with a similar bi-modal distribution of beat-plane orientations as for the sharp corner. However, the curvature of the sidewall, starting from $\Phi = 0^\circ$ destabilizes the parallel beat-plane orientation with the sidewall. When the sperm rotates to a perpendicular aligned beat plane $\arccos p_z = 0^\circ$, the sperm starts to detach from the sidewall, leading to a detachment of all sperm cells before the zenith at $\Phi = 45^\circ$. Interestingly, the length the sperm cell swims in parallel orientation seems to be almost constant.

Sperm with a perpendicular beat-plane orientation from the beginning almost manage to swim around the corner until $\Phi = 45^\circ$, but loose their stable beat-plane orientation at the zenith and detach as well.

Finally, for the almost completely attached three-dimensional beat pattern, the beat-plane orientation keeps wobbling between $15^\circ < \arccos p_z < 75^\circ$ (Fig. 3.15). Since the beat-plane rotates much faster than the movement of the sperm cell along the channel, the average change of the beat-plane orientation is almost zero. No stable beat-plane orientation emerges. A similar argument explains the almost unchanged distribution for increasing wavelength. Even though the increasing nonplanarity of the beat pattern increases the surface attachment of the perpendicular orientated sperm cell, the detachment is already dominated by the rotation of the destabilized perpendicular orientation around the zenith of the curved region. Therefore, only a slight increase of the mean deflection point occurs.

Considering the strong attraction of three-dimensional beating sperm cells, the recently proposed design of teardrop-shaped posts by Davies Wykes et al. (2017) seems to be particularly promising. The teardrops have a large

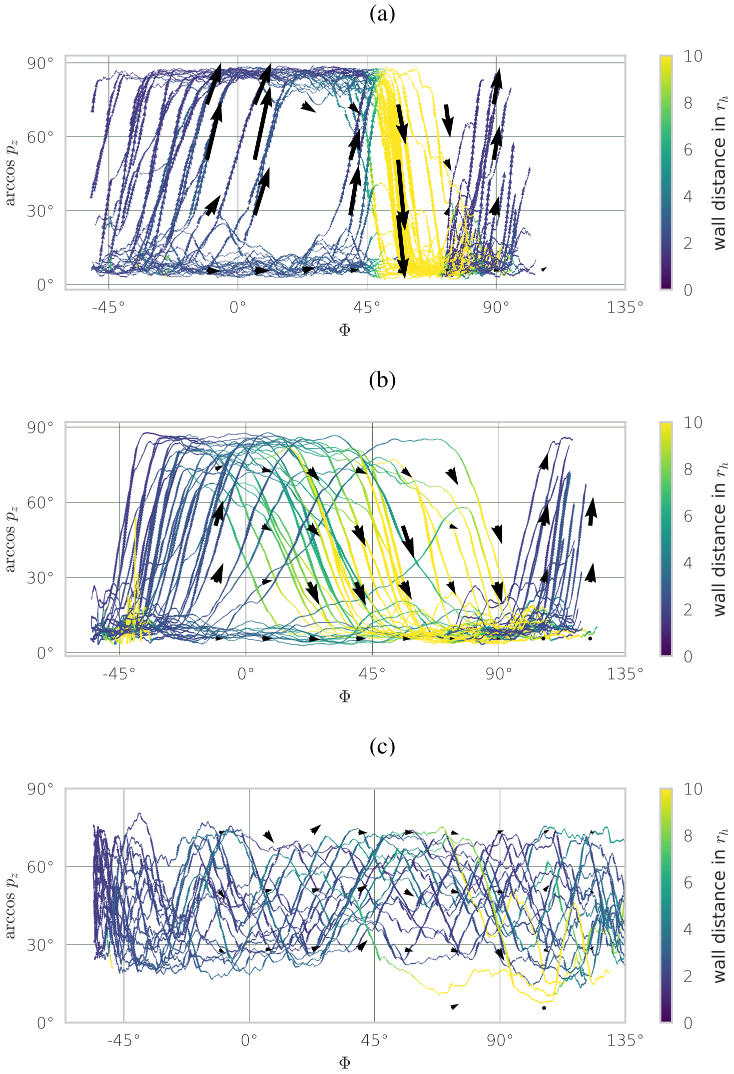

Figure 3.16 **Phase-space flow of the beat plane orientation** - The phase-space flow of the polar angle along the corner Φ and the beat plane orientation with the sidewall $\arccos p_z$ is compared for **(a)** 2D beat pattern in a zigzag channel with $\gamma = 90°$, **(b)** 2D beat pattern in a curved channel ($R = 2.8\ L$) **(c)** 3D beat pattern in a curved channel ($R = 2.8\ L$). The color indicates the distance to the closest sidewall. Note that at $\Phi = 0°$ the curved region begins and $\Phi = 45°$ corresponds to the edge of the $\gamma = 90°$ corner **(a)** or to the the zenith of the quarter circle **(b, c)**. The black arrows highlight the average flux in a grid of $18° \times 12°$.

radius of curvature at the bottom and a small radius of curvature at the top, and thereby allow for alignment of swimmers along the low curvature area and detachment when approaching the high curvature area. When tuned accordingly, only sperm with large wavelength that show a three-dimensional beat pattern align along the direction of the teardrop, whereas sperm cells with smaller wavelength which beat planar are not.

3.1.6 Conclusions - Details Matter

The results of the fluid dynamics simulation indicate that the shape of the beat pattern plays an important role for sperm surface interactions. Generic swimmer models are limited in explanatory power to understand the highly complex dynamics. Simulation results show a strong dependence on boundary guidance and the beat-shape opening angles. Steric interaction could potentially be a major factor in the function of the highly selective process of sperm cell migration in vivo.

Nonplanar beat patterns of sperm created by planar imposed torques have been shown. Sperm show a transition from planar to three-dimensional beat patterns that depends on the imposed wavelength. The switching between an extended three-dimensional beat pattern and a planar one influences the opening angle of the beat-shape envelope and so the surface attraction. Indeed, several experimental reports on switching between planar and three-dimensional beating exist (Nosrati, Driouchi, et al., 2015; Su, Xue, and Ozcan, 2012).

Sperm swimming in narrow channels tend to swim in the corners (Nosrati, Graham, et al., 2016). When they are in the vicinity of two planar surfaces, their planar beat can stably orient along either of them. This bi-stable configuration gives rise to a deflection angle distribution around rectangular sharp corners which depends on the beat-plane orientation. The average deflection angle for parallel and perpendicular beat plane orientations is explained by steric interactions of a cone-like swimmer with the sidewall.

The detachment point distribution is found to just slightly increase with radius of curvature of the channel. However, the effect is much less dependent on the wavelength than expected, since the sidewall curvature destabilizes the beat-plane orientation of the sperm cell with respect to the sidewall. Above a critical wavelength of $\lambda = 0.79\,L$ a buckling instability occurs which renders the beat pattern three-dimensional. The out-of-plane beat component induces a rotation of the sperm cell and enhances the surface attraction so that the sperm cell swims entirely around a curved quarter-circle.

These simulation results pose some interesting questions of how surface interactions guide active swimmers, in particular sperm, through complex and highly confined geometries. It emphasizes the importance of resolving a three-dimensional shape of the beating pattern which determines steric interactions with the surface.

3.2 3D-Beat Pattern of Sperm Cell

3.2.1 Introduction

Sperm cells propel themselves by the periodic beat of their flagellum. Even though sperm of most species share a common flagellar structure, their beat pattern and swimming paths vary a lot, because they had to adapt during evolution to their specific environment. The detailed description of the complex beat pattern of the flagellum can lay the basis for understanding the structural origin and evolutionary advantage of changes in beat shape. Small changes in wavelength, beating amplitude or frequency have the potential to change the resulting beat shape dramatically.

In the first part, section 3.2.2, the three-dimensional beat pattern of freely swimming human sperm cells is analyzed, based on holographic imaging data obtained by experimental collaborators at Forschungszentrum Caesar (Bonn). The three-dimensional beat pattern is quantified with regard to its nonplanarity and projected onto a local, co-moving and co-rotating reference system.

In section 3.2.3, the beat shape is qualitatively compared to simulation data of sperm with varying elastic properties of the filament. For high twist rigidity, the filament beats planar, whereas for low twist rigidity, it beats in a three-dimensional beat pattern. The out-of-plane beating component emerges from a twist of the filament which leads to a rolling of the sperm cell around its central axis.

3.2.2 Analysis of Experimental Data

The three-dimensional space curve of the flagellum was reconstructed from 3D digital holographic microscopy (Gabor et al., 1948; Lee and Grier, 2007) recordings of freely swimming human sperm cells. A high-speed camera obtains holograms with a spatial resolution of $0.17\mu m/px$. Rayleigh-Sommerfeld back-propagation is used to compute the z-position under the assumption that the flagellum of the sperm cell is a weakly scattering object. First, head tracking separates the center of mass of the sperm from the relative motion of the flagellum, providing a reference to align frames. Starting from the head,

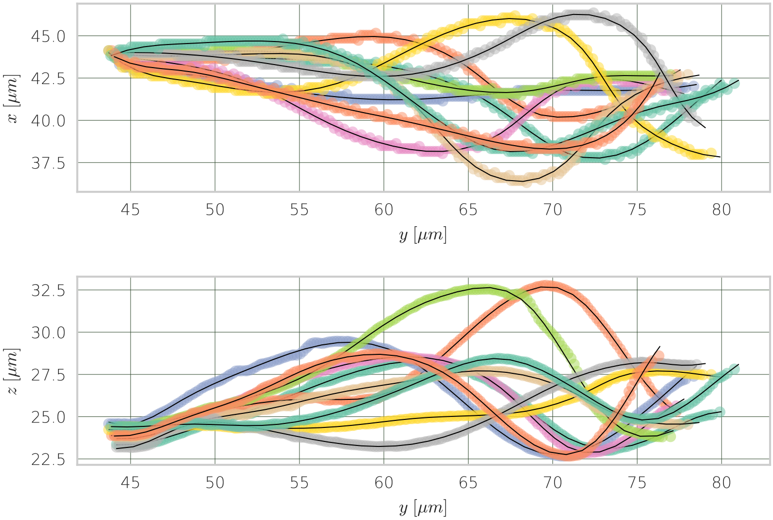

Figure 3.17 **Beat pattern of a human sperm cell** - Snapshots of the flagellum taken at 10 random time frames, showing raw experimental data (colored dots) in the lab-reference frame, overlayed by the fitted splines (black lines).

three-dimensional small volumes, voxels, along the flagellum are detected and reconstructed. Following this scheme, a voxel cloud along the shape of the flagellum is constructed.

The high spatial and temporal resolution of this voxel cloud allows a precise reconstruction of the flagellar shape $\mathbf{r}(s,t)$. First, a 3D-spline is fitted to the voxel data, where each voxel is weighted by the standard deviation of the voxels in a window of 10 voxels around it. The usage of local weights smooths out local errors in the reconstruction, due to systematic shifts introduced by dust or other particles disturbing the optical path and provides a reasonable smooth fit as shown in Fig. 3.17.

Because the reconstruction cannot resolve the orientation of the material frame along the spline, an out-of-plane component due to twist cannot be distinguished from an out-of-plane bending (section 2.4.4). However, the rotation of the entire sperm can be approximately separated from the relative

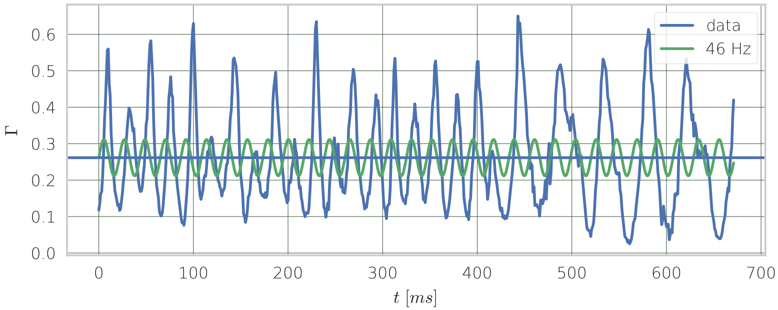

Figure 3.18 **Nonplanarity of the beat** - The nonplanarity Γ (blue) of the beat is described by the ratio of the two minor-axis principal moments of the gyration tensor $\Gamma = \lambda_p/\lambda_b$. It oscillates with a frequency of 48 Hz around the mean value $\langle\Gamma\rangle = 0.26$.

motion of the flagellum using gyration-tensor based decomposition ((Eq. A.1)). The local reference frame $\mathbf{e}(t)$, $\mathbf{b}(t)$, $\mathbf{p}(t)$ and center-of-mass motion decouples the orientation of the entire body from the relative beat pattern of the flagellum which is described by the amplitude $B(s,t)$ of the in-plane beating and the amplitude $P(s,t)$ of the out-of-plane beating.

The nonplanarity of the flagellum (Fig. 3.18) measures the amplitude of the out-of-plane beating, which is defined by the gyration-tensor analysis. It is given by the ratio $\Gamma(t) = \lambda_p(t)/\lambda_b(t)$ of the principal moments of the gyration tensor. The mean value $\langle\Gamma\rangle = 0.26$ indicates an almost planar beat. The mean value Γ adopts about the same value as reported by Bukatin et al. (2015) $\langle\Gamma\rangle \approx 0.2$. Therefore, 70% of the average beating is within a well-defined beat plane, which allows to decouple the planar beat from the out-of-plane beating along $\mathbf{p}(t)$. The relatively high planarity of the beat justifies the definition of the local coordinate system using the gyration tensor. In particular, a Fourier transformation in time of the in-plane beating $B(s,t)$ gives the power spectrum of the beat frequency $\tilde{B}(\omega,t)$ (Fig. 3.19). A pronounced and narrow maximum at a beating frequency of $f_{beat} = 22 \pm 2\ Hz$ agrees well with previously reported values (Ooi et al., 2014). The beating amplitude increases towards the middle of the flagellum ($s = 0.5\ L$) and decreases again

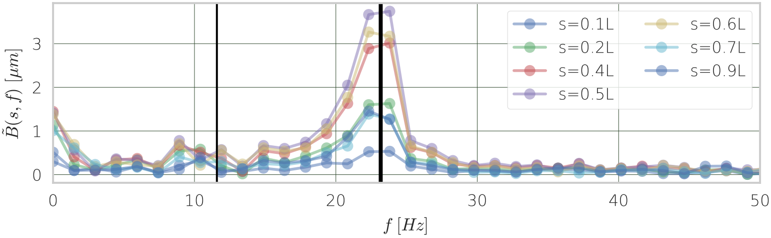

Figure 3.19 **Power spectrum of in-plane beat frequencies in dependence on the arc length** - Power spectrum of the in-plane oscillations $\tilde{B}(s,f)$ of the beat at different arc-length positions s. Human sperm cells beats with a frequency of $f_{beat} = 22\ Hz$ (thick black line). A second much smaller peak at lower frequency of $f_{beat}/2$ is also observed (thin black line).

towards the end. A much smaller, wider peak is observed at around half the beating frequency ($f_{beat}/2 = 11\ Hz$). The beat frequency allows to define the beating time $\tau_b = 1/f_{beat}$ which provides the natural time scale for further analysis of the three-dimensional beat.

The angular rolling velocity $I_e(t)$ around the main axis $\mathbf{e}$ is quantified by projecting the angular velocity of the beat-plane normal $\mathbf{p}(t)$ on the main axis $\mathbf{e}(t)$:

$$I_e(t) = \left(\mathbf{p} \times \frac{d}{dt}\mathbf{p}\right) \cdot \mathbf{e}. \tag{3.2}$$

A negative (positive) angular rolling velocity corresponds to clockwise (counterclockwise) rotation around $\mathbf{e}(t)$, viewed from the tail towards the head. The angular velocity of the rolling fluctuates around the average value of $\langle I_e \rangle = -55\ s^{-1} = -2.52\ \tau_b^{-1}$; it stays negative for the entire observation time, showing that no change in the rotation direction occurs. The average frequency of the rolling is $f_{roll} = I_e/2\pi = 8.75\ Hz = -0.40\ \tau_b^{-1}$ with counterclockwise rotation. Figure 3.20 shows the rolling of the flagellum during a peak in angular rolling velocity. A kink in the mid-piece seems to trigger a twist wave which travels through the tail. Thereby, it quickly changes the beat-plane orientation by almost 90°.

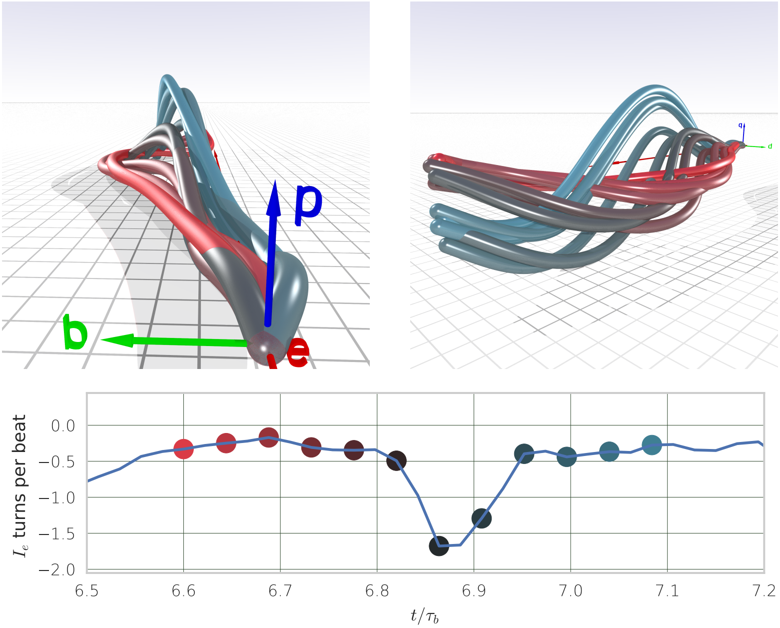

Figure 3.20 **Flagellar beat shape in the local frame** - The flagellar beat shape is visualized by splines (upper part) that are colored from red towards blue with evolving time. At the beginning, the almost planar beat (red) is oriented parallel to the b-axis and rotates over time by almost 90° (blue). The local coordinate system is fixed in the starting orientation (red) and does here not rotate with the sperm. It is placed at the head position. Lower part shows the angular rolling velocity of the beat plane around the main axis (red) of the sperm, measured in turns per beat. The colors of the points match the color of the spheres describing the beat shape.

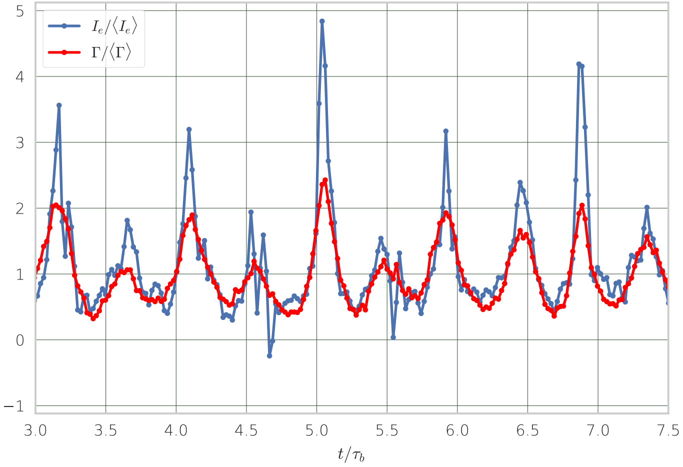

Figure 3.21 **Rolling speed and nonplanarity** - Changes in the rolling angular velocity $I_e(t)$ (blue) and in nonplanarity Γ (red) correlate with Pearson correlation coefficient of 0.8

Figure 3.21 shows the fluctuation of the nonplanarity and its correlation with the angular rolling velocity with time. They correlate with Pearson correlation coefficient of 0.8. The nonplanarity peaks at $\Gamma = 0.52$ indicate a substantial out-of-plane component in the beat pattern.

This indicates that rolling is driven by the out-of-plane component of the beat pattern. The nonplanarity and the rolling show peaks at a frequency of $46\ Hz \approx 2 f_{beat}$, which is about twice the beat frequency.

The regular peaks of the nonplanarity indicate a localized twist of the beat plane which travels along the flagellum. Indeed, different parts of the flagellum lie well within two planes (Fig. 3.22). Again, the gyration tensor is used to quantify the planes and find the twist point $s_t(t)$ along the arc length where the flagellum changes the orientation of its beat plane. Γ_1 represents the nonplanarity calculated by the gyration tensor up to the arc-length twist position $s_t(t)$, whereas Γ_2 represents the nonplanarity from the arc-length twist position

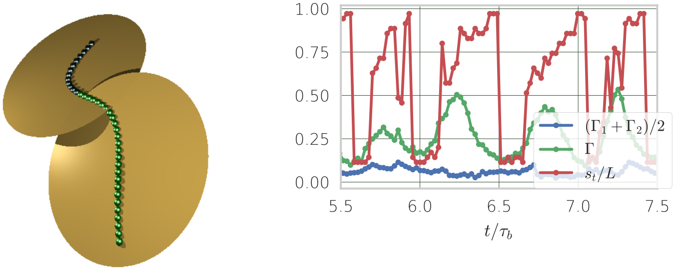

Figure 3.22 **Beat-plane nonplanarity in experimental data** - On the left the two beat planes separated by the twist point for $t = 6.5\ \tau_b$ are visualized. On the right the time series of the nonplanarity values Γ_1, Γ_2 for the part of the sperm cell lying within the corresponding planes are compared to the overall nonplanarity Γ. The combination of $(\Gamma_1 + \Gamma_2)/2$ reduces the large nonplanarity peaks significantly, while the twist point s_t moves towards the tail of the flagellum.

till the end of the tail. The twist point s_t is found by minimizing the sum $(\Gamma_1 + \Gamma_2)/2$ of both nonplanarities. If the out-of-beat component of the beat shape were equally distributed along the flagellum, the split would not reduce the nonplanarity value. In contrast, Fig. 3.22 shows a drastic reduction for the combined nonplanarity $(\Gamma_1 + \Gamma_2)/2$, especially for the peaks of the overall nonplanarity Γ. This suggest the following interpretation: the nonplanarity peaks are the result of a localized twist at $s_t(t)$, which moves along the tail. When the twist point s_t reaches the end of the flagellum, the beat becomes planar again until the flagellum starts to twist again at about $s = L/2$.

A kymograph of the curvature $\kappa(s,t)$ along the flagellum is shown in Fig. 3.23. The twist point occurs preferentially in regions of low curvature. A direct quantification of the twist wave is difficult, because noise heavily affects the twist measurement for low curvature regions and the twist is undefined along the space curve for zero curvature. However, the twist point and the very localized extremum of the twist seem to coincide.

Here, experiments from only a single sperm cell have been analyzed. Further studies using a larger number of samples should address the question whether the chirality occurs due to a spontaneously broken symmetry ("buckling in-

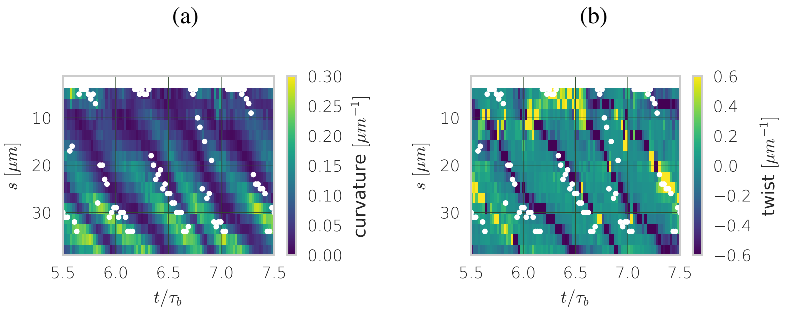

Figure 3.23 **Curvature and twist kymographs of the flagellum** - **(a)** The traveling curvature wave along the flagellum is clearly seen by the two peaks in the unsigned curvature plot, towards the tail of the flagellum. White dots mark the position of twist point along the flagellum s_t which seems to coincide with areas of minimal curvature and a twist wave **(b)**. Note that the error of the twist measurement increases when curvature is small.

stability"). Previous experiments (Ishijima, Hamaguchi, et al., 1992) where an almost equal number of clockwise and counter-clockwise rotations were reported, hint to a dynamic buckling instability induced by hydrodynamic interactions. Hydrodynamic simulations in the following section support this view and provide more insight by obtaining the twist and bending energies directly.

Because the beat period is well resolved in time, the gyration tensor provides an appropriate measure to indirectly establish the normal vector orientation along the flagellum. This opens the door for further analysis of the beat pattern and its different mechanisms of its deformations.

3.2.3 Simulations

In this sub-chapter MPC simulations (section 2.3.3) are employed to find an explanation for the out-of-plane beating component. The key idea is to look for a transition, where the planar beat becomes unstable and where the combination of flagellar dynamics with hydrodynamic interactions leads to an out-of-plane component of the beat. Initially, bending and twist rigidity of the flagellum are varied to roughly localize the transition to three-dimensional beating. This initial analysis is followed by a detailed investigation of three-dimensional beat patterns for two different beating frequencies.

The flagellum is described by a Kirchhoff model (section 2.4.4), consisting of 50 beads along its center line, which are connected with a bond-length $l_b = 1\mu m$ in agreement with the length of the flagellum $L \approx 50\mu m$. The cross section of the flagellum is assumed to be isotropic with regard to the bending rigidities: $K_1 = K_2 = K$ along the two axes. The twist rigidity K_3 is varied over several orders of magnitude to search for a twist instability. Planar bends are imposed as a traveling wave along the flagellum with a curvature amplitude of $\kappa = 0.1\ l_b$, a constant frequency $\omega = 0.05\ \sqrt{k_BT/(am^2)}$ and a wavelength of $\lambda = 1.26\ L$. The correspondence between simulation units and the respective experimental scales for time and rigidity is not straightforward. Therefore, it is discussed at the end of this section when interpreting the results.

To analyze the beat pattern and to compare its in-plane component $B(s,t)$ and out-of-plane component $P(s,t)$, the flagellum is projected along the gyration-tensor axes (see the fitting of the experimental sperm data in section3.2.2). Indeed, three-dimensional beat patterns emerge for low twist rigidity. A flagellum with large twist rigidity $K_3 = 2 \cdot 10^4\ k_bTa$ beats almost planar, whereas a flagellum with low twist rigidity $K_3 = 2 \cdot 10^3\ k_bTa$ beats in a complex three-dimensional shape (Fig. 3.24).

The in-plane component $B(s,t)$ shows almost the same maximal amplitude of $4\ r_h$ as the planar beat. However, the out-of-plane component of the three-dimensional beat pattern follows a clockwise spiral (viewed from the tail) and compared to the in-plane amplitude of $6\ r_h$ has a relatively small amplitude of $1.5\ r_h$. By following the spiral starting from the head (located at $(0,0)$) non-uniform bending is observed: the straight midpiece is followed by a sharp bending, then by a straight part, and finally a second sharp bending in the last third of the tail. Even though only planar bends are imposed along the flagellum, a complex three-dimensional pattern emerges due to the load, which the hydrodynamic friction creates along the flagellum.

In order to quantify this transition further and find the range of material parameters in which three-dimensional beating occurs, a phase-space scan was performed. The phase space in Fig. 3.25 measures the nonplanarity for various twist and bending rigidities. The peaks in the nonplanarity, quantified

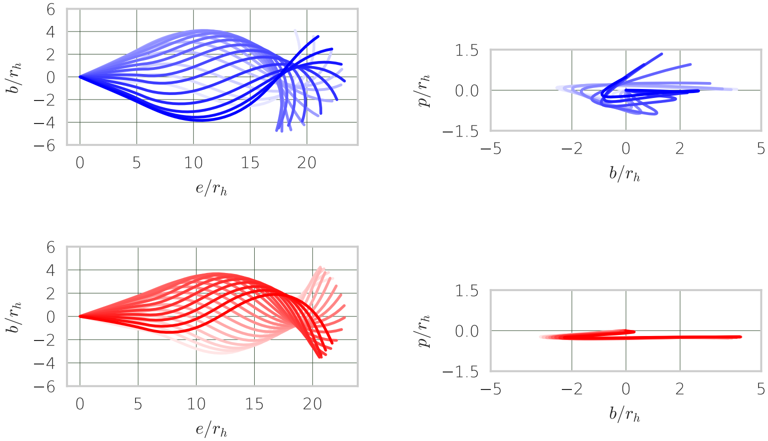

Figure 3.24 **Planar vs. nonplanar beat pattern** - The flagellum of a beating sperm cell simulation with small twist rigidity $K_3 = 2 \cdot 10^3\ k_bTa$ (blue) that exhibits out-of-plane beating (right column) is compared to the planar beat shape for a flagellum of large twist rigidity $K_3 = 2 \cdot 10^4\ k_bTa$ (red). The in-plane beat pattern (left column) does not change significantly.

by the 95%-percentile, are used to characterize the transition between planar and nonplanar beating. For high twist rigidities, the imposed planar bends lead to an almost perfectly planar beat with very small nonplanarity values Γ. However, when the twist rigidity is low $K_3 \leq 10^3\ k_bTa$, the in-plane bends give rise to a three-dimensional beat. The transition is sharp and independent of the bending rigidity K.

The bending can either be the result of an out-of-plane bending or twisting of the flagellum. In the simulation, the three-dimensional beat can be analyzed further by measuring the energies of the deformation of the flagellum for each axis. The energy of active beating is reflected by the in-plane bending energy E_{K_1}. The out-of-plane beat must either contribute to the twist energy E_{K_3} or the out-of-plane bending energy E_{K_2}. The bending energies for a passive flagellum fluctuate around the thermal equilibrium value for each degree of freedom: $0.5\ k_bT$. Energies originating from the active beat pattern need to lie significantly above this value.

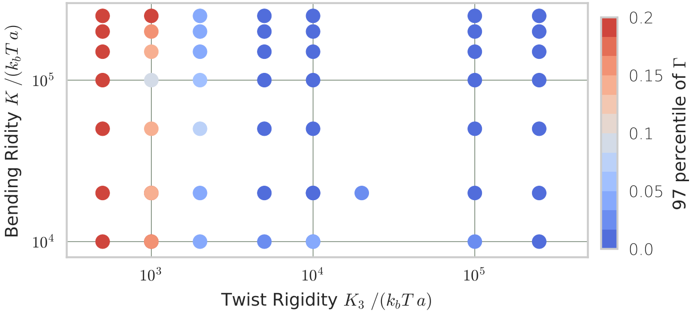

Figure 3.25 **Twist/bending rigidity phase space** - The color in the phase space measures the 95 percentile of the nonplanarity Γ of the beat pattern as defined by the principal moments of the gyration-tensor. Bending rigidity K changes along the y-axis, whereas twist rigidity K_3 varies along the x-axis. At a critical twist rigidity of $K_3 \leq 10^3\ k_bTa$ and below peaks of nonplanar beating develop.

Two simulations are performed using rigidities in the 3D-beat regime $K = 2500 \cdot 10^3\ k_bTa$ and $K_3 = 10^3\ k_bTa$. They only differ in beat frequencies $\omega = 0.1\sqrt{ma^2/k_bT}$ and $\omega = 0.05\sqrt{ma^2/k_bT}$. The change in beat frequencies imposes different viscous loads along the flagellum. A higher beat frequency increases the friction forces acting on the flagellum which might increase the out-of-plane beating.

As shown in Fig. 3.26, in both cases the planar bending energy E_{K_1} is transferred only to the twist mode energy E_{K_3} whereas the out-of-plane bending energy E_{K_2} stays constant and only fluctuates in the range of the thermal noise. This result proves the existence of a twist mode in the flagellum that is induced by an elastic instability. The maximal amplitude of the twist energy is 40 k_bT for the low-frequency beating with $\omega = 0.05\ \sqrt{ma^2/k_bT}$, and about six times larger at 260 k_bT for $\omega = 0.1\ \sqrt{ma^2/k_bT}$.

Even though the dissipative forces acting on the flagellum are proportional to the beat frequency ω, the energy of the twist mode scales non-linearly. In agreement with experimental data, maximal twist occurs for minima of the bending energy. The curvature profile stays unchanged. As reflected in the higher energies, the beat pattern is more stable for higher beating frequencies. In particular, two stable peaks of nonplanarity occur as found in the experimental data for human sperm cells.

3.2.4 Conclusions

The hydrodynamic simulations show remarkable qualitative similarities to the beat pattern of human sperm. Notably, the nonplanarity of the beat fluctuates abruptly which is not expected for a beat pattern with constant twist. To compare simulation and experimental values of bending and twist rigidities, scales must be related to each other. The length scale of the flagellum provides a straightforward reference, resulting in a bond length $l_b = 1\ \mu m$. However, finding the appropriate energy and time scales to match the bending, twist rigidities and the viscous forces is not so straightforward. The characteristic time scale is determined by comparing the Reynolds numbers, where the velocity is chosen as the in-plane beat amplitude times the beat frequency $B\omega/(2\pi)$ and the diameter of the sperm as a characteristic length scale. In the simulations the kinematic viscosity ν (Eq. 2.38) and the amplitude of the out-of-plane beat $B \approx 4\ r_h$ gives a Reynolds number $fBl_b/\nu = 0.04 - 0.08$ which ensures the low Reynolds number regime. Nevertheless, it is much larger than the experimental Reynolds number $Re \approx 10^{-5}$ of sperm, which is determined using a flagella diameter of $\approx 5\ \mu m$, a beat frequency of 22 Hz and a kinematic viscosity of water $\nu \approx 10^{-6}\ m^2/s$. Therefore, the simulations either underestimate the viscous load or simulate sperm with higher beat frequencies. A slower beating sperm will decrease the viscous load, whereas a sperm beat at higher viscosity will increase the viscous load. It is therefore difficult to predict how a change in Reynolds number will change the twist instability. Since the mechanical properties of the flagellum model are unaffected by the hydrodynamics and the simulation still ensures low Reynolds hydrodynamics, it is likely that the qualitative description still holds. Thus, only the value at which the twist instability occurs might change.

The range of $K = 10^4 - 10^6\ k_bTa$ corresponding to $10^{-23} - 10^{-21}\ Nm^2$ agrees well with measured bending rigidity of $6 \cdot 10^{-21} Nm^2$ (non-beating flagellum) to $4 \cdot 10^{-22} Nm^2$ (beating flagellum) (Ishijima and Hiramoto, 1994). Even though the viscous load and time scales do not match the experimental situ-

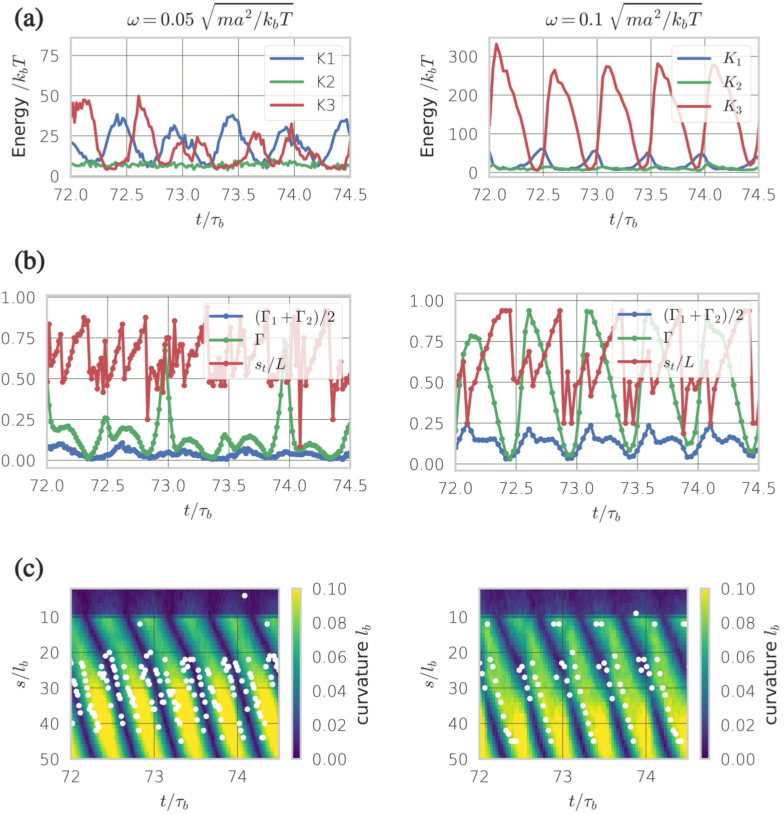

Figure 3.26 **Simulation of nonplanar beating sperm** - The beat pattern of a sperm cell in the right column ($\omega = 0.1\sqrt{ma^2/k_bT}$) is compared to a half as fast beating one ($\omega = 0.05\sqrt{ma^2/k_bT}$) in the left column. **(a)** The energy of the out-of-plane component goes into the twist degree of freedom E_{K_3}, whereas the out-of-plane bending energy E_{K_2} only fluctuates around the thermal equilibrium value. The twist energy increases non-linear for the larger beat frequency. **(a)** The nonplanarity peaks Γ increase with the beating frequency. For the low beating frequency only one peak per beat is found, whereas $\omega = 0.1\sqrt{ma^2/k_bT}$ shows two regular peaks per beat. The nonplanarity of the flagellum is reduced when split into two segments at the twist point s_t. Γ_1 and Γ_2 are the nonplanarity values for the corresponding planes. **(c)** The twist point s_t (white points) moves along the flagellum close to the minimum of the curvature wave. The curvature wave is not changing with increased beating frequency.

ation quantitatively, the two orders of magnitude between bending and twist rigidity at which the twist instability occurs are supported by experiments. Atomic-force microscopy measurements (Kis et al., 2002) have determined the mechanical anisotropy of microtubules. The shear modulus G is found to be two orders of magnitude lower than the Young's module E. Considering a homogeneous cylinder, the mechanical anisotropy leads to an anisotropy in bending $K_1 = K_2 = E\ \pi R^4/4$, and twist rigidity $K_3 = G\ \pi R^4/2$. This indicates that indeed, buckling induced out-of-plane beating is possible in flagella due to the two orders-of-magnitude difference in Young's and shear module.

Clearly, a more detailed observation of beat patterns under different viscosity is needed to fully elucidate the mechanism. The presented simulations reproduce key features observed in the experiment. The nonplanarity Γ of the beat pattern shows regular peaks of different amplitude, and dividing the flagella into two parts at the twist point s_t lowers the nonplanarity to almost zero. The reason for observing one peak in nonplanarity per beat in the simulations of low beat frequency $\omega = 0.05\sqrt{ma^2/k_bT}$ instead of two as experimentally observed and simulation for beat frequency $\omega = 0.1\sqrt{ma^2/k_bT}$, remains unclear and needs further investigation. More experimental data and a systematic exploration of the phase space will provide better agreement and thereby might resolve this open question.

Chapter 4

Cilia

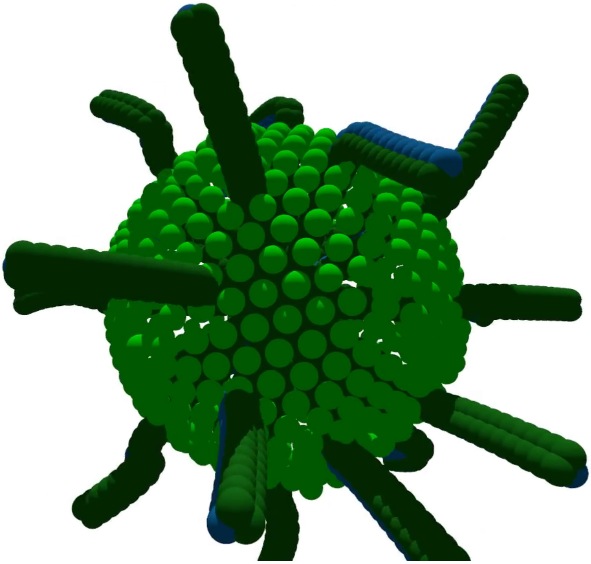

4.1 Ciliated Microswimmers

4.1.1 Volvox & Chlamydomonas

Alga, like *Volvox* or *Chlamydomonas* (Drescher et al., 2009; Jeanneret, Contino, and Polin, 2016) expose cilia on their surface to propel themselves and to enhance the transportation of nutrition towards their cell membrane. The dense cilia arrangement on the surface leads to interactions between cilia that changes the beat pattern. Eventually, cilia beat in an organized fashion and stable states of synchronization develop. Inspired by the complex and rich dynamic of ciliated microswimmers like *Chlamydomonas* (Jeanneret, Contino, and Polin, 2016), *Paramecium* (Omoto and Kung, 1980) or *Volvox* (Brumley, Polin, et al., 2015) a model system to study the influence of hydrodynamic and elastic interactions on the synchronization of cilia is proposed. The surface of the sphere mediates the elastic interactions, whereas the hydrodynamic interactions originate from the motion of the cilia through the fluid and the whole-body motion of the swimmer.

The ciliated sphere described in section 4.1.2 shows different swimming behavior depending on the placement of the cilia on its surface. Once the swimmer is in motion the flow field surrounding the sphere influences each cilium. Depending on the position of the cilia on the sphere, the swimmer transforms from a puller type swimmer to a pusher type (Lighthill, 1976; Zhu, Lauga, and Brandt, 2012). As discussed in section 2.1.5 the flow field of a swimmer that is pushing its cell body differs from a swimmer that is pulling its cell body, which might influence the state of synchronization. Section 4.1.3 discusses the effect on cilia placement with increasing density on the propulsion velocity of the swimmer, followed by a discussion of different synchronization states of cilia with symmetric arrangements on the sphere (section 4.1.4).

4.1.2 Multi-ciliated Sphere Model

The multi-ciliated swimmer consists of a sphere of radius $r_h = 16\ l_b$ with cilia anchored on its surface. The sphere is modeled by 634 beads, connected by springs, that form a triangulated mesh. The axoneme of a cilium is longer

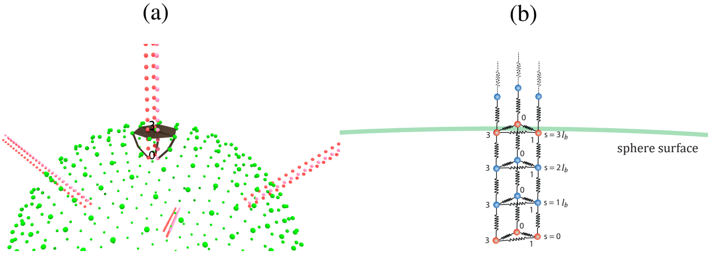

Figure 4.1 **Multi-ciliated sphere model** - **(a)** The spherical body of the ciliated swimmer consists of beads on its surface (green), which are connected to their neighbors by springs. Each cilium consists of two passive filaments (red) and one active filament (rose) which defines the beat direction. The anchoring area and its connections to the cilium are visualized in brown. **(b)** The red beads of the cilium at $s = 0$ and $s = 3\ l_b$ are anchored to the surface of the sphere by harmonic springs. Each bead (red) connects to the closest bead of the spherical surface (green). To distribute the force better the next neighbors on the surface are connected to the cilium beads as well.

than the one of a sperm cell. Yet, structurally similar enough, so the modeling approach of sperm cell can be adapted to simulated ciliary beating (section 2.4.3). Each cilium has a total length of $L = 26\ l_b$, where l_b is the bond length separating neighboring beads. The first part of the axoneme till $s \leq 3\ l_b$ ($n_0 = 3$) is passive and embedded into the sphere, which models the basal body of the cilium (Lindemann and Lesich, 2010). The part above the surface is actively beating and has a length of $25\ l_b$ ($n_L = 28$). The power stroke of all cilia points towards the south pole of the sphere leading to a net-propulsion of the swimmer in the direction of the north-pole. The fluid surrounding the swimmer is simulated using MPC (section 2.3.3). Time for all simulations is measured in units of beat periods τ_b of an isolated cilium attached to a solid surface and the corresponding beat frequency $f_0 = 1/\tau_b$.

Figure 4.1 shows the anchoring of the cilium (red) to the sphere (green). Harmonic springs (shown as brown tubes) attach the first particle (0) of each cilia rod to the closest particle on the surface of the sphere and its next neighbors. The fourth bead (3) of each rod, which lies on the surface of the sphere, is connected in the same way. The brown area on the surface of the sphere shows this anchoring area, where each rod is connected to the closest bead on the sphere and its neighbors.

The cilia positions on the surface of the sphere are specified by spherical coordinates: the latitude $\psi \in (-90°, 90°)$ and the longitude $\theta \in (0°, 360°)$. Instead of specifying each cilium position individually, cilia are placed along latitudes. For each latitudinal ring ψ_{ring} the number of cilia N_{ring} and the offset of the first cilia θ_{ring} on the ring are specified. Cilia are always evenly spaced on each ring with a distance of $2\pi/N_i$.

4.1.3 Effect of Cilia Arrangement on Propulsion Velocity

In order to study the dependence of the average propulsion velocity on cilia arrangement, 47 swimmers with semi-random cilia placements are simulated. Cilia positions are not completely chosen at random, but in a way to ensure a minimal distance between cilia. The number of latitudinal rings $N^{Rings} = \{1..8\}$ along which the cilia are placed is defined per simulation batch. For each number of rings N_{Rings} between 4 and 6 simulations are run. The following algorithm generates the cilia placements for each simulation: For each ring k its latitude ψ_k between $-60°$ and $60°$, its number of cilia N_k between 2 and 8, and the position of the first cilium on the ring θ_k are randomly chosen. Cilia are uniformly spaced on each longitudinal ring to ensure minimal longitudinal distance of $\Delta\theta = 45°$. Cilia placements with a $\Delta\psi < 10°$ are rejected to ensure a minimal latitudinal distance as well.

Figure 4.2 shows the mean propulsion velocity of such semi-randomly constructed swimmers. The configurations with larger than average mean propulsion velocity have a larger variance in propulsion velocity as well, which might indicate (partial) synchronization of cilia. The trend (red line) shows a sub-linear increase of the propulsion velocity with the number of cilia. It saturates for $N_{cilia} > 40$ as the cilia density growth. For small numbers of cilia (up to 10) the propulsion velocity increases linear with the number of cilia. At around 6 cilia the distribution of mean propulsion velocity becomes highly dependent on the distribution of cilia on the surface of the sphere. Even, swimmers with similar numbers of cilia show large differences in propulsion velocity that do not follow the overall increase. The combined center of mass motion and the interaction between cilia leads to a complex coupled interaction which will render some cilia configurations more efficient than others. Since the propulsion velocity varies a lot for an individual swimmer

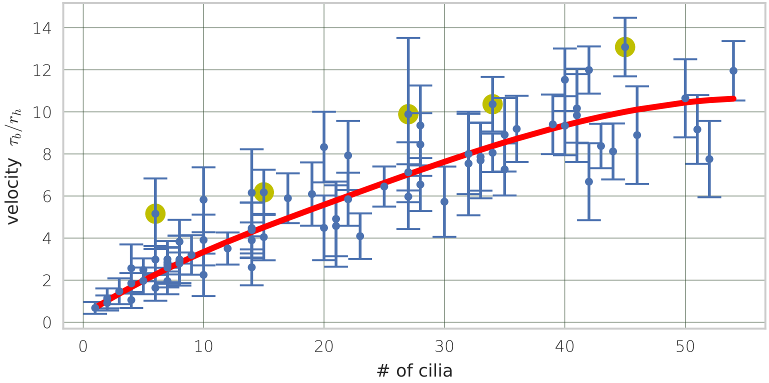

Figure 4.2 **Propulsion velocity** - The average propulsion velocity and its fluctuation of ciliated microswimmers for quasi-random placement of cilia are measured in sphere radius r_h per cilia beat period τ_b. It increases sub-linearly with the number of cilia on the swimmer. The swimmers with maximal velocity in each decade of number of cilia are marked yellow and are visualized in Fig. 4.3. The red line is a fitted spline following the weighted local average.

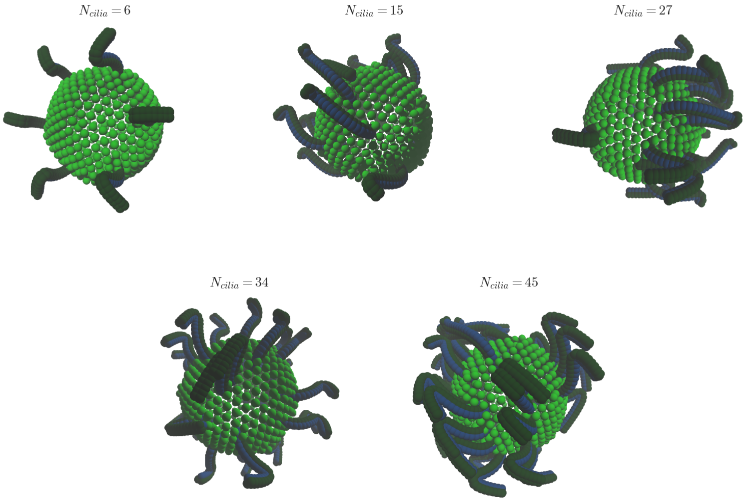

Figure 4.3 **Fastest ciliated microswimmers per decade** - The three-dimensional representation shows the cilia placements of the fastest microswimmer for each decade of number of cilia.

as well as between cilia configuration with similar cilia densities, the five configurations with the highest propulsion velocity per decade are shown in Fig. 4.3. The fast-moving swimmers do not have a common cilia distribution. Neither a stable synchronization state is observed. Some cilia get stuck, show short time entanglement but eventually diverge. Since no straight-forward common features for the faster swimmers emerge, the following analysis turns to simpler cilia arrangement.

4.1.4 Synchronization on Symmetrically Ciliated Swimmers

The states of synchronization of two types of highly symmetric swimmers are investigated. The 3-cilia swimmer has three cilia placed equally spaced around its equator and the 9-cilia swimmer has two additional rings of cilia at $\psi = \pm 45^\circ$. In order to vary initial conditions, the start position for the first cilium on the ring is set to a latitude value of **(a)** $\theta_0 = 0^\circ$, **(b)** $\theta_0 = 40^\circ$ and **(c)** $\theta_0 = 80^\circ$. These 3-cilia swimmers are shown in Fig. 4.4. The symmetric

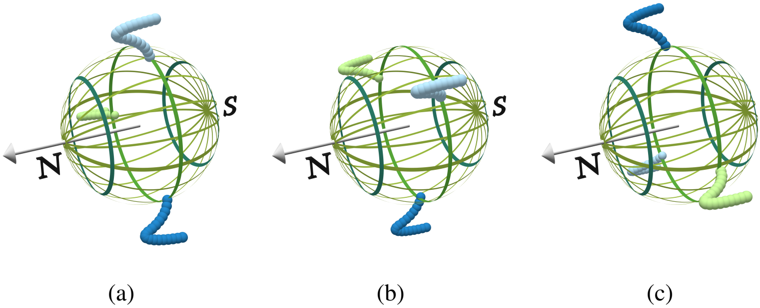

(a) (b) (c)

Figure 4.4 **Three 3-cilia swimmers** - Cilia are located equidistant around the equator of each swimmer. The N-S arrow indicates the swimming direction. The three swimmers only differ in cilia arrangement around their equator. The first cilium (light-blue) of each swimmer is placed at a longitude of (a) $\theta_0 = 0°$, (b) $\theta_0 = 40°$ and (c) $\theta_0 = 80°$. The longitudinal distance between all three cilia on each swimmer is $120°$.

swimmers are identical, except for a rotation of the cilia locations along the equator.

For each cilium its phase along the limit cycle φ_0, φ_1 and φ_2 is extracted (section A.2). This allows to quantify the state of synchronization by the difference between the phase of each cilium and the mean phase of the swimmer:

$$\bar{\chi}_i = \varphi_i(t) - \frac{1}{N_{cilia}} \sum_i \varphi_i. \tag{4.1}$$

All simulations start with synchronous beating cilia, i.e. $\bar{\chi}_i = 0$. The time development of the phase differences over time are shown in Fig. 4.5. Only for the swimmer **(a)** a constant phase difference between cilia establishes after 50 cilia beats. Thus, the three cilia beat with the same frequency $1.033 \pm 0.005\ f_0$. Cilium 0 (light-blue) leads with respect to cilium 2 (green) by a phase difference of $34 \pm 1°$. Cilium 2 is followed by cilium 1 (dark-blue) with a phase difference of $42 \pm 3°$. For swimmer **(b)** and **(c)** no constant phase difference emerges within the simulation time of 120 cilia beats. Instead, the cilia beats drift apart. Cilium 0 leads in swimmer **(b)** with an average beating frequency $1.038 \pm 0.005\ f_0$, followed by cilium 2 with $1.032 \pm 0.006\ f_0$ and finally cilium 1 with $1.030 \pm 0.005\ f_0$, whereas in swimmer **(c)** cilium 2 leads

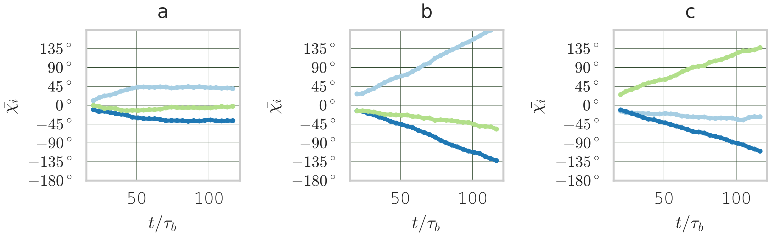

Figure 4.5 **Phase differences of three 3-cilia swimmers** - The phase difference for each cilium with respect to the mean phase of all cilia of the swimmer is colored according to the cilium color in Fig. 4.4. Swimmer **(a)** synchronizes, whereas the phase differences of swimmer **(b)** and **(c)** drift almost constantly apart.

with an average beating frequency of $1.035 \pm 0.005\ f_0$, followed by cilium 0 with $1.032 \pm 0.006\ f_0$ and finally cilium 1 with $1.029 \pm 0.004\ f_0$. Even though, the relative difference in cilia beating frequencies is small, the almost constant phase drift results in a large phase difference between the fastest and the slowest cilium after $t = 120\ \tau_b$. For swimmer **(b)** the phase difference between the fastest and slowest cilium add up to 317°, which is almost a full beat cycle. For swimmer **(c)** the phase difference adds up to 244°. One might expect all swimmers to behave the same. However, they reach different co-existing states of cilia synchronization.

The different synchronization states are reflected in the velocity distribution of the swimmer (Fig. 4.6). In order to obtain a velocity vector which is not dominated by thermal fluctuations the center-of-mass motion of the swimmer is smoothed by taking the gliding average in a window of size Δw along the trajectory. By projecting the velocity vector onto the main north-south-axis of the swimmer the propulsion velocity distribution has positive values when the swimmer moves in the north pole direction which implies the majority of the cilia beating towards the south pole (power-stroke). Negative velocities, opposing the average propulsion velocity, occur when the majority of cilia beat towards the north pole (recovery stroke). The mean propulsion velocity stays the same at $0.2\ r_h/\tau_b$ for all three swimmers. It is not much influenced

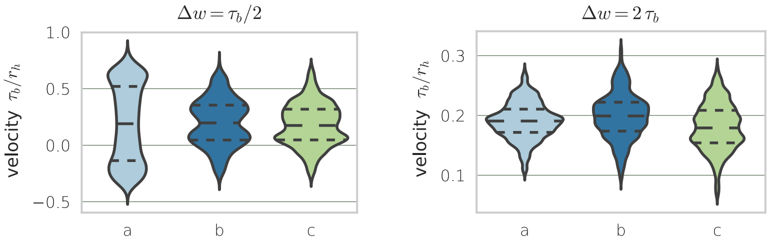

Figure 4.6 **Propulsion velocity distribution** - The propulsion velocity distributions of the 3-cilia swimmers **(a, b, c)** are visualized as violin plots. The long-dashed line indicates the mean and the short-dashed lines the quartiles of the distribution. The propulsion vector is projected on the north-south axis of the swimmer giving raise to positive velocities for motion in the direction of the north pole (power stroke) and negative values when the swimmer moves in the direction of the south pole (recovery stroke). Trajectories are smoothed with two different windows sizes $\Delta w = \tau_b/2$ and $\Delta w = 2\ \tau_b$ by applying a gliding average.

by the coordinated beating of the cilia which reflects the previous finding that significant differences in propulsion velocity start to occur for swimmers with more than 6 cilia. The velocity distribution quantifies the difference between the synchronized cilia beating of system **(a)** and the systems with drift **(b, c)**. How much of the cilia coordination is captured by the distribution depends on the averaging window size Δw.

Figure 4.6 compares a window size of $\Delta w = \tau_b/2$, which still resolves the oscillating motion of the cilia beating with the propulsion distribution for a window size of $\Delta w = 2\ \tau_b$ where the average smooths the trajectory so that the rocking like motion, created by the difference of power and recovery stroke, is not resolved. The difference of synchronized cilia beating only shows in the distribution obtained for small window size $\Delta w = \tau_b/2$ (Fig. 4.6 left). Here, the propulsion velocity distribution of swimmer **(a)** is much more elongated than for swimmer **(b)** and **(c)**. For swimmer **(a)** the power-stroke velocity peaks at almost 1.0 r_h/τ_b and the recovery stroke velocity at $-0.4\ r_h/\tau_b$. Since the total phase difference between the slowest and fastest cilium is about a quarter of the beat cycle, power and recovery strokes of all three cilia still overlap, which might explain the spread in propulsion velocity distribution around the mean without effecting the average propulsion velocity.

Even the 3-cilia swimmers show several states of synchronization. System **(a)** reaches a synchronization state with constant phase differences between the cilia, which results in a broader propulsion velocity distribution, but no significant change in the average propulsion velocity. Therefore, swimmers are constructed with increased cilia density, which might facilitate the development of latitudinal waves along the cilia on the surface of the swimmer.

The 9-cilia swimmer is constructed by adding two additional rings with 3 cilia. Now, in total 9 cilia are located on three rings: the equator, and $\theta = \pm 45^\circ$. The start position of the first cilium on each ring is shifted by a constant offset $\Delta\theta$ with respect to the proceeding ring. The longitudinal distance between cilia on consecutive ring is thereby varied. Five different configurations with $\Delta\theta = 10^\circ, 20^\circ, 40^\circ, 60^\circ$ and 70° are simulated.

The phase difference $\bar{\chi}_i$ of each cilium to the mean phase of the swimmer is plotted in Fig. 4.8. Swimmers start with synchronized beating of all cilia. Cilia on all swimmers except swimmer **(h)** desynchronize over time. The average beat frequency of cilia on swimmers **(d, e, f)** ($\Delta\theta = 10^\circ - 40^\circ$) fluctuates around $1.051 \pm 0.01\ f_0$, whereas swimmer **(g, h)** beat with a slower average frequency $1.036 \pm 0.006\ f_0$ ($\Delta\theta = 60^\circ$) and $1.044 \pm 0.002\ f_0$ ($\Delta\theta = 70^\circ$). Cilia on the surface of swimmer **(h)** synchronize with a constant phase lag. After $t = 40\ \tau_b$ the cilia beat with approximately the same frequency, explaining the smaller fluctuations of the average beating frequency. For all other swimmers the three cilia located near the north pole beat slower than the ones close to the equator and south pole. The slow cilia of swimmer **(d, e, f)** beat with $1.040 \pm 0.008\ f_0$, whereas the fast cilia near the south pole beat with $1.058 \pm 0.003\ f_0$. However, the cilia in each group do not sync to a common frequency. Swimmer **(g)** exhibits two groups of cilia which synchronize to two different frequencies. Thus, the groups drift apart from each other. The first group consists of the cilia on the south-ring and on the the equatorial ring. They beat faster than the cilia on the ring close to the north pole. The average frequency of the fast group is $1.040 \pm 0.002\ f_0$, whereas the slower one beats with $1.029 \pm 0.002\ f_0$. Note the significant lower fluctuations within each group. Only swimmer **(h)** shows a stable phase difference in form of a

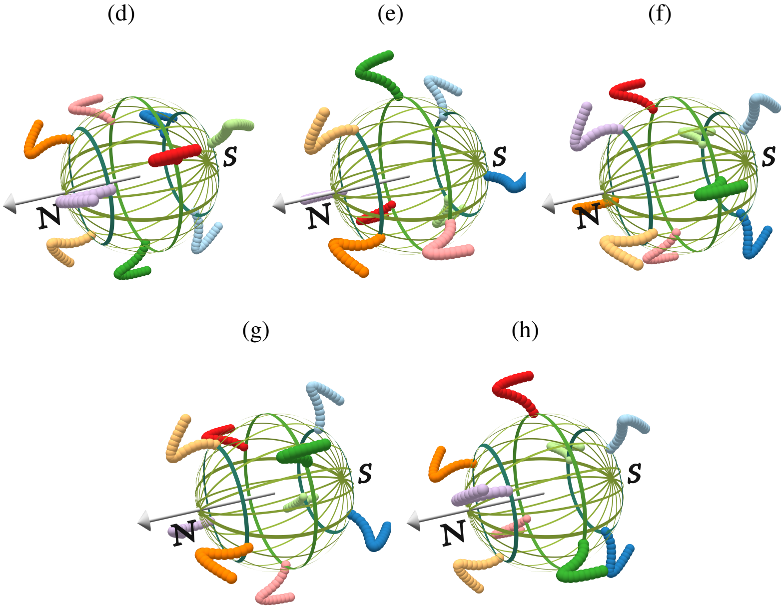

Figure 4.7 **9-cilia swimmers** - Three cilia are located equidistant on the latitudes $\psi_0 = 45°$, $\psi_1 = 0°$ and $\psi_2 = -45°$. The N-S arrow indicates the swimming direction. the Each ring is shifted by $\Delta\theta$ of **(d)** 10°, **(e)** 20°, **(f)** 40°, **(g)** 60° and **(h)** 70° with respect to the subsequent ring. The phases of each cilium in following plots (Fig. 4.8) are colored according to its colors here.

.

traveling wave. The wave roughly travels from the south to the north pole. The phase difference between cilia, which is calculated as the average over 10 beats starting from t=40 τ_b, varies. The smallest average phase difference between cilium 5 and 3 is $\varphi_5 - \varphi_3 = 2 \pm 5°$, whereas the largest difference between cilium 8 and 6 is $\varphi_8 - \varphi_6 = 40 \pm 5°$.

The propulsion velocity distribution (Fig. 4.9) reflects the enhancement due to the coordinated beating of swimmer **(h)** $\theta = 70°$ by a shift to a 30 percent higher average propulsion velocity. The swimmer **(g)** shows an enhanced propulsion velocity by about 15 percent, whereas the higher average beat frequency of the drifting swimmers **(d, e, f)** does not result in an enhancement of mean propulsion velocity compared to swimmer **(g, h)**.

4.1.5 Conclusion

Ciliated swimmers show a sub-linear increase with increasing cilia density. The large fluctuations for different cilia configurations result from the fact that even completely symmetric simple swimmers arrive in different states of synchronization. Indeed, in a simpler oscillator model Ghorbani and Najafi (2017) showed that in complex geometries the emergence of metachronal coordination depends on the initial state of the oscillators. For swimmers with high cilia densities, in particular for the symmetric 9-cilia swimmer with $\Delta\theta = 70°$ shift between successional rings, metachronal coordination emerges and results in an increase of the mean propulsion velocity. The slightly higher reported beating frequencies of multi cilia arrangements compared to single ones agree with previous theoretical studies (Gueron and Levit-Gurevich, 1999). However, studying synchronization of a few cilia on a spherical object turned out to be more complex and dependent on initial conditions, as well as modeling details, than anticipated.

Still, these findings are related to experimentally observed findings. Ciliary tufts exhibit stable metachronal synchronization within tufts that rapidly decreases when tufts are not connected. Then, different wavelength as well as uncorrelated cilia motion is found (Gheber and Priel, 1989). The dense and boundary free placement of cilia on the spherical surface of *Volvox* leads to the formation of stable metachronal waves around the meridian of the alga (Brum-

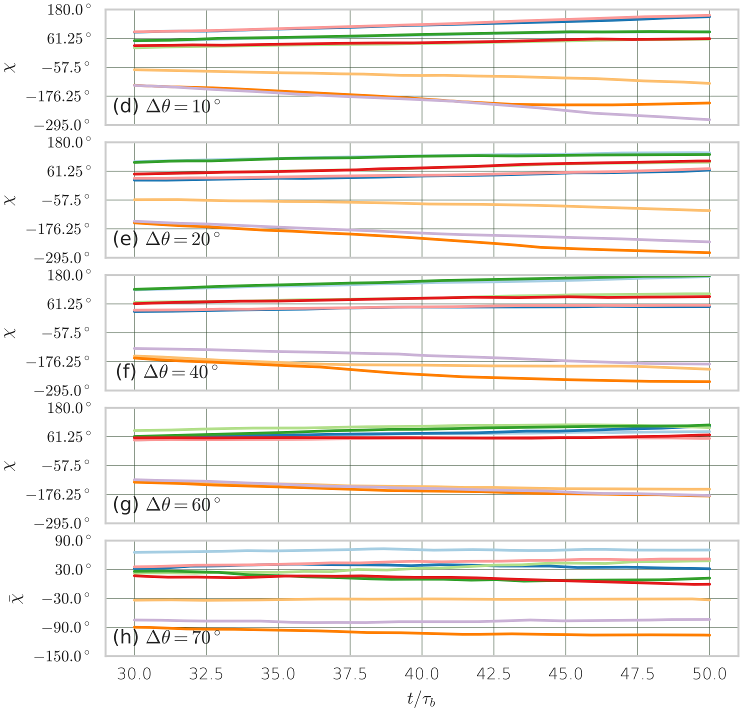

Figure 4.8 **Phase difference of the 9-cilia swimmers** - The phase difference between each cilium and the mean phase of the swimmer is colored according to the color of the cilium in the swimmer sketches in Fig. 4.7. Only the swimmer with $\Delta\theta = 70°$ synchronizes with a constant phase lag. For all swimmers cilia located near the north-pole (orange, yellow, purple) lag behind or beat slower than the cilia located near the south-pole (green, blue, light-blue).

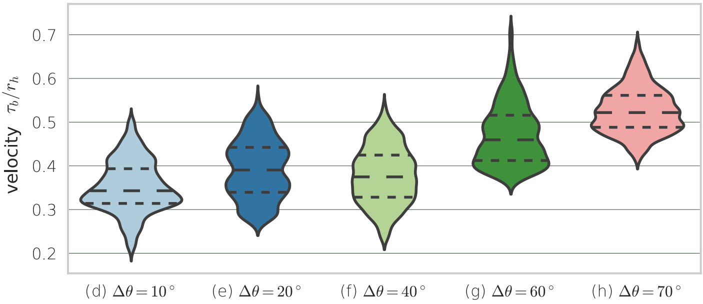

Figure 4.9 **Propulsion velocity distributions of 9-cilia swimmers** - The propulsion velocity distributions of the 9-cilia swimmers are visualized as violin plot where the long-dashed line indicates the mean and the short-dashed lines the quartiles of the distribution. The velocity is obtained from a trajectory with averaging windows size $\Delta w = 2\ \tau_b$. Therefore, no sign change in propulsion is observed, due to the different direction of power and recovery stroke. The two swimmers **(g, h)** that show stable states of synchronization show an enhanced propulsion velocity.

ley, Polin, et al., 2015; Brumley, Wan, et al., 2014). Therefore, hydrodynamic synchronization of cilia on the spherical surface of *Volvox* proved possible, whereas phase locking of the ciliary beat of *Chlamydomonas* to external flow fields is only achieved for flows which are larger than physiological conditions (Quaranta, Aubin-Tam, and Tam, 2015). The two cilia on the surface of *Chlamydomonas* show regions of phase-locking with significant slip-regions in between, where the phase difference of the two cilia increases rapidly (Wan, Leptos, and Goldstein, 2014). Recent experiments on multiciliated algae show a complex variation of cilia beat patterns, depending on basal-body interactions and cilia placement (Wan and Goldstein, 2016). Because the variety and complexity of synchronization observed experimentally and a strong dependency of the model on initial conditions, the complexity in the next section is further reduced.

4.2 Synchronization Patterns in Cilium Oscillators

4.2.1 Motivation

Due to the complexity of the full cilia model, a minimal model for hydrodynamic synchronization of oscillators is studied. The most pronounced feature of cilia dynamics is the cyclic movement. Instead of modeling the entire dynamics of the cilium, the model is reduced to a single bead on a closed trajectory, which mimics the motion of the tip of a cilium. In the spirit of minimal modeling the simplest closed trajectory is chosen here: a circle. Tilting the circle towards the surface includes the different hydrodynamic drag of the power (further away from the surface) and recovery stroke (close to the surface). If the bead is moved along a predefined trajectory with constant tangential driving force, no synchronization occurs. It is sufficient for the occurrence of hydrodynamic synchronization to allow for radial flexibility by constraining the motion of the bead along the trajectory via harmonic potentials. This cilium oscillator model, as first suggested by Niedermayer, Eckhardt, and Lenz (2008), allows studies of synchronization patterns in deterministic systems of oscillators for different topologies: two hydrodynamically interacting oscillators above a surface, a chain and a circular arrangement of oscillators. The beauty of the models lies in the control of one single nondimensionalized parameter λ_c which controls the confinement strength of the trajectory compared to the driving force. A large value of λ_c results in stiff trajectories, whereas small values allow large deviations that are critical for long range synchronization patterns to emerge.

4.2.2 Cilium Oscillator Model

The system is modeled by N oscillating beads. They are simulated by hydrodynamical Langevin dynamics (section 2.3.2). Tensor-based interaction either model an infinite fluid volume (Oseen) or a boundary at $z = 0$ (Blake).

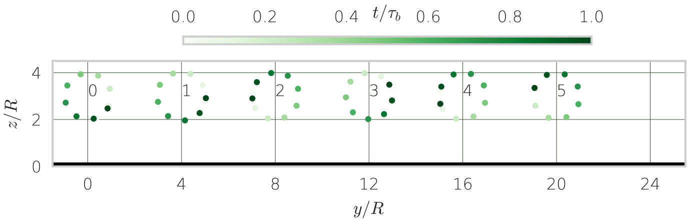

Figure 4.10 **Chain of oscillators** - The chain of oscillators above a surface at $z = 0$ is oriented along the y-direction. Each oscillator consists of a point particle, moving along a circular trajectory with radius R and a period τ_b. The position of the beat along one beating cycle is colored from white ($t = 0$) over green ($t = 0.5\tau_b$) to black ($t = \tau_b$). The oscillators are numbered with increasing index along the chain in the tangential beating direction close to the surface.

A tangential driving force $\mathbf{F}_d$ drives the bead around the predefined trajectory:

$$\mathbf{F}_d = f_0\, \mathbf{t}(\varphi), \tag{4.2}$$

and two normal forces restore the beads deviation from the predefined trajectory with a harmonic potential of strength γ_c:

$$\mathbf{F}_{normal} = -\gamma_c\left((\mathbf{r}-\mathbf{r_0})\cdot\mathbf{n}-R\right)\,\mathbf{n} \tag{4.3}$$
$$\mathbf{F}_{bi-normal} = -\gamma_c(\mathbf{r}-\mathbf{r_0})\cdot\mathbf{m}\,\mathbf{m}. \tag{4.4}$$

The beads move along a circular trajectory of radius R, that is tilted towards the surface by an angle α_t. The corresponding orientation vectors are given by:

$$\mathbf{t} = \begin{pmatrix} -\sin(\varphi) \\ \cos(\varphi)\cos(\alpha_t) \\ -\cos(\varphi)\sin(\alpha_t) \end{pmatrix} \tag{4.5}$$

$$\mathbf{n} = \begin{pmatrix} \cos(\alpha_t)\sin(\varphi) \\ -\cos(\alpha_t)\sin(\varphi) \\ -sin(\varphi)\sin(\alpha_t) \end{pmatrix} \tag{4.6}$$

$$\mathbf{m} = \begin{pmatrix} 0 \\ -\sin(\alpha_t) \\ \cos(\alpha_t) \end{pmatrix} \tag{4.7}$$

$$\tag{4.8}$$

The phase of the oscillator φ is given by the position of the bead along the circle tilted by α_t around the x-axis:

$$\begin{aligned} dx &= r^x - r_0^x \\ dy &= r^y - r_0^y \\ dz &= r^z - r_0^z \\ \varphi &= \operatorname{atan2}\left(dy\ \cos(\alpha_t) + dz\ \sin(\alpha_t),\ dx\right) \end{aligned} \tag{4.9}$$

The oscillator equations are nondimensionalized by choosing the trajectory radius R as a length scale $\mathbf{r}' = \mathbf{r}/R$, the driving force f_0 as a force scale $\mathbf{F} = \mathbf{F}/f_0$ and using the self-mobility of the bead μ_0 to set the time scale as $t' = tR/(\mu_0 f_0)$):

$$\mu_0 f_0 \frac{dr'}{dt'} = \mu_0 f_0 \left(\mathbf{t} - \frac{\gamma_c R}{f_0}\left(\left(\mathbf{r}' - \mathbf{r}'_\mathbf{0}\right)\cdot\mathbf{n} - 1\right)\ \mathbf{n}\left(\mathbf{r}' - \mathbf{r}'_\mathbf{0}\right)\cdot\mathbf{m}\right)\ \mathbf{m}\right), \tag{4.10}$$

where $\lambda_c = \gamma_c R/f_0$ is the only control parameter that determines the confinement strength. The undisturbed angular velocity equals $\omega = 2\pi R/f_0$ due to the nondimensionalized mobility. In order to stay in the far field limit of the Oseen tensor, a bead size of $l_b/R = 0.1$ is used. In the presence of a surface, the mobility of the bead is reduced, according to Eq. (2.21).

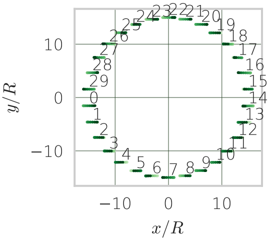

Figure 4.11 **Circular arrangement of oscillators** - Oscillators (green) are arranged on a circle of radius $R_c = 15\ R$ at a height of $z = 1.5\ R$ above the surface. Their beat plane lies within the xz axis. The oscillators are numbered with increasing index in counter clockwise direction around the circle.

The phase difference between successive oscillators is defined as $\chi_i = \varphi_{i+1} - \varphi_i$. Oscillators of the chain are numbered from one end to N along the chain (Fig. 4.10), whereas oscillators in the circular arrangement are numbered in counter clockwise direction (Fig. 4.11).

The phase difference maps into the interval between $\pm\pi$ by applying the linear transformation $\chi \leftarrow (\chi + \pi)\%2\pi + \pi$. When a constant steady state value of the phase difference develops, this is called phase lag.

4.2.3 Results

In the first part synchronization between two oscillators for confinement strength $\lambda_c = 10$ and different inclinations with respect to the surface are studied. A pair of oscillators tends to synchronize with a topologically-dependent, finite phase lag. The second part extends the simulation studies to chains of cilia, where metachronal waves are observed. The results are compared to the case of two interacting oscillators.

Two oscillators in an infinite fluid synchronize without a phase lag. The vicinity of the surface breaks the symmetry and introduces a phase lag χ, which depends on the position above the surface z, the distance between the two centers of the oscillators d, the orientation of the trajectory α_t with respect to the surface and the confinement strength λ_c.

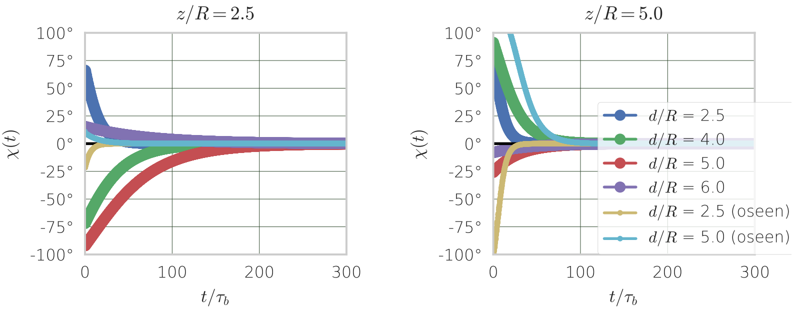

Figure 4.12 **Time relaxation of two oscillators** - The phase difference of two oscillators with parallel orientation towards the surface and confinement strength $\lambda_c = 10$ located at a distance of z above the surface with varying center-to-center distances d synchronize with zero phase lag $\chi = 0$ on different time scales.

Figure 4.12 compares the synchronization behavior of two oscillators for different distances d between oscillators and different heights above the surface as well as the configuration for a free fluid without any boundaries (Oseen tensor). All oscillators sync with zero phase lag $\chi = 0$. The synchronization time, which is the time it takes to reach zero phase difference, increases when approaching the surface and with increasing distance between oscillators. The further away from the surface the oscillators are, e.g. for $z/R = 5.0$, the more they approach the time scales of the free fluid case. An inclination of oscillators with respect to the surface $\alpha_t \neq 0$ leads to nonzero phase lag 4.13. Maximal phase lag is reached between oscillators with perpendicular orientation to the surface $\alpha_t = 90°$. At a height of $z/R = 3$ the phase lag reaches a value of $\chi = 40°$. The phase lag decreases with increasing distance to the surface. Far away from the surface the phase lag approaches zero, since the influence of the wall vanishes. The phase lag is a function of the proximity to the surface and the inclination of the trajectory.

Turning to chains of equally spaced oscillators, the state of synchronization is additionally influenced by boundaries. Therefore, chains with different numbers of oscillators are simulated. For the confinement strength $\lambda_c = 1.0$ metachronal waves emerge in chains with 10 oscillators of parallel $\alpha_t = 0°$

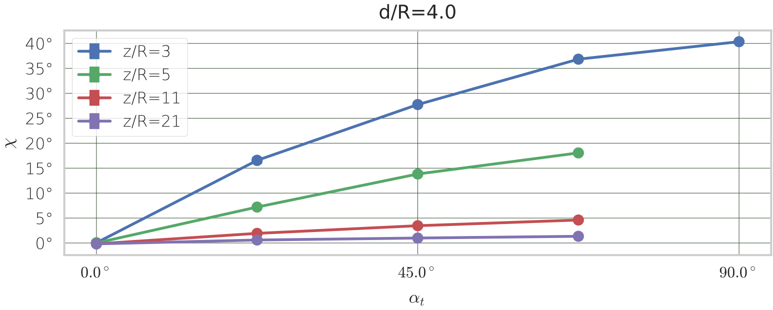

Figure 4.13 **Stationary phase lag of two oscillators** - The steady state value of the phase lag between two oscillators with confinement strength $\lambda_c = 10$ above a surface depends on the inclination angle and the height above the surface. For inclined trajectories above a surface $\alpha_t \neq 0$ the phase lag is non-zero. Maximal phase lag is reached for $\alpha_t = 90°$ and $z/R = 3$.

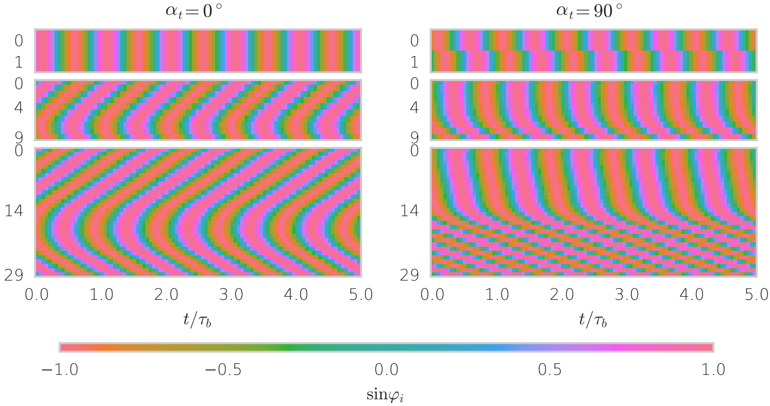

Figure 4.14 **Metachronal waves in chains** - The Kymograph shows the emergence of metachronal waves for chains of oscillators with confinement strength $\lambda_c = 1.0$ in parallel $\alpha_t = 0°$ and perpendicular $\alpha_t = 90°$ orientation to the surface. Note, that the emergence of metachronal waves does not depend on a finite phase lag between two oscillators.

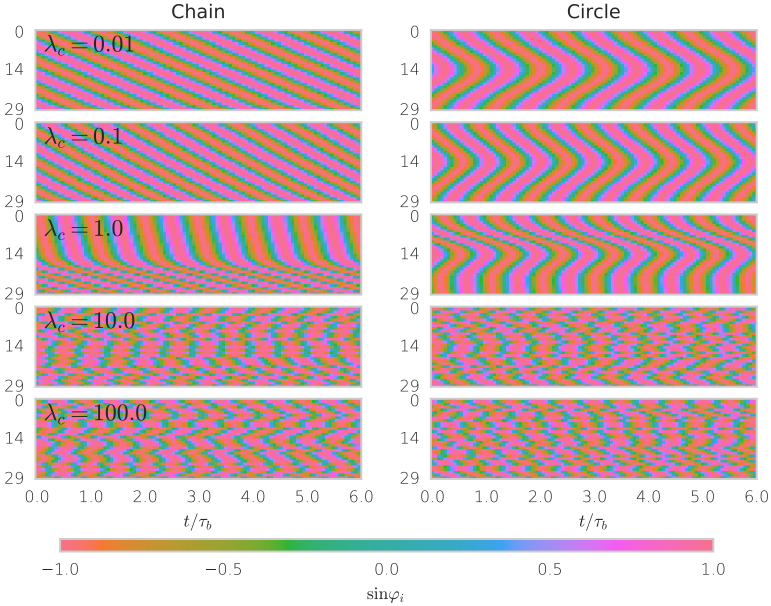

Figure 4.15 **Chain vs. circle** - Kymograph showing oscillator phase of circular and chain arrangements of oscillators for $\alpha_t = 90°$. Metachronal waves emerge for confinement strength equal and below $\lambda_c = 0.1$.

and perpendicular $\alpha_t = 90°$ orientation (Fig. 4.14). The initial phase lag between two oscillators is not critical for metachronal coordination. The initial symmetry can also be broken by the open boundaries of the chain. In the parallel orientation the metachronal wavelength stays constant, yet the wave reverses direction at the center of the chain. In the chain of 10 oscillators, the wave changes direction close to the boundary, whereas for a longer chain with 30 oscillators the traveling wave emerges from the middle of the chain. For the perpendicular orientation of oscillators boundaries heavily influence the synchronization pattern as well. Interestingly, this leads to two sharply separated regions with small and large wavelength.

No metachronal waves emerge for circular arranged, parallel oriented oscillators. When symmetry is broken by tilting oscillators towards the surface by $\alpha_t = 90°$, a variety synchronization patterns emerge (Fig. 4.15). By comparing the open chain to a circular arrangement with radius $R_c = 15\ R$ of oscillators

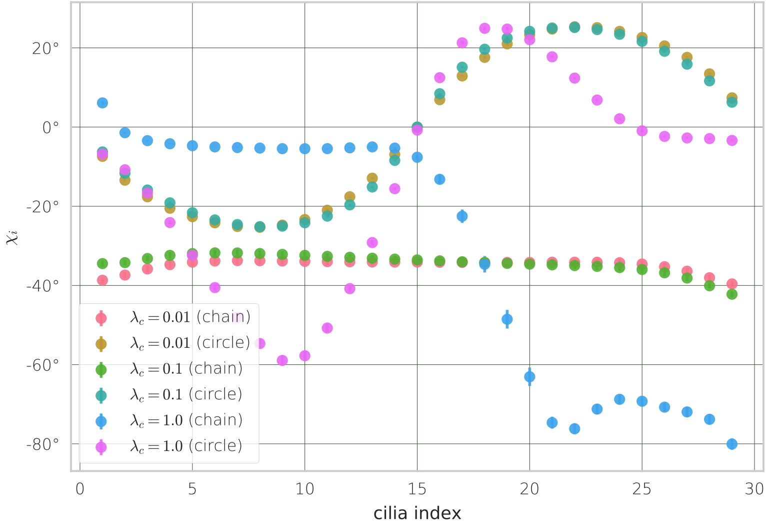

Figure 4.16 **Phase difference of oscillators** - The phase difference of successive oscillators χ_i is compared for different confinement strength λ_c in chains and circular arrangements. All oscillators are oriented perpendicular to the surface $\alpha_t = 90°$.

(Fig. 4.11), the influence of boundaries on the emerging state of synchronization is further investigated. Stable waves form for confinement strengths $\lambda_c \leq 1.0$. For weak confinement strength $\lambda_c \leq 0.1$, perfect metachronal waves form in the chain, whereas a chevron pattern forms in the circular arrangement.

The stable waves are analyzed by measuring the phase lag of successive oscillators χ_i (Fig. 4.16) for all configurations that develop a stable synchronization pattern. For the chain and weak confinements $\lambda_c \leq 0.1$ the phase lag is almost constant $\chi \approx -35^\circ$, whereas for a confinement strength of $\lambda_c = 1.0$ the phase lag rapidly changes from $\langle\chi\rangle_{i\leq 15} = 5^\circ$ to $\langle\chi\rangle_{i\geq 20} = 70^\circ$ over an almost linear transition region of 5 oscillators. For circular arrangements no metachronal waves emerge. For weak confinements $\lambda_c \leq 0.1$ the phase lags take a sinusoidal form instead, which is symmetrically around zero phase lag and has an amplitude of 25°. For strong confinement $\lambda_c = 1.0$ the symmetry is broken by a shift of the sinusoidal dependency towards negative values. The largest phase lag between oscillator 9 and 10 is -60°, whereas the oscillators 25 to 0 almost perfect synchronize $\chi = 0$. The phase lag in the two-oscillator case translates to “chaotic” motion in a chain (bottom of Fig. 4.15). Only significantly weaker confinement strength allows for stable synchronization states to emerge. In particular, the phase lag of zero for the planar orientation of oscillators translates to a chevron like pattern for long chains of 30 oscillators.

4.2.4 Conclusions

The study of two oscillators above a surface quantifies the phase lag in synchronization. Maximal phase lag of $\chi = 40^\circ$ is achieved for oscillators beating perpendicular to the surface ($\alpha_t = 90^\circ$). The phase lag decreased with the distance of the oscillators to the surface. Nevertheless, metachronal coordination develops in open chains with more than 10 oscillators for all orientations with the surface for weak confinement $\lambda_c \leq 1.0$. These results are in agreement with those of a recent study of Brumley, Polin, et al. (2012).

A strong influence of boundaries at medium confinement $\lambda_c = 1$ is found. The metachronal wave compresses towards the end of the chain, which points along the beating direction. Stronger confinement $\lambda_c = 10$ leads to short pair-wise partially synchronization that shows no stable long-term correlations. The critical value of λ_c, restricting metachronal coordination, could explain the difficulties to observe ciliary synchronization in the full cilia model (section 4.1). The high noise in MPC simulations and the relatively strong flows, needed to slow down the beating of the cilia in the Brownian ratchet model, create a narrow window where metachronal synchronization seems possible.

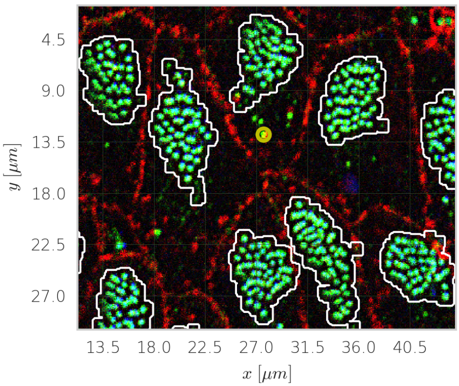

Figure 4.17 **Confocal microscopy image of ependymal tissue** - The primary cilia (yellow) is surrounded by tufts of motile cilia (white) in a quasi-hexagonal like structure. Motile and imotile cilia are stained in green, whereas cell junctions are stained in red. (from: A. Meunier (2016)).

4.3 Particle Transport in Cilia Tufts

4.3.1 Ciliary Tufts in Brain Ventricles

Cilia exposed on the surface of cells often occur in bunches forming tufts. Such tufts of motile cilia cover the surface of mammalian brain ventricles. The cerebrospinal fluid (CSF) flows through these cavities. During ependymal cilia development, motile cilia orient along the direction of the CSF flow (Molla-Herman et al., 2010) which is important to establish left-right symmetry. Once cilia are fully developed, their orientation becomes fixed. The arrangement of motile and primary cilia in ependymal tissue shows a quasi-hexagonal arrangement (Fig. 4.17). Neuronal stem-cells expose a primary cilium into the surface of the brain ventricles where they can interact with the fluid flow. Stem-cell development originating from the primary cilia is important during brain development and proper function. If the signaling cascade of the primary cilia is knocked-out, the formation of neuronal stem-cells is inhibited (Sawamoto et al., 2006).

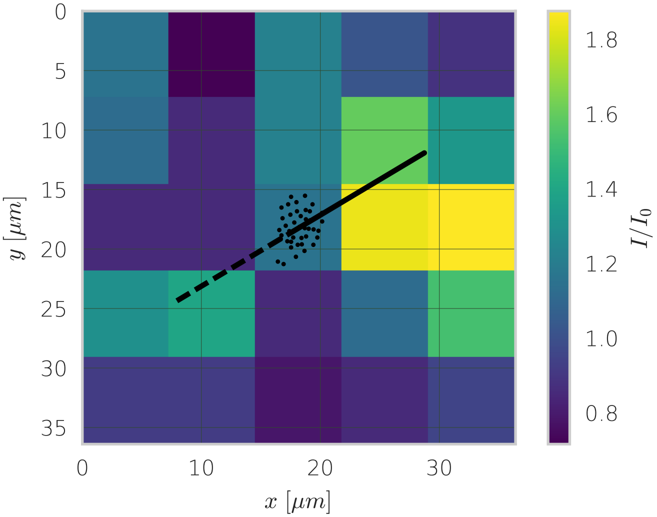

Figure 4.18 **Distribution of tracked particles** - The heat map shows the enhancement of particle flux I towards the xy-surface compared to purely diffusive transport I_0. In the hot-spot area (yellow) the flux density increases by up to 60 percent. Black dots mark the position of the individual cilia in the tuft. The bold (dashed) black line shows the direction of the power (recovery) stroke.

In this section the benefit of motile cilia around primary cilia is investigated. The fluid flow generated by the active beating of the cilia is simulated to examine its effect on particle transport towards the surface.

4.3.2 Modeling and Data Extraction

From the experimental data, which is provided by collaborators from Nathalie Spassky lab at ENS Paris, cilia coordination within a tuft is extracted using image processing. A tuft is rebuilt in the simulation by placing cilia in the same relative arrangement as in the original tuft. The base of each cilium is fixed at the surface. The simulation uses periodic boundary conditions in x and y direction, and a no-slip surface at the bottom and a slip surface at the top. Tufts are modeled in a simulation box of dimensions $L_x = 70a$, $L_y = 70a$ and $L_z = 30a$. Therefore, the beating of cilia in an infinite array of tufts with around 50 motile cilia creates the flow. By inserting tracer molecules, modeled as a tetrahedron with edge length a, the enhancement of flow towards the surface compared to passive diffusion is measured. The dimensions of the cilia match the experimentally observed sizes in brain tissue of mice.

FET, a signaling molecule, that is part of the brain fluid, has a diffusion constant of $0.518 \pm 0.016\ \mu m^2/s$. Considering the beat parameters of the cilia, as listed in Table 4.1, the Péclet number of the active particle transport, created by the ciliary beat, is $Pe = l_{motile}^2 f_{cilia}/D_{EGF} = 9000 \pm 6000$.

Table 4.1 Experimental scales of cilia tufts

l_{motile}	$12.2 \pm 2.1 \mu m$
d_{motile}	$\approx 0.3 \mu m$
$l_{primary}$	$0.9 \pm 0.3 \mu m$
N_{tuft}	≈ 50
f_{cilia}	$30 \pm 10 Hz$
D_{EGF}	$0.518 \pm 0.016 \mu m^2/s$

The mean beat period $\tau_b = 560\sqrt{k_b T/(ma^2/)}$ of a cilium in the simulated tuft is limited by the constraint of keeping the system in the low Reynolds limit. The low friction is reflected in the high noise of the system, leading to a diffusion constant $D_{\text{tracer}} = 0.012\sqrt{a^2/(k_b T^3 m)}$ of free dilute tetrahedron tracker molecules. This results in a Péclet number $Pe = 82$ for the simulation.

Thus, the diffusive transport is overestimated in the simulation. Effects of advective transport in the simulation will enhance with increasing Péclet number.

4.3.3 Results

At the start of the simulation $N_T = 490$ tracer particles are inserted in the volume V_s of the top layer of the fluid at random positions. This results in an average tracer particle density of $\rho_T = N_T/V_s = 0.1\ a^{-3}$. The tracers move in the flow field of the ciliary beating until they diffuse below the height of the primary cilium, $z = 2a$. If tracer particles arrive at this critical height, they are reinitialized by inserting them again at a random position in the starting volume. Additionally, their traveling time and impact coordinate on the surface are logged. This allows to determine the flux of particles towards the surface when they get absorbed at the height of the primary cilium. In Fig. 4.18 the flux of tracer particles towards the surface is shown. The ciliary beating has a twofold effect. First it increases the total flux towards the surface and second it localizes the particles in specific areas. The flux density in hot spots is about 80% higher than the influx of particle due to pure diffusion. Even though simulation results show a significant enhancement, the location of the hot-spot area does not coincide with the location of primary cilia. A simulation which includes the entire pinwheel arrangement will most likely change the location of the hot-spot area and most likely improve the result.

Due to the large noise present in MPC simulations, the diffusive transport is highly overestimated. In the current setup, the inserted tracking participles act more like tracers, following the flow towards the surface. Therefore, especially the localization of the flux due to the ciliary beating is interesting. The localization can be understood by the vortices that enhance particle transport towards the surface in specific areas. A similar enhancement has been shown experimentally in reef corals (Shapiro et al., 2014) using video microscopy. Ciliary beating increases oxygen transport towards the surface by up top 300%.

Chapter 5

Summary & Conclusions

The dynamics of flagellar beating and its consequences on trajectories as well as synchronization of ciliated microswimmers have been analyzed. Details of the beat shape critically determine the swimming path and propulsion velocity of ciliated microswimmers. Hydrodynamic simulations of sperm (single flagellum swimmers), swimming under confinement, reproduce experimental data, gain additional insight on the behavior of active particles in complex environments and help to propose new microfluidic experiments for the guidance of sperm. The importance of nonplanar beating leads to the development of a new approach to model the dynamics of flagellar beating. A Kirchhoff elastic rod model enables the study of filaments with values for the twist and bending rigidities of biological relevance.

The surface attraction of sperm, swimming along the sidewall of zigzag channels is mainly determined by steric interactions. A static, steric model covering the averaged beat-shape envelope of the beating sperm cell successfully describes the average deflection around corners. Planar beat-patterns tend to align with the nearest surface which leads to a bi-modal stability for sperm swimming near the corner of a channel. When the sperm beats parallel to the sidewall, the beat shape does not interact sterically with the sidewall which results in small deflection angles. On the contrary, a beat-plane orientation parallel to the top or bottom walls exposes the cone-like average beat-shape towards the sidewall. This leads to an inclination of the sperm towards the sidewall and eventually significant higher deflection angles. Therefore, the orientation and stability of the beat plane determines the deflection and thereby the overall trajectory of sperm in structured micro channels. Those two possible stable orientations are found to be the reason for the broad deflection angle distribution which is found in experiments as well as simulations. In particular the simulation results agree to experimentally measured deflection of sperm.

Even though the model with a planar beat successfully describes propulsion properties of sperm, it turns out that the three-dimensional beat pattern of the flagellum is crucial in the understanding of motion under confinement. Above a critical wavelength $\lambda = 0.7\ L$ the axoneme exhibits a small out-of-plane component which depends on the beat frequency. For $\lambda \geq 0.9$ perfect surface attraction is achieved for both tested frequencies. Using this result, a filtering between straight and buckled sperm cells could be achieved. While swimming along round corners of radius $R = 2.8\ L$, planar beating sperm detach and cross to the opposing channel side, whereas nonplanar beating sperm swim around the corner and stay attached to the same sidewall. These simulation results pose interesting questions how surface interactions guide sperm through complex and highly confined geometries. They emphasize the importance of resolving the three-dimensional beat shape, specifically turning the interest towards the underlying buckling dynamics.

By extending the planar beating sperm cell model to a semi-flexible polymer, where bending and twist rigidities can be specified independently, the transition from planar to three-dimensional beat pattern has been analyzed in more detail.

A phase-space study confirms a critical twist rigidity, which is two orders of magnitude below the corresponding experimental bending rigidity. In this unstable regime a twist instability, which propagates along the main axis of the filament, leads to the splitting of the planar beat pattern into two planes. These results agree with the performed analysis of experimental data of human sperm cells, where the same oscillating nonplanarity as in simulations is observed.

Synchronization of the beating of many cilia on the surface of spherical microswimmers is more difficult to achieve than expected. Even though a constant phase lag develops for some simple configurations, the generalization of the previously used cilium model from a planar arrangement to more complex spherical geometries turns out to be difficult. Within the used ratchet-like cilia model, the switching point between power and recovery stroke determines the change in cilia beat frequencies. In the regime of stable beating, the hydrodynamic interactions between cilia seem to be very weak and several states of synchronization coexist. A scan of swimmers with randomly placed cilia shows a sub-linear increase of propulsion speed with cilia density. For swimmers with symmetric cilia arrangement, stable coordinated cilia beating is observed and shown to increase the propulsion efficiency by about 30 percent. Due to the difficulties of reaching stable synchronization, a minimal model in order to study the conditions for emergence of metachronal coordination is investigated. The cilium oscillator model allows the control of the coupling strength between oscillators. When operating below a critical confinement strength, stable metachronal coordination emerges within a chain of oscillators. Boundaries turned out to be important in determining direction and shape of the wave.

The combination of experimental and simulation data is crucial in understanding the high-dimensional problem of self-propulsion of multi-ciliated microswimmers. Finding the predicted twist instability in experimental data helps in refining the proposed model and restricting the simulation regime to meaningful parametric values. Simulations provide details such as twisting and bending energies, that help to enhance the recorded data by information which is difficult, if not impossible, to obtain experimentally. In particular, the combination of confinement and the improved axoneme model, which undergoes a twist instability, proposes an interesting topic for further investigation. The sudden transition from planar to complex three-dimensional beat shapes has been shown to effect surface attraction and swimming path of sperm cells.

By analyzing the beat-shape envelope and the rolling of sperm, the resulting surface guidance can be predicted and eventually tested using the full hydrodynamic simulation techniques in confinement. Variations of beat pattern among species could relate to the very specific environmental conditions cells encounter. Especially, guidance and selectivity of the fittest sperm might be accomplished via their differences in beat shape and frequency and their effect on surface attraction. Sperm respond to signaling molecules by changes in beat frequency as well as wavelength. The inclusion of such response in the developed sperm model will have an effect on the out-of-plane component and thereby influence surface attraction heavily. This further elaboration will improve the understanding of the surface guidance mechanism in sperm navigation towards the egg cell.

The established ciliated-swimmer model can be extended to simulate more complex cilia arrangements. The doublet-cilia found on many algae are connected by elastic fibers. The altering of synchronization behavior by such an additional coupling poses an interesting problem, which seems feasible to address. In particular, a finer control of the beat shape of the cilia would allow to study cilia with different intrinsic frequencies. Direct control of the confinement strength, as discussed in the cilium oscillator model, would allow the testing of different interaction regimes and improve the understanding of synchronization on the propulsion velocity and swimming path of such complex swimmers.

The study of complex cilia topologies, including defects, is feasible within the simple oscillator model. Especially, the numerical efficiency and the single parameter control enables simulations of even large fields. The emergence of symmetry breaking along linear chains of oscillators looks promising in helping to improve the understanding left-right symmetry breaking during embryogenesis. For example, the oscillators model could be extended to allow for induced tilting of the imposed trajectory.

Overall the combination of multi-scale approaches, starting from the cilium oscillator model to study complex arrangement to more complex ciliated swimmers that might eventually allow direct mapping to experimentally observed data, provides a way to elucidate the origin of the beautiful complex world of ciliary synchronization patterns.

Bibliography

Ainley, Josephine et al. (2008). "The Method of Images for Regularized Stokeslets." In: *Journal of Computational Physics* 227(9), pp. 4600–4616.

Allen, Mike P and Dominic J Tildesley (1989). *Computer Simulation of Liquids*. Oxford university press.

Amann, Rupert P. and David F. Katz (2004). "Andrology Lab Corner*: Reflections on CASA after 25 Years." In: *Journal of andrology* 25(3), pp. 317–325.

Bailey, A. G. et al. (2009). "Accurate Simulation Dynamics of Microscopic Filaments Using "caterpillar" Oseen Hydrodynamics." In: *Phys. Rev. E* 80(4), p. 046707.

Bayly, Philip V. and Kate S. Wilson (2014). "Equations of Interdoublet Separation during Flagella Motion Reveal Mechanisms of Wave Propagation and Instability." In: *Biophysical Journal* 107(7), pp. 1756–1772.

Berbari, Nicolas F. et al. (2009). "The Primary Cilium as a Complex Signaling Center." In: *Current Biology* 19(13), R526–R535.

Berg, Howard C (2008). *E. Coli in Motion*. Springer Science & Business Media.

Berg, Howard C and Douglas A Brown (1972). "Chemotaxis in Escherichia Coli Analysed by Three-Dimensional Tracking." In: *Nature* 239(5374), pp. 500–504.

Blake, J. R. (1971). "A Note on the Image System for a Stokeslet in a No-Slip Boundary." In: *Mathematical Proceedings of the Cambridge Philosophical Society* 70 (02), p. 303.

Brokaw, Charles J (1971). "Bend Propagation by a Sliding Filament Model for Flagella." In: *Journal of Experimental Biology* 55(2), pp. 289–304.

Brokaw, Charles J. (1972). "Computer Simulation of Flagellar Movement: I. Demonstration of Stable Bend Propagation and Bend Initiation by the Sliding Filament Model." In: *Biophysical Journal* 12(5), pp. 564–586.

Brokaw, Charles J. (2005). "Computer Simulation of Flagellar Movement IX. Oscillation and Symmetry Breaking in a Model for Short Flagella and Nodal Cilia." In: *Cell Motility and the Cytoskeleton* 60(1), pp. 35–47.

Brokaw, Charles J. (1961). "Movement and Nucleoside Polyphosphatase Activity of Isolated Flagella from Polytoma Uvella." In: *Experimental Cell Research* 22, pp. 151–162.

Brumley, Douglas R., Marco Polin, et al. (2012). “Hydrodynamic Synchronization and Metachronal Waves on the Surface of the Colonial Alga Volvox Carteri.” In: *Phys. Rev. Lett.* 109(26), p. 268102.

Brumley, Douglas R., Marco Polin, et al. (2015). “Metachronal Waves in the Flagellar Beating of Volvox and Their Hydrodynamic Origin.” In: *Journal of The Royal Society Interface* 12(108), p. 20141358.

Brumley, Douglas R., Kirsty Y. Wan, et al. (2014). “Flagellar Synchronization through Direct Hydrodynamic Interactions.” In: *eLife* 3, e02750.

Bukatin, Anton et al. (2015). “Bimodal Rheotactic Behavior Reflects Flagellar Beat Asymmetry in Human Sperm Cells.” In: *Proceedings of the National Academy of Sciences* 112(52), pp. 15904–15909.

Camalet, Sébastien and Frank Jülicher (2000). “Generic Aspects of Axonemal Beating.” In: *New Journal of Physics* 2(1), p. 24.

Darnton, Nicholas C. et al. (2007). “On Torque and Tumbling in Swimming Escherichia Coli.” In: *Journal of Bacteriology* 189(5), pp. 1756–1764.

Darwin, Charles (1859). *The Origin of Species by Means Or Natural Selection Or The Preservation of Favoured Races in the Struggle for Life*.

Davenport, James R. and Bradley K. Yoder (2005). “An Incredible Decade for the Primary Cilium: A Look at a Once-Forgotten Organelle.” In: *AJP: Renal Physiology* 289(6), F1159–F1169.

Davies Wykes, Megan S. et al. (2017). “Guiding Microscale Swimmers Using Teardrop-Shaped Posts.” In: *Soft Matter* 13(27), pp. 4681–4688.

Denissenko, Petr et al. (2012). “Human Spermatozoa Migration in Microchannels Reveals Boundary-Following Navigation.” In: *Proceedings of the National Academy of Sciences* 109(21), pp. 8007–8010.

Drescher, Knut et al. (2009). “Dancing \textit{Volvox} : Hydrodynamic Bound States of Swimming Algae.” In: *Phys. Rev. Lett.* 102(16), p. 168101.

Eamer, Lise et al. (2016). “Turning the Corner in Fertility: High DNA Integrity of Boundary-Following Sperm.” In: *Lab Chip* 16(13), pp. 2418–2422.

Eisenbach, Michael and Laura C. Giojalas (2006). “Sperm Guidance in Mammals ? An Unpaved Road to the Egg.” In: *Nature Reviews Molecular Cell Biology* 7(4), pp. 276–285.

Elgeti, Jens and Gerhard Gompper (2013). “Emergence of Metachronal Waves in Cilia Arrays.” In: *Proceedings of the National Academy of Sciences* 110(12), pp. 4470–4475.

Elgeti, Jens and Gerhard Gompper (2008). “Hydrodynamics of Active Mesoscopic Systems.” In: NIC Symposium. Vol. 39, pp. 53–62.

Elgeti, Jens, U. Benjamin Kaupp, and Gerhard Gompper (2010). “Hydrodynamics of Sperm Cells near Surfaces.” In: *Biophys. J.* 99(4), pp. 1018–1026.

Elizabeth Hulme, S. et al. (2008). “Using Ratchets and Sorters to Fractionate Motile Cells of Escherichia Coli by Length.” In: *Lab on a Chip* 8(11), p. 1888.

Ermak, Donald L. and Andrew J. McCammon (1978). “Brownian Dynamics with Hydrodynamic Interactions.” In: *The Journal of Chemical Physics* 69(4), pp. 1352–1360.

Eyckmans, Jeroen et al. (2011). “A Hitchhiker’s Guide to Mechanobiology.” In: *Developmental Cell* 21(1), pp. 35–47.

Fauci, Lisa J. and Amy McDonald (1995). “Sperm Motility in the Presence of Boundaries.” In: *Bulletin of mathematical biology* 57(5), pp. 679–699.

Fliegauf, Manfred, Thomas Benzing, and Heymut Omran (2007). “When Cilia Go Bad: Cilia Defects and Ciliopathies.” In: *Nature Reviews Molecular Cell Biology* 8(11), pp. 880–893.

Friedrich, Benjamin M. et al. (2010). “High-Precision Tracking of Sperm Swimming Fine Structure Provides Strong Test of Resistive Force Theory.” In: *Journal of Experimental Biology* 213(8), pp. 1226–1234.

Gabor, Dennis et al. (1948). “A New Microscopic Principle.” In: *Nature* 161(4098), pp. 777–778.

Gaffney, Eamonn A. et al. (2011). “Mammalian Sperm Motility: Observation and Theory.” In: *Annual Review of Fluid Mechanics* 43(1), pp. 501–528.

Gheber, Larisa and Zvi Priel (1989). “Synchronization between Beating Cilia.” In: *Biophysical journal* 55(1), pp. 183–191.

Ghorbani, Aref and Ali Najafi (2017). “Symplectic and Antiplectic Waves in an Array of Beating Cilia Attached to a Closed Body.” In: *Phys. Rev. E* 95(5), p. 052412.

Gibbons, Ian R. and A. J. Rowe (1965). “Dynein: A Protein with Adenosine Triphosphatase Activity from Cilia.” In: *Science* 149(3682), pp. 424–426.

Gompper, G. et al. (2009). “Multi-Particle Collision Dynamics: A Particle-Based Mesoscale Simulation Approach to the Hydrodynamics of Complex Fluids.” In: *Advanced Computer Simulation Approaches for Soft Matter Sciences III*. Springer: Berlin, Heidelberg, pp. 1–87.

Gueron, Shay and Konstantin Levit-Gurevich (1999). “Energetic Considerations of Ciliary Beating and the Advantage of Metachronal Coordination.” In: *Proceedings of the National Academy of Sciences* 96(22), pp. 12240–12245.

Guidobaldi, A. et al. (2014). “Geometrical Guidance and Trapping Transition of Human Sperm Cells.” In: *Physical Review E* 89(3), p. 032720.

Hilfinger, Andreas (2006). “Dynamics of Cilia and Flagella.” Ph. D. dissertation, TU Dresden.

Hines, Michael and J. J. Blum (1978). “Bend Propagation in Flagella. I. Derivation of Equations of Motion and Their Simulation.” In: *Biophysical Journal* 23(1), p. 41.

Howard, Jonathon (2001). “Mechanics of Motor Proteins and the Cytoskeleton.” In:

Hu, Jinglei et al. (2015). “Modelling the Mechanics and Hydrodynamics of Swimming E. Coli.” In: *Soft Matter* 11(40), pp. 7867–7876.

Huang, Chien-Cheng, A. Chatterji, et al. (2010). “Cell-Level Canonical Sampling by Velocity Scaling for Multiparticle Collision Dynamics Simulations.” In: *Journal of Computational Physics* 229(1), pp. 168–177.

Huang, Chien-Cheng, Anoop Varghese, et al. (2015). “Thermostat for Nonequilibrium Multiparticle-Collision-Dynamics Simulations.” In: *Physical Review E* 91(1), p. 013310.

Ihle, Thomas and Daniel M. Kroll (2003). “Stochastic Rotation Dynamics. I. Formalism, Galilean Invariance, and Green-Kubo Relations.” In: *Physical Review E* 67(6), p. 066705.

Ishijima, Sumio, Miyako S. Hamaguchi, et al. (1992). “Rotational Movement of a Spermatozoon around Its Long Axis.” In: *Journal of experimental biology* 163(1), pp. 15–31.

Ishijima, Sumio and Yukio Hiramoto (1994). “Flexural Rigidity of Echinoderm Sperm Flagella.” In: *Cell structure and function* 19(6), pp. 349–362.

Jeanneret, Raphaël, Matteo Contino, and Marco Polin (2016). “A Brief Introduction to the Model Microswimmer Chlamydomonas Reinhardtii.” In: *The European Physical Journal Special Topics* 225 (11-12), pp. 2141–2156.

Jülicher, Frank and Jacques Prost (1997). “Spontaneous Oscillations of Collective Molecular Motors.” In: *Physical review letters* 78(23), p. 4510.

Kanakasabapathy, Manoj Kumar et al. (2017). “An Automated Smartphone-Based Diagnostic Assay for Point-of-Care Semen Analysis.” In: *Science Translational Medicine* 9(382).

Kantsler, Vasily, Jörn Dunkel, Martyn Blayney, et al. (2014). “Rheotaxis Facilitates Upstream Navigation of Mammalian Sperm Cells.” In: *eLife* 3, e02403.

Kantsler, Vasily, Jörn Dunkel, Marco Polin, et al. (2013). “Ciliary Contact Interactions Dominate Surface Scattering of Swimming Eukaryotes.” In: *Proceedings of the National Academy of Sciences* 110(4), pp. 1187–1192.

Katz, David F., Erma Z. Drobnis, and James W. Overstreet (1989). “Factors Regulating Mammalian Sperm Migration through the Female Reproductive Tract and Oocyte Vestments.” In: *Gamete research* 22(4), pp. 443–469.

Kaupp, U. Benjamin, Nachiket D. Kashikar, and Ingo Weyand (2008). “Mechanisms of Sperm Chemotaxis.” In: *Annual Review of Physiology* 70(1), pp. 93–117.

Kawagishi, Ikuro et al. (1996). “The Sodium-Driven Polar Flagellar Motor of Marine Vibrio as the Mechanosensor That Regulates Lateral Flagellar Expression.” In: *Molecular microbiology* 20(4), pp. 693–699.

Kim, Sangtae and Seppo J. Karrila (2013). *Microhydrodynamics: Principles and Selected Applications*. Courier Corporation.

Kis, A. et al. (2002). “Nanomechanics of Microtubules.” In: *Physical Review Letters* 89(24).

Knowlton, Stephanie M., Magesh Sadasivam, and Savas Tasoglu (2015). “Microfluidics for Sperm Research.” In: *Trends in Biotechnology* 33(4), pp. 221–229.

Kralemann, Björn et al. (2008). “Phase Dynamics of Coupled Oscillators Reconstructed from Data.” In: *Physical Review E* 77(6), p. 066205.

Lauga, Eric (2014). “An Introduction to the Hydrodynamics of Locomotion on Small Scales.” In: *arXiv preprint arXiv:1403.4093*.

Lee, Sang-Hyuk and David G. Grier (2007). “Holographic Microscopy of Holographically Trapped Three-Dimensional Structures.” In: *Optics Express* 15(4), pp. 1505–1512.

Lighthill, James (1976). “Flagellar Hydrodynamics.” In: *SIAM review* 18(2), pp. 161–230.

Lighthill, James (1989). *Mathematical Biofluiddynamics*. CBMS-NSF regional conference series in applied mathematics 17. Society for Industrial and Applied Mathematics: Philadelphia.

Lindemann, Charles B. (2002). “Geometric Clutch Model Version 3: The Role of the Inner and Outer Arm Dyneins in the Ciliary Beat.” In: *Cell Motility and the Cytoskeleton* 52(4), pp. 242–254.

Lindemann, Charles B. and Kathleen A. Lesich (2010). “Flagellar and Ciliary Beating: The Proven and the Possible.” In: *Journal of Cell Science* 123(4), pp. 519–528.

Lowe, Christopher P (2001). “A Hybrid Particle/Continuum Model for Micro-Organism Motility.” In: *Future Generation Computer Systems*. Particle Based Modelling Methods Applied in Biology 17(7), pp. 853–862.

Löwen, Hartmut (1999). “Anisotropic Self-Diffusion in Colloidal Nematic Phases.” In: *Physical Review E* 59(2), p. 1989.

Machemer (1974). “Cilia and Flagella.” In: Academic Press, pp. 199–286.

Malevanets, Anatoly and Raymond Kapral (1999). “Mesoscopic Model for Solvent Dynamics.” In: *The Journal of chemical physics* 110(17), pp. 8605–8613.

McCarter, Linda, Marcia Hilmen, and Michael Silverman (1988). “Flagellar Dynamometer Controls Swarmer Cell Differentiation of V. Parahaemolyticus.” In: *Cell* 54(3), pp. 345–351.

Miki, Kiyoshi and David E. Clapham (2013). “Rheotaxis Guides Mammalian Sperm.” In: *Current Biology* 23(6), pp. 443–452.

Molla-Herman, Anahi et al. (2010). “The Ciliary Pocket: An Endocytic Membrane Domain at the Base of Primary and Motile Cilia.” In: *Journal of Cell Science* 123(10), pp. 1785–1795.

Mortimer, Sharon T. (1997). “A Critical Review of the Physiological Importance and Analysis of Sperm Movement in Mammals.” In: *Human Reproduction Update* 3(5), pp. 403–439.

Niedermayer, Thomas, Bruno Eckhardt, and Peter Lenz (2008). “Synchronization, Phase Locking, and Metachronal Wave Formation in Ciliary Chains.” In: *Chaos: An Interdisciplinary Journal of Nonlinear Science* 18(3), p. 037128.

Nonaka, Shigenori et al. (1998). “Randomization of Left–right Asymmetry Due to Loss of Nodal Cilia Generating Leftward Flow of Extraembryonic Fluid in Mice Lacking KIF3B Motor Protein.” In: *Cell* 95(6), pp. 829–837.

Nosrati, Reza, Amine Driouchi, et al. (2015). “Two-Dimensional Slither Swimming of Sperm within a Micrometre of a Surface.” In: *Nature Communications* 6, p. 8703.

Nosrati, Reza, Percival J. Graham, et al. (2016). “Predominance of Sperm Motion in Corners.” In: *Scientific Reports* 6, p. 26669.

Omoto, Charlotte K. and Ching Kung (1980). “Rotation and Twist of the Central-Pair Microtubules in the Cilia of Paramecium.” In: *The Journal of cell biology* 87(1), pp. 33–46.

Ooi, E. H. et al. (2014). “The Mechanics of Hyperactivation in Adhered Human Sperm.” In: *Royal Society Open Science* 1(2), pp. 140230–140230.

Ott, Edward and Thomas M. Antonsen (2008). “Low Dimensional Behavior of Large Systems of Globally Coupled Oscillators.” In: *Chaos: An Interdisciplinary Journal of Nonlinear Science* 18(3), p. 037113.

Poblete, Simón et al. (2014). “Hydrodynamics of Discrete-Particle Models of Spherical Colloids: A Multiparticle Collision Dynamics Simulation Study.” In: *Physical Review E* 90(3), p. 033314.

Purcell, Edward M. (1977). “Life at Low Reynolds Number.” In: *American Journal of Physics* 45(1), pp. 3–11.

Quaranta, Greta, Marie-Eve Aubin-Tam, and Daniel Tam (2015). “Hydrodynamics Versus Intracellular Coupling in the Synchronization of Eukaryotic Flagella.” In: *Physical Review Letters* 115(23), p. 238101.

Ripoll, Marisol, K. Mussawisade, et al. (2005). “Dynamic Regimes of Fluids Simulated by Multiparticle-Collision Dynamics.” In: *Physical Review E* 72(1), p. 016701.

Ripoll, Marisol, K Mussawisade, et al. (2004). “Low-Reynolds-Number Hydrodynamics of Complex Fluids by Multi-Particle-Collision Dynamics.” In: *EPL (Europhysics Letters)* 68(1), p. 106.

Robinson, Lynne et al. (2012). “The Effect of Sperm DNA Fragmentation on Miscarriage Rates: A Systematic Review and Meta-Analysis.” In: *Human Reproduction* 27(10), pp. 2908–2917.

Rothschild (1963). “Non-Random Distribution of Bull Spermatozoa in a Drop of Sperm Suspension.” In: *Nature* 200(4904), pp. 381–381.

Saggiorato, Guglielmo et al. (2017). “Human Sperm Steer with Second Harmonics of the Flagellar Beat.” In: *arXiv preprint arXiv:1703.07705*.

Sartori, Pablo et al. (2016). “Dynamic Curvature Regulation Accounts for the Symmetric and Asymmetric Beats of Chlamydomonas Flagella.” In: *eLife* 5, e13258.

Satir, Peter (1985). “Switching Mechanisms in the Control of Ciliary Motility.” In: *Modern cell biology* 4, pp. 1–46.

Satir, Peter and Søren Tvorup Christensen (2007). “Overview of Structure and Function of Mammalian Cilia.” In: *Annual Review of Physiology* 69(1), pp. 377–400.

Satir, Peter, Lotte B. Pedersen, and Søren Tvorup Christensen (2010). “The Primary Cilium at a Glance.” In: *Journal of Cell Science* 123(4), pp. 499–503.

Sawamoto, Kazunobu et al. (2006). “New Neurons Follow the Flow of Cerebrospinal Fluid in the Adult Brain.” In: *Science* 311(5761), pp. 629–632.

Shapiro, Orr H. et al. (2014). “Vortical Ciliary Flows Actively Enhance Mass Transport in Reef Corals.” In: *PNAS* 111(37), pp. 13391–13396.

Söderlind, Gustaf (2002). “Automatic Control and Adaptive Time-Stepping.” In: *Numerical Algorithms* 31 (1-4), pp. 281–310.

Spagnolie, Saverio E. and Eric Lauga (2012). “Hydrodynamics of Self-Propulsion near a Boundary: Predictions and Accuracy of Far-Field Approximations.” In: *Journal of Fluid Mechanics* null, pp. 105–147.

Spagnolie, Saverio E., Gregorio R. Moreno-Flores, et al. (2015). “Geometric Capture and Escape of a Microswimmer Colliding with an Obstacle.” In: *Soft Matter* 11(17), pp. 3396–3411.

Strünker, Timo et al. (2011). “The CatSper Channel Mediates Progesterone-Induced CaŜup 2+Înflux in Human Sperm.” In: *Nature* 471(7338), p. 382.

Su, Ting-Wei, Liang Xue, and Aydogan Ozcan (2012). “High-Throughput Lensfree 3D Tracking of Human Sperms Reveals Rare Statistics of Helical Trajectories.” In: *Proceedings of the National Academy of Sciences* 109(40), pp. 16018–16022.

Tabeling, Patrick (2005). *Introduction to Microfluidics*. Oxford University Press on Demand.

Ten Hagen, Borge et al. (2015). “Can the Self-Propulsion of Anisotropic Microswimmers Be Described by Using Forces and Torques?” In: *Journal of Physics: Condensed Matter* 27(19), p. 194110.

Valente, Enza Maria et al. (2013). “Primary Cilia in Neurodevelopmental Disorders.” In: *Nature Reviews Neurology* 10(1), pp. 27–36.

Vazquez, J.M. et al. (2009). “Sex-Sorting Sperm by Flow Cytometry in Pigs: Issues and Perspectives.” In: *Theriogenology* 71(1), pp. 80–88.

Vilfan, Andrej and Frank Jülicher (2006). “Hydrodynamic Flow Patterns and Synchronization of Beating Cilia.” In: *Physical Review Letters* 96(5), p. 058102.

Vogel, Reinhard and Holger Stark (2012). “Motor-Driven Bacterial Flagella and Buckling Instabilities.” In: *The European Physical Journal E* 35(2).

Wan, Kirsty Y. and Raymond E. Goldstein (2016). “Coordinated Beating of Algal Flagella Is Mediated by Basal Coupling.” In: *Proceedings of the National Academy of Sciences* 113(20), E2784–E2793.

Wan, Kirsty Y., Kyriacos C. Leptos, and Raymond E. Goldstein (2014). “Lag, Lock, Sync, Slip: The Many ’Phases’ of Coupled Flagella.” In: *Journal of The Royal Society Interface* 11(94), pp. 20131160–20131160.

Wanner, Gerhard and Ernst Hairer (1991). “Solving Ordinary Differential Equations II.” In: *Stiff and Differential-Algebraic Problems*.

Winet, H., G. S. Bernstein, and J. Head (1984). “Observations on the Response of Human Spermatozoa to Gravity, Boundaries and Fluid Shear.” In: *Journal of reproduction and fertility* 70(2), pp. 511–523.

Woolley, D. M. (2003). “Motility of Spermatozoa at Surfaces.” In: *Reproduction* 126(2), pp. 259–270.

Woolley, D. M. and G. G. Vernon (2001). “A Study of Helical and Planar Waves on Sea Urchin Sperm Flagella, with a Theory of How They Are Generated.” In: *Journal of Experimental Biology* 204(7), pp. 1333–1345.

Wysocki, Adam, Jens Elgeti, and Gerhard Gompper (2015). “Giant Adsorption of Microswimmers: Duality of Shape Asymmetry and Wall Curvature.” In: *Phys. Rev. E* 91(5), p. 050302.

Zhu, Lailai, Eric Lauga, and Luca Brandt (2012). “Self-Propulsion in Viscoelastic Fluids: Pushers vs. Pullers.” In: *Physics of Fluids* 24(5), p. 051902.

Zini, Armand et al. (2008). “Sperm DNA Damage Is Associated with an Increased Risk of Pregnancy Loss after IVF and ICSI: Systematic Review and Meta-Analysis.” In: *Human Reproduction* 23(12), pp. 2663–2668.

Appendix A

A.1 Gyration Tensor Decomposition

A consistent local frame of reference can be obtained from the expansion of the flagellum. The diagonalized gyration tensor defines a local orientation for each time frame of the trajectory. It defines three orthogonal vectors of the flagellum which are aligned so they form a right-handed coordinate system with the largest eigenvalue **e** pointing towards the tail of the flagellum, the eigenvector with the second largest eigenvalue **b** gives the direction of the beating.

Since the beating varies periodically in time and space, this vector is only defined up to a factor of ± 1. A time resolution of the obtained data higher than the rolling frequency of the object allows local alignment of the **b** vector between succeeding frames. Finally, the beat-plane normal is defined as a right-handed coordinate system $\mathbf{p} = \mathbf{e} \times \mathbf{b}$. Where **p** defines the normal orientation of the space curve in a co-moving reference frame with respect to center of mass translation and rotation.

The motion of the sperm cell is now described as the superposition of the beat pattern in the local reference frame and the whole-body translation and rotation:

$$\mathbf{r}(s,t) = \mathbf{r}_0(t) + E(s,t)\hat{e}(t) + B(s,t)\hat{b}(t) + P(s,t)\hat{p}(t), \qquad \text{(A.1)}$$

where $\mathbf{r}_0$ is the center of mass motion and E, B and P are the amplitudes of the displacement along the corresponding axes.

A.2 Phase Extraction from Limit Cycle

Introducing a phase description simplifies the study of synchronization in high dimensional systems (Kralemann et al., 2008; Ott and Antonsen, 2008). Assuming the system has a stable limit cycle solution, which means it undergoes stable oscillations, a one-dimensional phase description can be established. The phase describes the position of the system along the closed trajectory of the limit cycle.

The undisturbed motion in the limit cycle has a constant oscillation time τ after which the motion repeats itself:

$$\mathbf{r}(t+\tau_b) = \mathbf{r}(t) \tag{A.2}$$

$$\tag{A.3}$$

The undisturbed phase follows as:

$$\varphi(t) = \omega_0 t, \tag{A.4}$$

where $\omega_0 = 2\pi/\tau_b$ is the intrinsic frequency of the oscillator.

The following steps are applied to extract the phase of the cilium, assuming its center line is described by the space curve $\mathbf{r}(s)$:

- Calculate the orientation of the cilia segment $\delta\mathbf{r}_1 = \mathbf{r}(L/2) - \mathbf{r}(0)$ and $\delta\mathbf{r}_2 = \mathbf{r}(L) - \mathbf{r}(L/2)$
- Calculate the angels between the normal of the cilia $\mathbf{n}$ and two local orientations $\cos\phi_i = \mathbf{r}_i \cdot \mathbf{n}$
- Use the phase space of the limit cycle described by ϕ_1 and ϕ_2 to define a Poincaré section
- Measure the intersection times of this section
- Interpolate a phase from these intersection times.

The details of the concrete phase dependence within one limit cycle is lost, but the relative phase difference between oscillators with respect to the sharp Poincaré section is well defined and extremely noise resistance. A variety of more refined methods exit (Kralemann et al., 2008) to extract a phase from experimental data. In the scope of global states of synchronization the method presented here proved to be most reliable.

A.3 Adaptive Timestep

Adaptive time stepping (Söderlind, 2002) solves an ordinary differential equation numerically in such a way that the integration error is below a given tolerance ε_{tol}. Using forward integration first and than compare the result to backward propagation gives an estimate for the integration error. A simple Euler step propagates the particles forward in time:

$$dr_i^E(t+\tau) = \mu_{ij}(r,t)F_j(r,t)\ \tau \tag{A.5}$$

The difference between the force vector obtained at the new and old position gives rate of change of the force with the current time step. Therefore, it provides an estimate of the integration error $\delta\mathbf{F} = (\overleftrightarrow{\mu}_{ij}(r+dr)\mathbf{F}_j(r+dr) - \overleftrightarrow{\mu} ij(r)\mathbf{F}_j(r))$.

Using the maximal error observed during integration, the time step adapts accordingly to:

$$\tau \leftarrow 0.9 \times 2\ \frac{\varepsilon_{tol}}{\mathbf{max}|\delta\mathbf{F}_j/\mathbf{F}_j|}, \tag{A.6}$$

where the factor 0.9 provides a safety margin due to the error of the error estimate itself.

Finally, the error estimate is used to expand the Euler integration schema to a trapezoidal method, which is stable for stiff-equations (Wanner and Hairer, 1991):

$$
\begin{aligned}
dr_i(t+\tau) &= (\mu_{ij}(r+dr)\,\mathbf{F}_j(r+dr)+\mu_{ij}(r)\,\mathbf{F}_j(r))\;\frac{\tau}{2} \\
&= dr_i^E(t+\tau)+\delta\mathbf{F}_j\;\frac{\tau}{2}.
\end{aligned}
\tag{A.7}
$$

Appendix B

B.1 Simulation Parameters

The parameters used to simulate the presented MD structures are given here. All values are in MPC units. When not otherwise specified in the main text, the spring constant γ_s is set to a large value of $\gamma_s = 20000$ to ensure rigid structure. In table B.1 the parameters used to simulate cilia fixed on surfaces and on spherical swimmers are given. The stall force threshold is set to zero, since thermal fluctuations are strong enough in MPC to drive the cilia beat via the ratchet.

Table B.1 Cilium simulation parameters

parameter	swimmer	fixed
A	0.14	0.11
Q_R	0.7	1.0
Q_P	-0.7	-1.0
$v_{recover}$	5.0	50.0
rodlength	26	50

Acknowledgements

First of all, my deep gratitude goes to Prof. Gerhard Gommper for providing the excellent opportunity to study and to do my research on ciliated microswimmers at the FZ Jülich. Moreover, I want to thank him sincerely for all the support and advice he gave me during this time. I also owe Jens Elgeti, my thesis supervisor, who's door was always open for me, a huge debt of gratitude for many interesting and inspiring discussions, leading to a deeper understanding of the focused topics and having enriched my research process a lot. Being part of the Biosoft Graduate School has been a great pleasure for me, and I am very thankful for this. It provides a constant environment for enhancing exchange and it is perfectly organized by Thorsten Auth. I also want to thank the SPP Microswimmers program for providing funding and a great environment for scientific exchange. Furthermore, I like to thank all the wonderful fellow students at Jülich for the good time we spent together at ICS-2 and of course thanks goes to all the people from Biosoft. Especially I want to mention here Raphael, Nirmalendu, Run Li and Dimitrios, who participated in countless scientific discussions. I am so glad to have meet you and shared an office with all of you. It has been a nice, enriching time. And I want to thank all the train people who managed to turn most DB related delays from a lost time into a fruitful discussion about almost every topic, ranging from science and international politics to family and holidays. I also like to thank Mrs. Paffen and Mrs. Kleine for helping with many of the administrative difficulties and for always providing good advice and guidance on administrative tasks. Thanks also goes to JSC and especially Mrs. Henkel for helping with all IT related issues. Last but not least I want to express my special thanks to An Gong and Luis Alvarez for giving me the opportunity to visit Caesar Research Center and to work together. It was always a great pleasure for me to discuss

with you and I am especially very grateful that An took the time to explain me the experimental setups and showed me how experiments on real, living sperm cells are performed. It helped a lot to switch viewpoint and see the problem from another perspective. Finally, I would like to thank Ina, my brother Julian and my parents for all the help and support they gave me during these not always easy times of working on my thesis.

B.2 Kurzzusammenfassung

Der Antriebsmechanismus und die Schwimmdynamiken verschiedenartiger Mikroorganismen, die mit Zilien ausgestattet sind, werden untersucht. Diese Organismen, die sich von der eingeißligen Spermazelle bis zu Mikroschwimmern mit zahlreichen Zilien erstrecken, treiben sich selbst durch diese Cilien, die an ihrer Zellmembran befestigt sind, an. Die zugrunde liegende, vielschichtige Biomaschinerie eines Ziliums nutzt evolutionär entwickelte Mechanismen, welche darauf zugeschnitten sind, ein optimales Schlagmuster zu erzeugen, damit der Schwimmer sich in seiner Umwelt bewegen kann. In dieser Arbeit werden mesoskopische hydrodynamische Simulationen angewendet, um die peitschenähnliche Bewegung in niedrigen Reynolds-Zahlen zu simulieren. Die teilchenbasierte Herangehensweise an die "multi-particle collision dynamics" ermöglicht Simulationen von sich selbst antreibenden Mikroschwimmern, die in komplexen Strukturen eingeschlossen sind, wo sterische und hydrodynamische Wechselwirkungen die Schwimmdynamiken stark beeinflussen. Einzelheiten der Anordnung und Schlagform der Zilien sind entscheidend, um die Antriebskraft und Oberflächenanziehung zu verstehen. Der Schlag der Zilien wird durch ein halbflexibles Polymer mit periodisch wechselnden intrinsischen Krümmungen modelliert. Im Sinne einer minimalistischen Modellierung wird das Zilium nur in einem Freiheitsgrad gekrümmt, damit eine definierte Schlagebene geschaffen werden kann.

Weitere Untersuchungen verschiedener Schlagmuster mit anwachsender Wellenlänge ergeben eine komplexe Oberflächenanziehungsdynamik der Spermazelle. Die Erkenntnisse aus dem sterischen Modell helfen dabei, diese Oberflächenanziehung in Bezug auf die Einhüllende des Schlagmusters zu verstehen. Es lässt sich beobachten, dass das Schlagmuster ab einer kritischen Wellenlänge dazu führt, dass das Filament einknickt und sich dadurch ein komplexes dreidimensionales Schlagmuster ergibt, welches die Oberflächenanziehung stark erhöht. Schließlich wird ein Kanaldesign mit konstanter Krümmung vorgeschlagen, um Spermien mit einem dreidimensionalen Schlagmuster von denen mit einem ebenen zu unterscheiden. Das zweite Kapitel analysiert dreidimensionale holographische Experimentaldaten von frei schwimmenden menschlichen Spermazellen. Im Mittel ist das Schlagmuster relativ eben, aber es zeigt zweimal pro Schlag Komponenten, die nicht eben sind. Eine mögliche Erklärung für die nicht ebenen Schläge wird gewonnen, indem man die Simulationsergebnisse mit hoch-aufgelösten Experimentaldaten des Zilium-Schlagmusters vergleicht. Wenn man Spermazellen mit festgelegten ebenen Biegungen und einer um zwei Größenordnungen kleineren Verdrillungs-Steifigkeit als die Biegesteifigkeit simuliert, erfahren diese eine Verdrillungs-Instabiltät und zeigen ein dreidimensionales Schlagmuster. Die Simulationen ermöglichen es, den Phasenraum der Verdrillungs-Instabilität abzubilden, die keine Abhängigkeit von der Biegesteifigkeit aufweist, sondern einen scharfen Übergang von ebenen zu dreidimensionalen Schlägen unterhalb einer kritischen Verdrillungs-Steifigkeit. Eine örtlich begrenzte Verdrillungswelle läuft durch das Zilium, die das Zilium in einem sehr engen Segment verdrillt, das nahe dem Punkt von minimaler Biegung auf gleicher Ebene liegt. Dies bewirkt im Wesentlichen die zwei Schlagebenen, indem es das Zilium in zwei Segmente unterteilt, nämlich vor und nach der Verdrillungsregion.

Im zweiten Teil der Arbeit werden die Antriebskraft und die Synchronisation von vielfach zilienbesetzten kugelförmigen Schwimmern mit unterschiedlichen Ziliendichten und -anordnungen untersucht. Anstatt die intrinsische Krümmung vorher festzulegen, treibt ein Mechanismus, der einer Ratsche ähnelt, das Schlagmuster der Zilie an. Daher kann die Schlagperiode durch die Strömung, die durch die Bewegung der anderen Zilien erzeugt wird, beeinflusst werden. Die Antriebsgeschwindigkeit von zilienbesetzten kugelförmigen Schwimmern steigert sich sublinear mit zunehmender Ziliendichte. Es lassen sich große Unterschiede in der Antriebsgeschwindigkeit gleicher Anzahlen von Zilien mit unterschiedlicher Anordnung auf der Kugel beobachten. Für symmetrische zilienbesetzte Schwimmer zeigt sich, dass die Entstehung einer stabilen Synchronisation vom Anfangszustand abhängt. In einigen symmetrischen Schwimmern mit 9 Zilien entwickeln sich lange Phasen der Synchronisation. Schwimmer, deren Phasenunterschied aufgrund von Phasensprüngen zunimmt, haben eine langsamere Antriebsgeschwindigkeit als Schwimmer, die eine konstante Phasenverzögerung entwickeln. Die Entstehung von metachronaler Koordination in verschiedenen Anordnungen in der Nähe einer Oberfläche werden untersucht, indem ein einfaches Oszillatormodell für die Ziliensynchronisation angewendet wird. Die Oszillatoren werden als hydrodynamisch interagierende Kugeln, die sich in einer kreisförmigen Bahn vorwärts bewegen, modelliert. Die Entdimensionalisierung des Modells ergibt die radiale Begrenzung als einzigen Kontrollparameter in dem Modell. Die Synchronisation wird ebenso durch Randeffekte wie durch die Begrenzungsstärke beeinflusst. Bis hin zu einer kritischen Begrenzungsstärke zeigen sich stabile großformatige Synchronisationsmuster sowohl in offenen Reihen von Oszillatoren als auch in kreisförmigen Anordnungen. Oberhalb einer kritischen Begrenzungsstärke erscheint in keiner der untersuchten Strukturen eine langfristige Koordination. Als letzter Schritt wird das Ziliummodell genutzt, um ein Büschel von Zilien zu modellieren, zu dem Zweck, die Platzierung von Zilien in den Gehirnventrikeln von Mäusen zu beschreiben. Es wird beobachtet, dass die Partikelströmung in Richtung der Oberfläche in Häufungspunkten lokalisiert ist, wo die Strömung, verglichen mit bloß diffusivem Transport, deutlich gesteigert wird. Das zeigt die wichtige Rolle des Zilienschlagens im molekularen Transport gegenüber den ursprünglichen Zilien auf der Oberfläche der Ventrikel.

Erklärung zur Dissertation

Ich versichere, dass ich die von mir vorgelegte Dissertation selbständig angefertigt, die benutzten Quellen und Hilfsmittel vollständig angegeben und die Stellen der Arbeit – einschließlich Tabellen, Karten und Abbildungen –, die anderen Werken im Wortlaut oder dem Sinn nach entnommen sind, in jedem Einzelfall als Entlehnung kenntlich gemacht habe; dass diese Dissertation noch keiner anderen Fakultät oder Universität zur Prüfung vorgelegen hat; dass sie – abgesehen von unten angegebenen Teilpublikationen – noch nicht veröffentlicht worden ist, sowie, dass ich eine solche Veröffentlichung vor Abschluss des Promotionsverfahrens nicht vornehmen werde.

Die Bestimmungen der Promotionsordnung sind mir bekannt. Die von mir vorgelegte Dissertation ist von Prof. Dr. Gerhard Gompper betreut worden.

Sebastian Rode
Jülich 2017

Sebastian Rode

[redacted]

[redacted]

[redacted]

[redacted]

[redacted]
[redacted] ✉ s.rode@fz-juelich.de